

## ABSTRACT

Title of Dissertation: A PREDICTIVE MODEL FOR  
MULTIPACTOR DISCHARGE BASED ON  
CHAOS THEORY

Moiz Siddiqi  
Doctor of Philosophy, 2019

Dissertation directed by: Doctor Rami Kishek  
Department of Electrical and Computer  
Engineering

As the demand for high-power radio-frequency (RF) applications continues to rise, modern-day technology is becoming increasingly prone to multipactor breakdown. Multipactor is a pernicious electron discharge driven by secondary electron emission (SEE) that plagues microwave components, particle accelerators, space-borne systems, and other related electronics. It occurs when electrons in a vacuum are accelerated by electromagnetic fields and impact device walls, resulting in the emission of secondary electrons from the surfaces. Under certain conditions, this process repeats and the number of electrons grows exponentially, potentially disrupting device operation or even causing component failure. Despite several decades of study, multipactor continues to be a longstanding engineering problem with no comprehensive theoretical solution.

This dissertation presents a novel theoretical approach for the understanding, prediction, and assessment of multipactor discharge. Drawing upon techniques from chaos theory, this new theory models multipactor as a complex dynamical system, where iterative maps track the RF phases at the surface impacts with no *a priori* assumptions on the electron trajectories. By systematically applying these maps and scanning system parameters, bifurcation diagrams are constructed that recover a plethora of multipacting modes. This information is combined with the SEE properties of the surface material to compute the multipactor exponential growth rate throughout parameter space.

The theory is first illustrated for a parallel-plate geometry driven by RF and DC fields. Here, the system attractor form is found to manifest in the exponential growth rate, where high-periodicity and chaotic modes suppress multipactor growth. Conventional multipactor regions are recovered but new parameter spaces susceptible to the discharge are also identified. These theoretical predictions are verified with particle-in-cell simulations and industrial design standards. Next, the theory is expanded to a coaxial system and validated against published simulation and experimental results. Finally, the theory is generalized to multicarrier operation, where several RF carriers (each with a separate amplitude and frequency) coexist, as employed in modern space communication systems. This is demonstrated for the lowest-order system in a parallel-plate geometry, namely two-carrier operation. These results are verified with particle-in-cell simulations. This model serves as the first comprehensive theoretical solution for multipactor in multicarrier systems.

A PREDICTIVE MODEL FOR MULTIFACTOR DISCHARGE BASED ON  
CHAOS THEORY

by

Moiz Siddiqi

Dissertation submitted to the Faculty of the Graduate School of the  
University of Maryland, College Park, in partial fulfillment  
of the requirements for the degree of  
Doctor of Philosophy  
2019

Advisory Committee:  
Professor Thomas Antonsen, Chair  
Doctor Rami Kishek, Co-Chair/Advisor  
Professor Edward Ott  
Professor Phillip Sprangle  
Professor Steven Anlage

© Copyright by  
Moiz Siddiqi  
2019

## Acknowledgements

I first and foremost thank my research advisor, Rami Kishek, for introducing me to multipactor and providing me an opportunity to pursue this research. I have greatly benefited from his mentorship and scientific knowledge. His encouragement, advise, support, and guidance facilitated my transition into an independent researcher and thinker. I am tremendously proud of this thesis and thank Rami for all his efforts in educating me.

Next, I acknowledge the University of Maryland Electron Ring (UMER) staff members for providing a supportive environment, especially in my first year: Brian Beaudoin, Santiago Bernal, Irving Haber, and David Sutter. I also thank Eric Montgomery for guiding me in the direction that eventually led me to this research and for helpful discussions during my time here. Additionally, Professor Antonsen and Professor Ott allowed me to present to their research group and provided constructive feedback throughout this work. I further thank Professors Antonsen and Ott, along with Professor Sprangle and Professor Anlage, for serving on my thesis defense committee.

Moreover, I thank the graduate students whom I shared an office with during these years: Kiersten Ruisard, Heidi Komkov, Levon Dovlatyan, and David Matthew. You are all good friends and I will cherish the good times. I wish you all the best in your future endeavors. Finally, I thank my friends and family, especially my parents and sisters, for supporting me in all aspects of my life. I am proud to share this success with all of you. This research was funded by the National Science Foundation (NSF) and the University of Maryland Division of Research.

# Table of Contents

|  |           |
|--|-----------|
| Acknowledgements .....   | ii        |
| Table of Contents .....  | ii        |
| List of Tables .....   | v         |
| List of Figures .....  | vi        |
| <b>1 Introduction.....</b>   | <b>1</b>  |
| 1.1 Chapter Overview .....   | 1         |
| 1.2 Motivation.....  | 1         |
| 1.3 Conventional Understanding .....   | 3         |
| 1.3.1 Resonance Theory.....  | 3         |
| 1.3.2 Secondary Electron Emission Yield .....  | 6         |
| 1.4. Modern-Day Prediction Methods .....   | 10        |
| 1.4.1 Universal Susceptibility Diagrams .....  | 10        |
| 1.4.2 Stochastic Models .....  | 12        |
| 1.4.3 Experimental Works .....   | 13        |
| 1.5 Shortcomings of Conventional Theories and Approaches .....   | 14        |
| 1.6 Brief Historical Overview .....  | 17        |
| 1.7 Introduction to Map-Based Multipactor Theory.....  | 20        |
| 1.8 Assumptions.....   | 22        |
| 1.9 Organization of Thesis.....  | 23        |
| <br>   |           |
| <b>2 Map-Based Multipactor Theory for a Parallel-Plate Geometry.....</b>   | <b>24</b> |
| 2.1 Chapter Overview .....   | 24        |
| 2.2 Map-Based Theory Under an RF Electric-Field.....   | 24        |
| 2.2.1 Basic Equations and Multipactor Maps .....   | 24        |
| 2.2.2 Bifurcation Diagrams and Comparison to Resonance Theory .....  | 30        |
| 2.2.3 Multipactor Exponential Growth Rate and Incorporation of Spreads in<br>Secondary Emission Energies and Angles .....                      | 37        |
| 2.2.4. Comparison to Simulation .....  | 41        |
| 2.3 Map-Based Theory Under RF and DC Electric-Fields.....  | 45        |
| 2.3.1 Multipactor Maps and Bifurcation Diagrams .....  | 45        |
| 2.3.2 Comparison to Simulation .....   | 48        |
| 2.4 Map-Based Theory with a Transverse DC Magnetic-Field.....  | 52        |
| 2.4.1 Basic Equations, Bifurcation Diagrams, and Comparison to Resonance<br>Theory.....  | 52        |
| 2.4.2 Comparison to Simulation .....   | 59        |
| 2.5 Construction of Universal Multipactor Susceptibility Diagrams from Map<br>Based Theory and Comparison to Industrial Design Standards ..... | 61        |

|       |  |    |
|-------|--|----|
| 3     | Map-Based Multipactor Theory for Coaxial Systems .....                                       | 69 |
| 3.1   | Chapter Overview .....   | 69 |
| 3.2   | Map-Based Multipactor Theory for a Coaxial System .....                                      | 69 |
| 3.2.1 | Basic Equations and Multipactor Maps .....   | 69 |
| 3.2.2 | Comparison to Published Simulation and Experimental Results .....                            | 75 |
| 4     | Map-Based Multipactor Theory for MultiCarrier Operation.....                                 | 80 |
| 4.1   | Chapter Overview .....   | 80 |
| 4.2   | Map-Based Multipactor Theory for Two-Carrier Operation in a Parallel-Plate<br>Geometry ..... | 80 |
| 4.2.1 | Basic Equations and Multipactor Maps .....   | 80 |
| 4.2.2 | Comparison to Simulation and Two-Carrier Susceptibility Diagrams                             | 84 |
| 5     | Summary and Future Research Directions .....   | 89 |
| 5.1   | Chapter Overview .....   | 89 |
| 5.2   | Summary .....  | 89 |
| 5.3   | Future Research Directions.....  | 92 |
| A     | Brief Review of Chaos Theory .....   | 93 |
|       | Bibliography .....   | 97 |

# List of Tables

|     |   |   |
|-----|---|---|
| 1.1 | Secondary electron emission (SEE) parameters for different materials, as specified by the European Space Agency (ESA) ..... | 8 |
|-----|---|---|

# List of Figures

|     |  |    |
|-----|--|----|
| 1.1 | Multipactor Resonance Dynamics. Figure taken from Ref. [20] .....  | 4  |
| 1.2 | Secondary electron emission (SEE) yield $\delta$ as a function of electron impact energy for normal incidence ( $\theta_1 = 0$ ). $W_1$ , $W_2$ , $\delta_{\max 0}$ , and $W_{\max 0}$ are all material dependent parameters (see Table 1.1) .....   | 7  |
| 1.3 | Multipactor susceptibility diagram adopted from the European Space Agency (ESA) for aluminum material [18]. Each resonance order (N) defines a separate pair of boundaries in the fD-voltage space. Discrepancies with experiments (circles outside the predicted zones) are accounted for by an arbitrary margin (solid black line) ..... | 11 |
| 2.1 | Parallel-plate geometry with gap separation D and normal RF and DC electric-fields. Direction of coordinate system for an electron emitted from a.) surface-0 and b.) surface-1 .....  | 25 |
| 2.2 | Multipactor map (Eq. 2.7) relating an emission phase $\theta_0$ to the phase at the next impact for fixed system parameters $\bar{E}_0 = 0.50$ , $\bar{v}_{0x} = 0.10$ , and $\eta = 0$ . The map is color-coded according to impact phases resulting from two-surface transits (red) and single-surface transits (blue) .....             | 29 |
| 2.3 | Bifurcation diagram constructed by scanning $\bar{E}_0$ in $[0.10, 1.20]$ for a fixed $\bar{v}_{0x} = 0.03$ and $\eta = 0$ . Attractor phases resulting from two-surface transits and single-surface transits are shown in red and blue, respectively .....  | 31 |

|      |   |    |
|------|---|----|
| 2.4  | Zoomed-in view of Fig. 2.3 for $\bar{E}_0$ between 0.10-0.24 .....  | 32 |
| 2.5  | First-order ( $N = 1$ ) two-surface resonance stability boundaries recovered by the bifurcation diagram in Fig. 2.3 for $\bar{v}_{0x} = 0.03$ .....   | 34 |
| 2.6  | Bifurcation diagram constructed by scanning $\bar{v}_{0x}$ in $[0.02, 0.80]$ for a fixed $\bar{E}_0 = 0.70$ and $\eta = 0$ . Attractor phases resulting from two-surface transits and single-surface transits are shown in red and blue, respectively .....   | 36 |
| 2.7  | Average SEE yield over an RF period (black curve) for the $\bar{E}_0$ scan in Fig. 2.3 (scale shown on right). The RF frequency and gap separation are $f = 500$ MHz and $D = 7$ mm, respectively. For each scan, a monoenergetic emission $\bar{v}_{0x} = 0.03$ is assumed and the DC electric-field is turned off ( $\eta = 0$ ) .....  | 38 |
| 2.8  | Effective SEE yield over an RF period from theory with an emission energy scan (red) and Warp simulations (black) as a function of $\bar{E}_0$ . The RF frequency and gap separation are $f = 500$ MHz and $D = 7$ mm, respectively, and the DC electric-field is turned off ( $\eta = 0$ ). The corresponding RF electric-field amplitude scan range is from 39.28 kV/m to 471.37 kV/m ..... | 44 |
| 2.9  | Bifurcation diagrams for a.) surface-0 and b.) surface-1 constructed by scanning $\eta$ in $[-1.0, 1.0]$ for a fixed $\bar{v}_{0x} = 0.03$ and $\bar{E}_0 = 0.30$ . Attractor phases resulting from two-surface transits and single-surface transits are shown in red and blue, respectively.....   | 47 |
| 2.10 | Effective SEE yield over an RF period from theory with an emission energy scan (red) and Warp simulation (black) as a function of $\eta$ . The RF frequency, gap separation, and RF field amplitude are $f = 500$ MHz, $D = 7$ mm, and $E_0 = 91.75$ kV/m corresponding to $\bar{E}_0 \approx 0.23358$ . The corresponding DC electric-field scan   |    |

|   |    |
|---|----|
| range is from 0 kV/m to $E_0$ .....   | 50 |
| 2.11 Bifurcation diagram for surface-0 constructed by scanning $\eta$ for a monoenergetic $\bar{v}_{0x} = 0.05$ and a fixed $\bar{E}_0 = 0.23358$ . Attractor phases resulting from two-surface transits and single-surface transits are shown in red and blue, respectively .....  | 51 |
| 2.12 Parallel-plate geometry with normal RF electric-field and a transverse DC magnetic-field. Here, $\phi$ is the emission angle with respect to the surface tangential .....  | 53 |
| 2.13 Bifurcation diagram constructed by scanning $\bar{E}_0$ in $[0.10, 1.20]$ for a fixed $\bar{v}_{0x} = \bar{v}_{0y} = 0.03$ and $\Omega = 0.50$ . Attractor phases resulting from two-surface transits and single-surface transits are shown in red and blue, respectively .....  | 55 |
| 2.14 First-order ( $N = 1$ ) two-surface resonance stability boundaries recovered by the bifurcation diagram in Fig. 2.13 for $\Omega = 0.50$ and $\bar{v}_{0x} = \bar{v}_{0y} = 0.03$ .....  | 57 |
| 2.15 Bifurcation diagram constructed by scanning $\Omega$ in $[0.0, 1.50]$ for a fixed $\bar{E}_0 = 0.23358$ and $\bar{v}_{0x} = \bar{v}_{0y} = 0.05$ . Attractor phases resulting from two-surface transits and single-surface transits are shown in red and blue, respectively .....  | 58 |
| 2.16 Effective SEE yield over an RF period from theory with an emission energy scan (red) and Warp simulation (black) as a function of $\Omega$ . The RF frequency, gap separation, and RF field amplitude are $f = 500$ MHz, $D = 7$ mm, and $E_0 = 91.75$ kV/m, respectively, corresponding to $\bar{E}_0 \approx 0.23358$ . The corresponding DC magnetic-field scan range is from 0 mT to 27 mT ..... | 60 |
| 2.17 Multipactor susceptibility diagram (log-log plot) for copper material in the absence of DC fields (i.e., $\eta = \Omega = 0$ ) constructed from the map-based theory.  |    |

|      |   |    |
|------|---|----|
|      | Here, the RF frequency is $f = 1$ GHz. Contours corresponding to different magnitudes of $\delta_{\text{eff}}$ are shown. The black contours are the multipacting boundaries .....  | 62 |
| 2.18 | European Space Agency (ESA) design standard [18] (dashed lines) for copper material shown on top of the susceptibility diagram from theory (Fig. 2.17). Here, each separate design margin is labeled either as ‘1’, ‘2’, or ‘3’ .....   | 64 |
| 2.19 | Results from particle-in-cell simulations (crosses) at various points on the susceptibility diagram from theory. Here, red crosses are placed on parameter regions that support multipactor growth (i.e., $\delta > 1$ ) while black crosses are placed on parameter regions that support multipactor decay (i.e., $\delta < 1$ ).....                                  | 65 |
| 2.20 | Multipactor susceptibility diagram (log-log plot) for copper material with $B_{\text{DC}} = 10$ mT (corresponding to $\Omega \approx 0.28$ ) constructed from the map-based theory. Here, the RF frequency is taken to be $f = 1$ GHz. Contours corresponding to different magnitudes of $\delta_{\text{eff}}$ are shown (according to the same code in Fig. 2.17 ..... | 67 |
| 3.1  | Cross-sectional view of a coaxial geometry with inner-radius $a$ and outer-radius $b$ . The cylindrical coordinate system $(r, \phi, z)$ is shown, where the $z$ -axis extends along the length of the conductors (i.e., into or out of the page). The radial RF electric-field and the axial DC magnetic-field are also shown .....                                    | 70 |
| 3.2  | Effective SEE yield as a function of $\bar{E}_0$ for fixed parameters $\Omega = 0.856$ (corresponding to $B_{\text{DC}} = 35$ mT and $f = 1.145$ GHz) and $R = 0.434$ (corresponding to $a = 1.515$ mm and $b = 3.490$ mm). The normalized threshold point $\bar{E}_{0\text{TH}}$ is  |    |

defined as the value where  $\delta_{\text{eff}} \approx 1.0$  (indicating the onset of multipactor) ..... 77

3.3 Multipactor threshold power predicted by the map-based theory (red circles) against simulation (green triangles) and experimental (blue squares) results from from Ref. [70]. The value of the normalized parameter  $\Omega$  is shown for different DC magnetic-field strengths ..... 78

4.1 Parallel-plate geometry with gap separation  $D$  and fundamental-carrier ( $E_{\text{RF1}}$ ) and second-carrier ( $E_{\text{RF2}}$ ) RF electric-fields. Direction of coordinate system for an electron emitted from a.) surface-0 and b.) surface-1..... 81

4.2 Effective SEE yield over a fundamental RF period from theory with an emission energy scan (red) and Warp simulations (black) as a function of  $\beta$ . The fundamental RF field amplitude and frequency are  $E_{01} = 91.75$  kV/m and  $f_1 = 500$  MHz, respectively, while the gap separation is  $D = 7$  mm (corresponding to  $\bar{E}_{01} \approx 0.23358$ ). The RF frequency of the second-carrier is  $f_2 = 250$  MHz (corresponding to  $n = 0.50$ ). The corresponding second-carrier field amplitude scan range is from 0 kV/m to 183.5 kV/m ..... 86

4.3 Two-carrier susceptibility diagram for  $E_{01} = 91.75$  kV/m,  $f_1 = 500$  MHz, and  $D = 7$  mm (corresponding to  $\bar{E}_{01} \approx 0.23358$ ). The diagram is color-coded according to the magnitude of the effective SEE yield (color-code shown on right) ..... 88



# Chapter 1: Introduction

## 1.1 Chapter Overview

This chapter first introduces multipactor discharge and provides a motivation for this dissertation research (Sect 1.2). The conventional understanding of multipactor and modern-day prediction methods are then presented (Sect.'s 1.3 and 1.4). The shortcomings of such methods are discussed, motivating the need for a new theoretical approach (Sect. 1.5). A brief historical review of multipactor is provided (Sect. 1.6) and a new map-based theoretical approach is then introduced (Sect. 1.7). The core assumptions made throughout the thesis are then listed and justified (Sect. 1.8). This chapter concludes with an overview of the organization of the thesis (Sect. 1.9).

## 1.2 Motivation

Multipactor is an electron discharge driven by secondary electron emission (SEE) [1]. It occurs when electrons in near-vacuum conditions are accelerated by electromagnetic fields and impact device walls, resulting in the emission of secondary electrons from the surfaces. Under certain conditions, this process repeats and the number of electrons grows exponentially. Multipactor occurs over a wide range of voltages and frequencies and in numerous geometries.

Today, multipactor is ubiquitous, occurring in microwave/radio-frequency (RF) components [2-4], particle-accelerators [5-9], space-borne systems [10-12], and other related electronics. It is often undesirable as the electron avalanche can lead to signal

noise, reflected power, overheating, power dissipation, surface outgassing, component damage, or even total device failure. Multipactor poses an especially challenging problem to the space industry, where any incidence of the discharge in space can compromise an entire mission. As a result, modern-day research is heavily geared towards eliminating the discharge and suppression techniques continue to be in high-demand. However, it is worthwhile to note that some applications are interested in using multipactor for beneficial purposes, such as for plasma displays, electron guns, or for the protection of highly sensitive receivers [13-14].

Despite decades of study, multipactor continues to be a longstanding engineering problem with no comprehensive theoretical solution. The underlying reason for this is that this phenomenon is still not very well understood. The large parameter space presented by the electromagnetic fields, geometry, and surface material makes it a difficult problem to analyze.

Conventional theories make simplified assumptions on the electron trajectories to predict breakdown boundaries as a function of device parameters [1, 15-16] (see Sect. 1.4.1). Although these susceptibility diagrams are obsolete and unreliable, they continue to serve as modern-day design standards [17-20]. Other approaches rely on stochastic methods (i.e., Monte Carlo models, particle-tracking codes, or statistical theory) to predict multipactor breakdown (see Sect. 1.4.2) [21-33]. While these approaches successfully model some devices, the results are often difficult to generalize and the underlying multipactor dynamics are not always clear. Additionally, these approaches can have high computational cost, especially in cases where the number of multipactor electrons is large.

As no theory to date explains universal multipactor behavior, the motivation of this research is to establish a thorough understanding of multipactor. In light of this, this thesis presents a novel theoretical study for the understanding, prediction, and assessment of multipactor based on principles from nonlinear dynamics and chaos theory. This theory is derived from first principles and demonstrated for a variety of systems, including parallel-plate, coaxial, and multicarrier. Throughout this thesis, the theoretical predictions are verified against existing theoretical models, particle-in-cell simulations, industrial design standards, and experimental data. As shown in the core chapters of this thesis (Ch.'s 2-4), this theory revolutionizes our understanding of multipactor dynamics and provides a comprehensive and predictive model.

## 1.3 Conventional Understanding

### 1.3.1 Resonance Theory

Early researchers recognized that a possible mechanism for multipactor growth is synchronism between the electron transit-times (from emission to impact) and the RF electric-field [1, 15, 16, 34]. This behavior became to be known as resonance. Figure 1.1 illustrates the concept of multipactor resonance assuming a parallel-plate geometry (i.e., two conducting plates separated by a gap) with a RF electric-field perpendicular to the surfaces.

Consider an electron emitted from the bottom plate during the decelerating portion of the RF cycle. As the electron charge is negative, this decelerating electric-field provides a positive force, accelerating the electron towards the top plate. If the

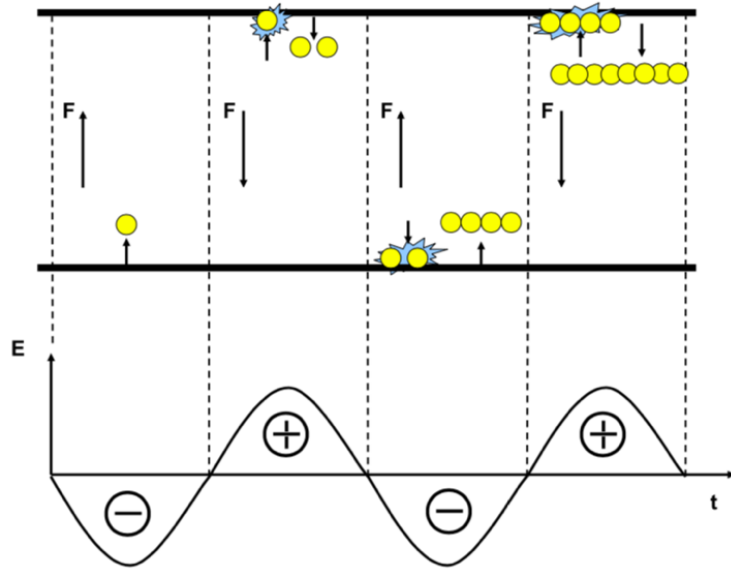


Figure 1.1: Multipactor Resonance Dynamics. Figure taken from Ref. [20].

electron impacts the top plate by the time the RF electric-field reverses polarity (i.e., to an accelerating field), then electrons released from this plate (as a result from the impact) are accelerated towards the bottom plate. The impacting electron(s) (which are usually absorbed by the surface upon impact) are referred to as primary electron(s) while the emitted electrons released from the plate are referred to as secondary electron(s). For the purpose of this discussion, secondaries are assumed to be emitted on each impact (with a singular energy). If the secondaries impact the bottom plate by the time the RF field again reverses polarity (i.e., back to a decelerating field), the next generation of secondaries can then be accelerated towards the top plate as before. As this resonance pattern continues to repeat, the electron population grows exponentially, possibly leading to multipactor breakdown.

The requirement for this synchronous (resonance) motion is that the one-way transit-time for an electron to impact the opposite surface is equal to an odd number of RF half-periods, i.e.,  $t_1 = N\pi/\omega$ . Here,  $N$  is an odd integer corresponding to the number of RF half-periods between each surface impact while  $\omega$  is the RF frequency of the electric-field. In the literature,  $N$  is also referred to as the resonance order [1]. Thus, a first-order ( $N = 1$ ) resonance describes the case where the electron transit-time between impacts is a RF half-period. This resonance condition guarantees that the next generation of secondaries experiences the same exact field conditions as the preceding primaries, allowing for the multipacting process to continually repeat. The RF phase at which the resonant impacts occur periodically is referred to as the fixed-phase [1].

The requirement that electron impacts in resonant multipactor always occur at the fixed-phase is rarely, if never, met in practice. Instead, as a result of phase stability (or phase focusing), there exists a range of impact phases (i.e., a basin of attraction) that converges to resonance behavior. Impact phases that deviate from the fixed-phase but remain within the basin of attraction eventually converge back to resonance behavior at the fixed-phase. On the other hand, impact phases that occur outside the basin of attraction diverge away from the fixed-phase (and multipactor resonance). For a given resonance order  $N$ , RF frequency, gap separation, and secondary emission energy, the lower (upper) boundary of the stable phases corresponds to the upper (lower) RF voltage required to sustain the resonance discharge. The reader is referred to Ref. [1] for a mathematical derivation of the range of stable impact phases.

Note that the resonance cycle cannot continue forever, as saturation mechanisms eventually cease the discharge. One such mechanism is space-charge,

where the coulomb (electrostatic) repulsion due to the increasing electron density disrupts resonance behavior (and broadens the electron bunch) [35-36]. Other saturation mechanisms include beam loading and frequency detuning, which commonly occur in RF cavities [37-40]. In this thesis, saturation mechanisms are neglected, as this research is mainly concerned with the initiation of multipactor.

Figure 1.1 is a simplified picture and does not correctly model all the main physics of the multipacting process. In fact, as shown throughout this thesis, resonance itself is a major assumption as multipactor is capable of manifesting in a variety of forms. The drawbacks of this simplified view are discussed further in Sect. 1.5.

### 1.3.2 Secondary Electron Emission Yield

The second main requirement for multipactor arises from the secondary emission properties of the surface material. Multipactor is typically characterized by the secondary electron emission (SEE) yield  $\delta$ , defined as the average number of emitted secondaries per incident primary [41-42].  $\delta$  is a function of the primary impact energy  $W_I$ , the impact angle  $\theta_I$  (defined with respect to the surface normal), and the surface material properties. A typical curve illustrating the SEE yield dependence on the electron impact energy (for normal incidence, i.e.,  $\theta_I = 0$ ) is shown in Fig. 1.2.

As shown by Fig. 1.2, the SEE yield is above unity (corresponding to multipactor growth) only for a range of impact energies that lie between the first and second crossover energies (denoted as  $W_1$  and  $W_2$ , respectively). This can be understood as follows. For impact energies below  $W_1$ , the impacting electron does not impart sufficient energy to release secondaries from the surface. For impact energies

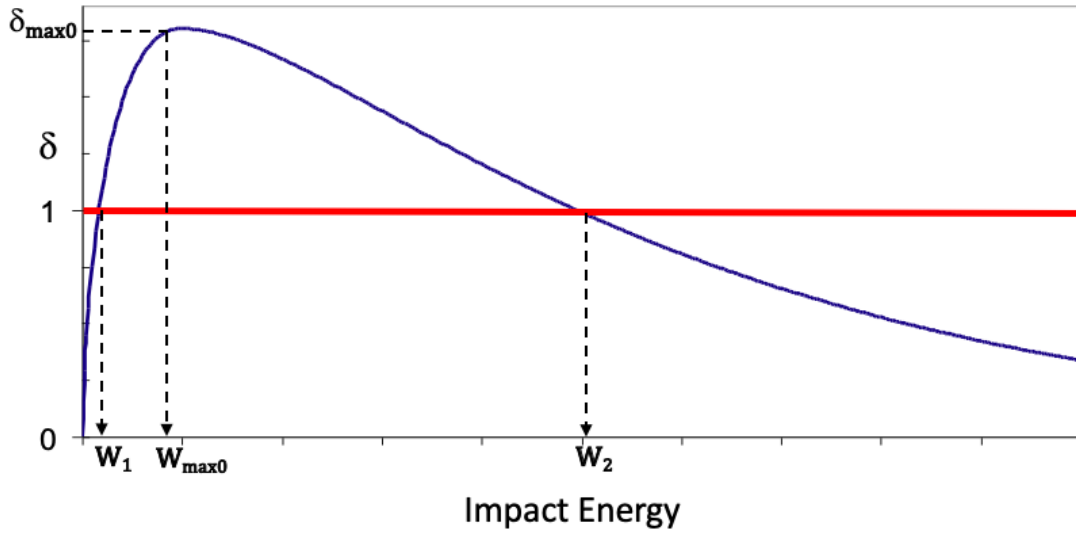


Figure 1.2: Secondary electron emission (SEE) yield  $\delta$  as a function of electron impact energy for normal incidence ( $\theta_I = 0$ ).  $W_1$ ,  $W_2$ ,  $\delta_{\max 0}$ , and  $W_{\max 0}$  are all material dependent parameters (see Table 1.1).

greater than  $W_2$ , the primary electron penetrates the surface too deeply and secondaries therefore cannot escape the surface. As a result, the impact energy has to lie in a certain range for multipactor to occur.  $\delta_{\max 0}$  is defined as the peak SEE yield resulting from an impact occurring with an energy  $W_{\max 0}$ . The parameters  $W_1$ ,  $W_2$ ,  $\delta_{\max 0}$ , and  $W_{\max 0}$  are all material dependent. Table 1.1 shows these parameters for standard engineering materials, as specified by the European Space Agency (ESA) [18]. As the crossover energies are far below the electron rest energy ( $\sim 511$  keV), multipactor is a nonrelativistic effect.

Table 1.1: Secondary electron emission (SEE) parameters for different materials, as specified by the European Space Agency (ESA) [18].

| Material | $W_1$ [eV] | $W_2$ [eV] | $\delta_{\max 0}$ | $W_{\max 0}$ [eV] |
|----------|------------|------------|-------------------|-------------------|
| Copper   | 25         | 5000       | 2.25              | 175               |
| Aluminum | 30         | 5000       | 2.98              | 805               |
| Silver   | 30         | 5000       | 2.22              | 165               |
| Gold     | 150        | 4000       | 1.79              | 1000              |

A common model for SEE is Vaughan's empirical formula, which specifies the SEE yield dependence on the material properties, the impact energy, and the impact angle [41]. This formula is given by:

$$\delta(W_I, \theta_I) = \delta_{\max}(v e^{1-v})^k \quad (1.1a)$$

$$\delta_{\max} = \delta_{\max 0} \left( 1 + k_s \frac{\theta_I^2}{2\pi} \right) \quad (1.1b)$$

$$v = (W_I - W_c) / (W_{\max} - W_c) \quad (1.1c)$$

$$W_{\max} = W_{\max 0} \left( 1 + k_s \frac{\theta_I^2}{2\pi} \right). \quad (1.1d)$$

In Eq. 1.1a,  $\delta(W_I, \theta_I)$  is the SEE yield resulting from an impact with energy  $W_I$  and angle  $\theta_I$ . Here,  $k$  is defined to be 0.62 for  $v < 1$  and 0.25 for  $v > 1$  while  $k_s$  is a surface smoothness parameter, ranging from 0 (for a rough surface) to 2 (for a polished surface). In this thesis,  $k_s = 1$ , corresponding to a typical dull surface. The parameter  $W_c$  is conventionally taken to be 12.5 eV.

While Vaughan's formula is a well-established model for true secondaries, it does not incorporate the effects due to low energetic backscattered and reflected primaries, which have been shown to play a considerable role in multipactor dynamics [43-45]. To incorporate the effects of low energetic backscattered primaries, a modified version of Vaughan's formula is often used [46]. The modification is namely that the SEE yield for impact energies below  $W_c$  is set to a fixed value  $\delta_0$ , corresponding to the probability of elastic and inelastic backscatter (typically between 0.5 and 1.0). For instance,  $\delta_0 = 0.70$  for copper material. In this thesis, this modified Vaughan's formula is employed.

In practice, the RF electric-field also penetrates the surface material (at a depth roughly equal to the skin depth of the metal). For typical parameters ( $W_I \approx 5$  keV,  $E_{RF} \approx 1$  MV/m), the electron penetration depth is  $d \approx 0.125$   $\mu\text{m}$  while the penetration depth of the RF electric-field (for copper and an RF frequency of  $f = 1$  GHz) is roughly 2  $\mu\text{m}$  and exceeds the penetration depth of the primary electron by an order of magnitude. Thus, it would seem that a complete SEE model should include the effects of the penetrating RF electric-field on the embedded primary. However, the magnitude of the effective electric-field ( $E_{eff} \approx W_I/(ed)$ ), which stops the primary electron a depth  $d$  within the material, is far greater than the magnitude of the RF electric-field in the gap. Thus, the effects of the RF electric-field are negligible and the SEE model given by Eq. 1.1 is sufficient.

## 1.4 Modern-Day Prediction Methods

### 1.4.1 Universal Susceptibility Diagrams

As shown in Sect. 1.3, multipactor is conventionally understood to occur when electrons are in resonance with the RF electric-field and the electron impact energies lie between the crossover energies (for a given material). These two criteria are often combined together to form susceptibility diagrams (assuming monoenergetic secondary emission), which portray multipactor boundaries as a function of device parameters. These diagrams were first constructed by Hatch and Williams [15-16] in the 1950's. Today, these diagrams continue to serve as design standards for the space industry, as found in multipactor prevention handbooks prepared by the European Space Agency (ESA) (2003, 2013) [18], The Aerospace Corporation (2014) [19], and The American Institute of Aeronautics and Astronautics (AIAA) (2016) [20].

Figure 1.3 shows an example of a susceptibility diagram adopted by the ESA [18]. In this diagram, the vertical axis is the peak RF voltage (in volts) while the horizontal axis is the frequency-gap product (in GHz-mm). Each resonance order (N) defines a separate pair of lines. These boundaries enclose the regions that support the corresponding order of multipactor. Thus, parameter regions inside the boundaries support multipactor growth while parameter regions outside these boundaries (ideally) support multipactor decay. This diagram further indicates that multipactor can significantly limit the achievable RF power.

Such a diagram is a useful tool for device design, as it can identify parameter spaces that result in multipactor-free operation. Note that these diagrams feature experimental discrepancies (circles in Fig. 1.3 that lie outside side the predicted zones),

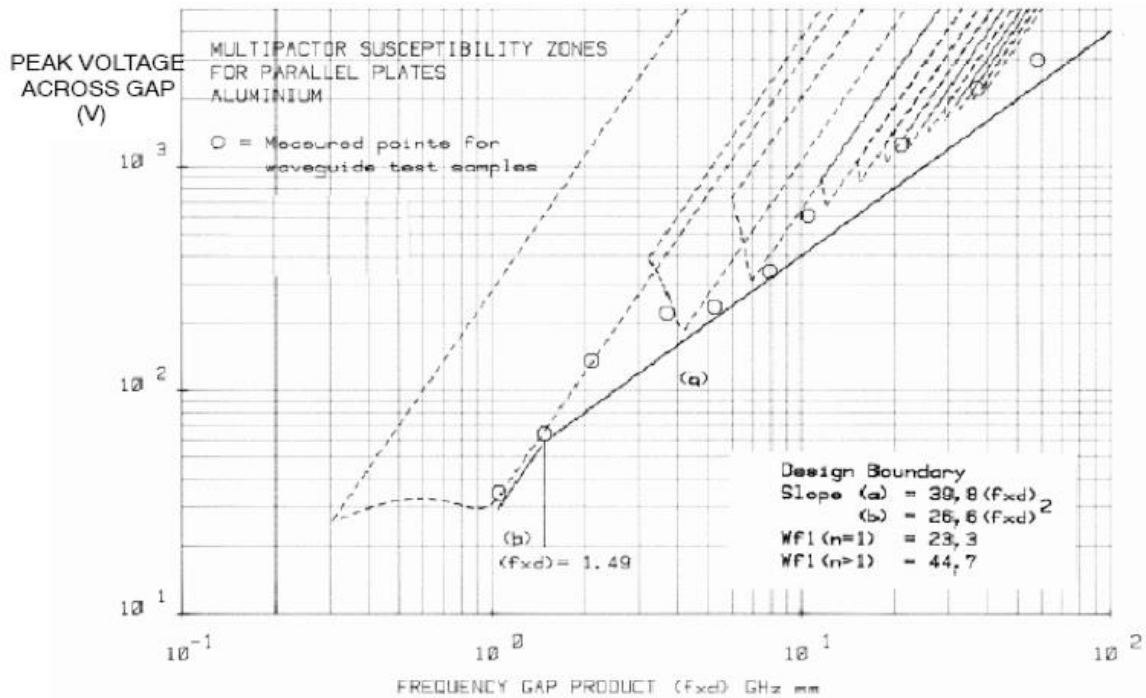


Figure 1.3: Multipactor susceptibility diagram adopted from the European Space Agency (ESA) for aluminum material [18]. Each resonance order (N) defines a separate pair of boundaries in the  $fD$ -voltage space. Discrepancies with experiments (circles outside the predicted zones) are accounted for by an arbitrary margin (solid black line).

which are accounted for by arbitrary margins that have no theoretical basis (solid line in Fig. 1.3). These obsolete and unreliable susceptibility diagrams partly motivate the new theoretical approach presented in this thesis. In fact, in Sect. 2.5, susceptibility diagrams are constructed from this new theory and compared to industrial standards.

## 1.4.2 Stochastic Models

One major class of multipactor prediction tools is stochastic models, which generally have three forms: Monte Carlo simulations, particle-tracking codes, and statistical theories. These approaches are rooted in the well-understood fact that secondary emission energies (and angles) are inherently random and therefore described by probability distributions as opposed to singular values. In light of this, these approaches aim to study multipactor as a random process.

Monte Carlo models have been extensively applied to study the longstanding problem of single-surface multipactor on a dielectric surface [21-26]. In a Monte Carlo simulation, a macroparticle is systematically tracked under the influence of the electromagnetic fields for a long period of time. On each impact with a surface, the macroparticle is emitted from the surface with a random energy and angle according to specified probability distributions. The charge (and mass) of the macroparticle are adjusted according to the SEE yield from each impact. Observing the macroparticle charge for a sufficiently long time indicates either multipactor growth or decay.

In a particle-tracking code, electron trajectories are numerically tracked to investigate the evolution of multipactor. Here, space and time are discretized while the electromagnetic fields are specified on a 3D grid. On each time-step of the simulation, electrons are self-consistently advanced in space according to the Lorentz force-law (note that space-charge fields may also be included in addition to the applied fields). On each surface impact, secondaries are emitted according to the impact energy/angle with a random emission energy and angle. The total number of particles during the simulation indicates either multipactor growth or decay. Today, particle-tracking codes

are widely used by industry to aid in the design of multipactor-free components. Examples include Computer Simulation Technology (CST) codes [47], such as FEST3D [48], and Spark3D [49]. The theoretical approach presented in this thesis is extensively tested against the Warp particle-in-cell code [50], which uses the POISNST library to model SEE [51].

Instead of tracking individual electron trajectories, statistical theories calculate the time evolution of multipactor probabilities [27-33]. These works construct the joint probability density function that describes the probability a secondary electron impacts the opposite surface (or the emission surface). From this function, several other quantities are obtained as a function of time, such as the impact (or emission) rate on a given surface, the total SEE yield, and the total number of electrons. As in Monte Carlo simulations and particle-tracking codes, statistical theories model multipactor as a random process.

### 1.4.3 Experimental Work

As multipactor can potentially damage or even destroy modern-day technology, such systems typically undergo rigorous experimental testing to ensure multipactor-free operation. This is especially critical to the space industry, as any incidence of the discharge in space can compromise an entire mission. However, experimental testing cannot completely guarantee multipactor-free operation. This is because the discharge can be triggered by any seed electron and realistic conditions are not always possible to simulate. Further, the SEE properties of the surface material are not always accurately known and are subject to change. Thus, even after thorough experimental

testing and design, multipactor breakdown may still be inevitable. However, certain measures can be taken to significantly reduce the chance of a multipactor onset.

Recall that multipactor is strongly dependent on the SEE properties of the surface material (see Sect. 1.3.2). Some research efforts therefore examine experimental multipactor suppression techniques. For instance, surface coatings, geometrical modifications, or the addition of DC fields are often studied [14, 51-55]. Surface coatings are used to reduce the SEE coefficient of the surface material and thus potentially inhibit multipactor growth. A geometrical modification may include adjusting the gap separation between surfaces so as to eliminate resonant electron trajectories. Furthermore, a transverse DC magnetic-field may be added to induce cyclotron motion and prevent electrons from reaching and impacting the opposite surface. However, care should be taken in doing so, as a magnetic-field can potentially induce impacts at oblique angles, resulting in larger SEE yields (see Eq. 1.1).

## 1.5 Shortcomings of Conventional Theories and Approaches

Figure 1.1 portrayed multipactor as a single-resonance process, where electron impacts are synchronized with the RF electric-field. While resonance is one possible (and common) manifestation of multipactor, multipactor can also exhibit other forms. The underlying reason for this is that multipactor is an inherently nonlinear phenomenon. The discontinuity of the velocity vector at impact can lead to electron trajectories and modes that are far more complex compared to those in single-resonance multipactor. This important fact has been largely overlooked in past analyses.

Before advancing this discussion further, it is important to introduce single-surface multipactor. A single-surface impact occurs when an electron returns to impact the emission surface (rather than impacting the opposite surface). The condition for single-surface resonant multipactor is that the electron transit-time between impacts is a full multiple of the RF period, i.e.,  $t_i = M\pi/\omega$ . Here,  $M$  is an even integer corresponding to the number of full RF cycles between impacts. As in the two-surface counterpart (see Sect. 1.3.1), this condition guarantees that the next generation of secondaries experiences the same field conditions as the preceding primaries (assuming monoenergetic secondary emission). While one may expect that single-surface impacts do not contribute heavily to multipactor growth, recent studies have shown that these impacts do indeed play a considerable role in multipactor dynamics [30, 32, 56].

Recent theories predict that multipactor can exhibit forms other than single-resonance, such as hybrid-resonance [57], period- $n$  [58-59], ping-pong [60-63], or nonresonant [31, 64]. The electron trajectories for these modes are complex and, in some cases, not analytically tractable. For instance, a ping-pong mode consists of both single-surface and two-surface impacts. In a period- $n$  multipactor, the resonant impact phase alternates periodically between multiple values. These studies typically follow the standard procedure of assuming a particular mode and then deriving corresponding stability conditions and breakdown boundaries. However, this technique becomes increasingly difficult (and impractical) for high-periodicity (and nonresonant) multipactors. Thus, as introduced in this dissertation (Sect 1.7), a new approach is needed to handle these complex multipactor forms. This new model is the first comprehensive theory that recovers all such possible manifestations of multipactor.

In addition to assuming an *a priori* mode, conventional theories also often assume that secondaries generated from each impact are all emitted with the same emission energy. However, the secondary emission energy and angle are actually random variables and therefore subject to change (according to distributions). A spread in emission energies implies a spread in transit-times, which can potentially disrupt any synchronous resonance behavior. Thus, a spread in emission energies can obfuscate the multipactor boundaries derived from monoenergetic assumptions.

Stochastic models replace the monoenergetic assumption by incorporating the random nature of secondary emission (see Sect. 1.4.2). For instance, in a Monte Carlo simulation or a particle-tracking code, secondaries are emitted with a random energy (and angle) according to specified probability distributions. While these models are more consistent with actual multipacting processes, they tend to overemphasize the stochasticity of SEE, which obscures the fundamental nonlinear nature of multipactor. Further, the results can be difficult to generalize, resulting in device-specific solutions. Moreover, as the number of electrons in a multipactor simulation may be large, these approaches can have high computational cost.

Note that multipactor also occurs in more complex geometries (compared to the standard parallel-plate system). For these cases, resonance theory (Sect. 1.3.1) does not always apply. For instance, in a coaxial system, the geometry is asymmetrical and the driving RF electric-field is nonlinear and inversely proportional to the radial distance. The addition of DC fields further complicates the analysis. As a result, multipactor in coaxial systems has received far less analytical treatment compared to the standard parallel-plate geometry [32, 65-67]. Aside from stochastic models [68-72], no theory

to date comprehensively models multipactor in coaxial geometries. In Ch. 3, the new theoretical approach presented in this dissertation is expanded to a coaxial system.

## 1.6 Brief Historical Overview

In this section, a brief history of multipactor discharge is provided, covering the time period from its discovery to modern day (2019). This discussion is not intended to be an exhaustive overview but rather just highlights of some major developments. The reader is referred to Ref. [73] (and references therein) for a thorough background on the early history of multipactor.

Multipactor was observed as early as 1924 but was not identified until 1934 by Philo Farnsworth [74], the inventor of the first electronic television. Farnsworth observed multipactor in his electron cathode tubes and was interested in using SEE for his electron amplifiers, which eventually earned him several patents. Over time, however, multipactor became prevalent and posed a serious threat to upcoming microwave and space communication systems.

As the demand for multipactor suppression grew, theories on the existence of the discharge were formulated. Many scientists recognized the mechanism of resonance to be a driving force for multipactor growth. Thus, resonance theory prevailed, although somewhat different versions of the theory were put forth. In the 1950's, A.J. Hatch and H.B. Williams used one particular version of resonance theory (the constant k theory [75-76]), along with experimental-fitting, to construct universal susceptibility diagrams that portray multipactor breakdown boundaries as a function of device parameters [15-16]. In the constant k theory, the electron impact and emission

energies are assumed to be proportional (with a proportionality constant  $k$ ). Although this assumption has no physical basis and was heavily criticized, it gave reasonable agreement with experimental measurements and therefore these diagrams became an industry standard.

In 1988, Vaughan derived resonant multipactor theory assuming monoenergetic secondary emission (as opposed to the constant  $k$  assumption) [1]. Although the monoenergetic assumption is also not entirely accurate, it was considered to be more accurate than the constant  $k$  assumption and was therefore adopted by the scientific community. Using the monoenergetic assumption, Vaughan mathematically derived the concept of phase stability and constructed his own multipactor susceptibility diagrams. Today, Vaughan's paper is a classic reference and continues to be widely cited in the literature.

In 1989, Vaughan continued to contribute to multipactor research and published his empirical formula for secondary electron emission [41]. This formula specifies the SEE yield dependence on the electron impact energy/angle and the surface material properties (see Sect. 1.3.2). Today, this formula is a standard SEE model.

In the 1990's, Kishek and Lau advanced a novel model for multipactor using a resonant RF circuit [37-40]. This model aimed to address the interaction of multipactor with the surrounding RF structure and the role of saturation mechanisms (i.e., space-charge, beam loading, and frequency detuning). Additionally, these researchers also perhaps developed the first Monte Carlo model for multipactor [21], which, in the years to come, would become a standard prediction tool (see Sect. 1.4.2). Riyopolous studied the effects of space-charge debunching [35], DC magnetic-fields [77], time-delays [78],

and retarding RF fields [79] on multipactor.

In the early 2000's, the demand for high-power RF applications grew rapidly and multipactor therefore became an even more serious problem. As a result, multipactor suppression research intensified. Industry invested heavily in the development of particle-tracking codes (and Monte Carlo algorithms) for the prediction of multipactor breakdown in a variety of systems [47-50]. These codes, combined with experimental testing, resulted in the creation of multipactor prevention handbooks by the space industry [17-20]. These handbooks intended to provide the space community (and the general multipactor community) with a comprehensive reference on the state-of-the-art multipactor mitigation processes.

Further, statistical theories were developed with the hopes of establishing a reliable and predictive theory for multipactor [27-33] (see Sect. 1.4.2). Meanwhile, many researchers formulated new theoretical models for multipactor [57-64], suggesting the discharge can manifest in forms other than single-resonance (see Sect. 1.5). Shemelin [34, 80] introduced the concepts of phase maps to analyze high-periodicity multipactor and demonstrate generalized phase stability while Dexter and Seviour [81] used similar maps to construct multipactor phase charts. Moreover, experimental multipactor suppression schemes continued to be an active area of research (see Sect. 1.4.3).

Multipactor became especially pressing in the 2000's due to the prevalence of space communication systems that operated with multiple channels. These multicarrier systems, where several RF carriers (each with a separate amplitude and frequency) coexist, are difficult to analyze due to the expanded parameter space and the time-

varying signal envelope. As a result, multipactor in multicarrier systems has received little theoretical study to date despite its relevance to modern-day space-borne systems [26, 82-87]. Industrial design-standards are based on empirical rules that have no theoretical basis, such as the “20 gap-crossing-rule”, which states that multipactor takes place if the carrier envelope exceeds the breakdown voltage for a time equal or higher than the time it takes an electron to cross the gap 20 times [88]. In Ch. 4, the new theoretical approach presented in this dissertation is generalized to multicarrier operation and verified for a two-carrier system. This model serves as the first comprehensive theoretical solution for multipactor in multicarrier systems.

## 1.7 Introduction to Map-Based Multipactor Theory

Traditionally, theoretical studies for multipactor rely on two approaches: a.) analytical treatment of simple resonance modes or b.) stochastic models. The former makes simplified assumptions on the electron trajectories (i.e., resonance, monoenergetic secondary emission) to establish multipactor boundaries while the latter is not comprehensive and can be computationally expensive. As discussed in Sect. 1.5, multipactor can manifest in a variety of forms, placing further limitations on these approaches. Thus, a more general and comprehensive theory is needed.

In this dissertation, a new theoretical approach for multipactor based on principles from nonlinear dynamics and chaos theory is introduced and demonstrated for a variety of systems. The central insight behind this approach is that the cumulative SEE yield over a sequence of impacts can be determined solely from the RF phases at each impact (along with the impact angles and surface material properties). Thus, the

electron trajectories are irrelevant and a function (i.e., a map) that relates the emission RF phase to the RF phase at the next surface impact is all the information needed to determine multipactor growth or decay. Two-surface multipactor maps have been previously studied by Riyopoulos but only with stable resonant fixed-points [59, 77]. Shemelin used the basis of maps to analyze high-periodicity multipactor and demonstrate generalized phase stability [34, 80]. Dexter and Seviour used similar phase maps to construct multipactor charts [81].

The map-based theory introduced in this dissertation makes no *a priori* resonance assumptions on the electron trajectories. Instead, it models multipactor as a complex dynamical system, where iterative maps track the RF phases at the surface impacts. By systematically applying these maps and scanning system parameters, a plethora of multipacting modes are recovered. This information is combined with the SEE properties of the surface material to compute the multipactor exponential growth rate throughout parameter space. This approach is universal in that different systems can be studied by simply changing the underlying equations.

In the following chapters, this new theoretical approach is illustrated for a wide range of systems, including parallel-plate (Ch. 2), coaxial (Ch. 3), and multicarrier (Ch. 4). Here, the theoretical predictions are verified with resonance theory, particle-in-cell simulations, industrial design standards, and experimental data. This model serves as the first comprehensive theory for multipactor in coaxial and multicarrier systems. If necessary, the reader is referred to Appendix A for a brief overview of the relevant concepts and terminology from chaos theory that pertain to this dissertation.

## 1.8 Assumptions

The core assumptions made throughout this thesis are as follows:

1. A near-perfect vacuum (i.e.,  $P \ll 10^{-4}$  Torr) is assumed. Thus, the electron mean-free path length exceeds the gap separation and electron collisions can be safely neglected. Under this assumption, corona (or gas discharges) and electron ionization can also be safely ignored [89].
2. Space-charge effects (and any other saturation mechanisms) are neglected. This is justified as the main interest of this research is on the initiation of multipactor.
3. As impact energies that give rise to multipactor are far below the electron rest energy (see Table 1.1), nonrelativistic dynamics are used in the analysis.
4. As multipactor electron velocities are low ( $v \ll c$ ), the effects of the RF magnetic-field are not included.
5. Initially, monoenergetic secondary emission and a fixed emission angle are assumed. Subsequently, more realistic distributions of secondary emission energies and angles are incorporated into the analysis (see Sect. 2.2.3).
6. No time-delay between the impact of a primary and the emission of the resulting secondaries is assumed, i.e., the impact phase of a primary is the emission phase of the resulting secondaries. Note that including a time-delay is dynamically equivalent to including a spread in emission energies.
7. For simplicity, the transverse geometry dimensions are assumed to be much larger than the gap separation between the surfaces. Thus, a 1D infinite parallel-plate model is assumed (Ch.'s 2 and 4) while electron motion along the axial length of a coaxial geometry is not considered (Ch. 3).

8. Vaughan's SEE model (Eq. 1.1) is assumed for the calculation of SEE yields. A modification in the SEE model is included to account for inelastic/elastic backscatter of low energetic primaries (see Sect. 1.3.2).
9. While this analysis can be applied to any surface material with known SEE properties, copper (a standard engineering material) is used in this thesis as an illustration. The theory also includes a normal DC electric-field, which can account for surface charging of dielectric materials (see Sect. 2.3).

## 1.9 Organization of Thesis

The remaining chapters of this thesis are organized as follows. Chapter 2 illustrates the new map-based theoretical approach for multipactor in a parallel-plate geometry with and without applied DC fields. These results are compared with conventional resonance theory, particle-in-cell simulations, and industrial design standards. In Ch. 3, the map-based theory is expanded to a coaxial system and validated against published simulation and experimental data. In Ch. 4, the map-based theory is generalized to multicarrier operation in a parallel-plate geometry, where several RF carries (each with a separate amplitude and frequency) are present (as commonly employed in modern-day space communication systems). Here, the simplest such case is considered, namely a two-carrier system. These theoretical predictions are compared against particle-in-cell simulations and a two-carrier susceptibility diagram is presented. In Ch. 5, the main conclusions drawn from this research are summarized and the major advantages of the map-based theory are highlighted. Future research directions are also discussed. The content of this thesis is published in Ref.'s [90-94].

# Chapter 2: Map-Based Multipactor Theory for a Parallel-Plate Geometry

## 2.1 Chapter Overview

This chapter demonstrates the new map-based multipactor theory for a parallel-plate geometry under different scenarios: a.) a normal RF electric-field (Sect. 2.2), b.) normal RF and DC electric-fields (Sect. 2.3), c.) a normal RF electric-field and a transverse DC magnetic-field (Sect. 2.4). In these sections, the theoretical predictions are compared against resonance theory and particle-in-cell simulations. Finally, multipactor susceptibility diagrams are constructed using the new theoretical approach and compared against industrial design standards (Sect. 2.5). The content from this chapter is published in Ref.'s [90-92].

## 2.2 Map-Based Theory Under an RF Electric-Field

### 2.2.1 Basic Equations and Multipactor Maps

To illustrate the map-based theory, a 1D parallel-plate geometry of gap separation  $D$  with an RF electric-field of the form  $-E_0 \sin(\omega t + \theta_0)$  and a DC electric-field  $E_{DC}$  that are both normal to the surfaces is used (Fig. 2.1a). For notation purposes, the sign of the RF field is negative in order to have positive acceleration for accelerating phases in  $[0, \pi)$ . In this chapter, the following normalized variables are used:  $\tau = \omega t$  for time,  $\bar{x} = x/D$  for position,  $\bar{v} = v/(\omega D)$  for velocity, and  $\bar{E}_0 = eE_0/(mD\omega^2)$  for the RF

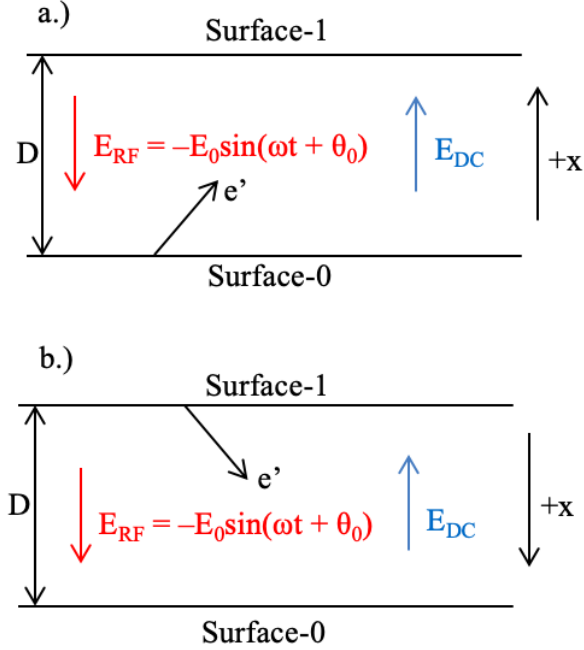


Figure 2.1: Parallel-plate geometry with gap separation  $D$  and normal RF and DC electric-fields. Direction of coordinate system for an electron emitted from a.) surface-0 and b.) surface-1.

electric-field amplitude, where  $\omega = 2\pi f$  is the RF frequency,  $-e$  is the electron charge, and  $m$  is the mass. For the time-being, monoenergetic secondary emission is assumed. Subsequently, in Sect. 2.2.3, a more realistic distribution of secondary emission energies is incorporated.

Using the normalized notation, the Lorentz force law (Eq. 2.1) is integrated for an electron that is launched at  $t = 0$  from the plate at  $x = 0$  with a fixed perpendicular velocity component  $v_{0x}$  to obtain the velocity (Eq. 2.2) and position (Eq. 2.3):

$$\ddot{x} = (e/m)(E_0 \sin(\omega t + \theta_0) - E_{DC}), \quad (2.1)$$

$$\bar{v}(\tau, \theta_0) = -\bar{E}_0(\cos(\tau + \theta_0) - \cos(\theta_0) + \eta\tau) + \bar{v}_{0x}, \quad (2.2)$$

$$\bar{x}(\tau, \theta_0) = -\bar{E}_0(\sin(\tau + \theta_0) - \sin(\theta_0) - \tau \cos(\theta_0) + \frac{1}{2}\eta\tau^2) + \tau\bar{v}_{0x}. \quad (2.3)$$

Here,  $\eta = E_{DC}/E_0$  is the ratio of the electric-field amplitudes. The normalized two-surface transit-time  $\tau_{01}$  for an electron emitted from surface-0 to reach surface-1 is determined by setting  $\bar{x} = 1$  in Eq. 2.3:

$$0 = -\sin(\tau_{01} + \theta_0) + \sin(\theta_0) + \tau_{01}(\cos(\theta_0) + \bar{v}_{0x}/\bar{E}_0) - \frac{1}{2}\eta\tau_{01}^2 - 1/\bar{E}_0. \quad (2.4)$$

The last term on the right-hand side of Eq. 2.4 contains the gap height dependence for the two-surface transit-time. To account for the possibility of single-surface impacts within the two-surface geometry, the normalized single-surface transit-time  $\tau_{00}$  for an electron to return to impact surface-0 is also calculated by setting  $\bar{x} = 0$  in Eq. 2.3:

$$0 = -\sin(\tau_{00} + \theta_0) + \sin(\theta_0) + \tau_{00}(\cos(\theta_0) + \bar{v}_{0x}/\bar{E}_0) - \frac{1}{2}\eta\tau_{00}^2. \quad (2.5)$$

In Eq.'s 2.4 and 2.5, the subscripts of  $\tau$  designate the surface of emission and surface of impact, respectively. As electrons can impact either surface, both transit-times are calculated. In this section, the DC electric-field is turned off (i.e.,  $\eta = 0$ ) and the dynamics solely under the RF field are considered. A nonzero DC electric-field is included in Sect. 2.3.

At this point in the analysis, conventional theories often assume resonance:  $\tau_{01} = N\pi$  and  $\tau_{00} = M\pi$ , where  $N(M)$  is an odd (even) integer representing the number of half (full) RF cycles between impacts [1]. Here, no such restrictions are applied, allowing for the recovery of both resonant and non-resonant modes. To construct the map for this system, the minimum transit-time is first selected:

$$\tau_{\min}(\theta_0|\bar{E}_0, \bar{v}_{0x}) = \min(\tau_{01}(\theta_0|\bar{E}_0, \bar{v}_{0x}), \tau_{00}(\theta_0|\bar{E}_0, \bar{v}_{0x})). \quad (2.6)$$

In Eq. 2.6,  $\tau_{01}(\theta_0|\bar{E}_0, \bar{v}_{0x})$  and  $\tau_{00}(\theta_0|\bar{E}_0, \bar{v}_{0x})$  are the normalized two-surface and single-surface transit-times for an emission phase  $\theta_0$  (under given system parameters  $\bar{E}_0$  and  $\bar{v}_{0x}$ ) as determined by the earliest nonnegative roots of Eq's 2.4 and 2.5, respectively. The minimum transit-time is taken to consistently account for the possibility of impacts on either surface. As shown later, this procedure recovers the ping-pong modes. For given system parameters  $\bar{E}_0$  and  $\bar{v}_{0x}$ , the map relating an emission phase  $\theta_0$  to the RF phase at the next impact is given by:

$$M_0(\theta_0|\bar{E}_0, \bar{v}_{0x}) = \begin{cases} \text{mod}(\theta_0 + \tau_{00}(\theta_0|\bar{E}_0, \bar{v}_{0x}), 2\pi), & \tau_{\min}(\theta_0|\bar{E}_0, \bar{v}_{0x}) = \tau_{00}(\theta_0|\bar{E}_0, \bar{v}_{0x}) \\ \text{mod}(\theta_0 + \tau_{01}(\theta_0|\bar{E}_0, \bar{v}_{0x}) + \pi, 2\pi), & \tau_{\min}(\theta_0|\bar{E}_0, \bar{v}_{0x}) = \tau_{01}(\theta_0|\bar{E}_0, \bar{v}_{0x}) \end{cases} \quad (2.7)$$

Equation 2.7 can be understood as a vector operator, which for an input list of emission phases, outputs a corresponding list of subsequent impact phases. Note that impact phases resulting from two-surface transits are shifted by  $\pi$ . This is due to the change in location of the origin of the coordinate system, which is placed at the emission surface on each iteration. As the emission surface switches on each two-surface transit, so does the direction of the positive surface normal. Thus, the addition of  $\pi$  to the impact phase accounts for the change in sign of the RF field under the flipped coordinate system for the subsequent iteration (see Fig. 2.1b).

To construct the map given by Eq. 2.7, the transit-times  $\tau_{01}$  and  $\tau_{00}$  can be numerically solved according to Eq's 2.4 and 2.5, respectively, from any root-finding solver. In this chapter, two root-finding solvers are used: a Newton-Raphson algorithm and a sign-detection algorithm. Before further explaining the theoretical approach, these two root-finders are first briefly described here.

The Newton-Raphson root-solver uses Newtons Method to iteratively compute the roots of a given equation. In using this root-solver, care is taken to ensure that a solution exists, that the iterations converge, and that the earliest nonnegative (and nonzero) root is selected. In practice, these conditions are satisfied by using multiple initial guesses. Roots that occur for values larger than a cutoff value  $\tau_{\max}$  are neglected. The reason for doing so is that these solutions represent high-order multipactors with large transit-times that are unlikely to contribute to electron growth. In this analysis, this cutoff value is chosen as  $\tau_{\max} = 50$  radians, corresponding to roughly 8 RF periods. If no root is found for a particular phase, it is not used to construct the map.

The sign-detection root-solver discretizes the equation of interest (as a function of the normalized transit-time) and systematically evaluates its value until a change of sign occurs, indicating the earliest root. A more accurate value of the root is then obtained by applying linear interpolation. As in the Newton-Raphson root-finder, roots larger than  $\tau_{\max}$  are neglected.

While the sign-detection algorithm is guaranteed to result in the correct root, the Newton-Raphson root-solver is more computationally efficient and also gives high-accuracy results. Thus, for large-scale scans that require numerous map constructions, the Newton-Raphson root-finder is employed. However, for constructing single maps or bifurcation diagrams (to be shown later), the sign-detection root-solver is used. Both root-solvers are thoroughly tested.

As an example, Fig. 2.2 shows the map (Eq. 2.7) for fixed system parameters  $\bar{E}_0 = 0.50$  and  $\bar{v}_{0x} = 0.10$ . Recall that the map selects the minimum transit-time (Eq. 2.6). For a visual aid on the dynamics, the map is color-coded according to impact

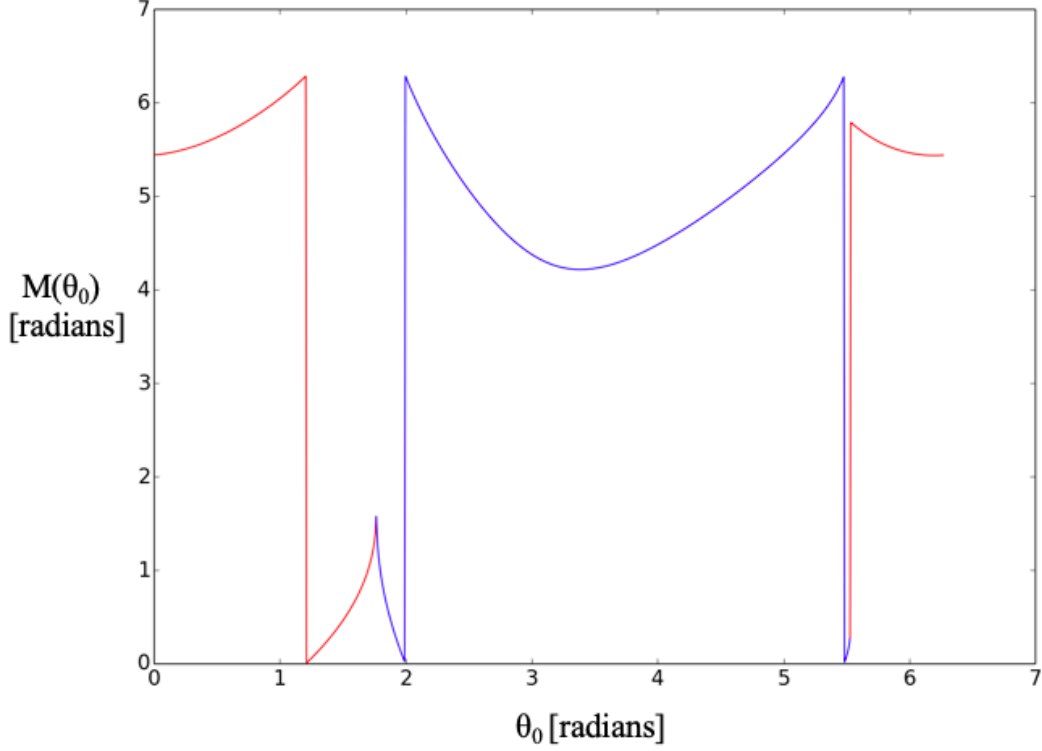


Figure 2.2: Multipactor map (Eq. 2.7) relating an emission phase  $\theta_0$  to the phase at the next impact for fixed system parameters  $\bar{E}_0 = 0.50$ ,  $\bar{v}_{0x} = 0.10$ , and  $\eta = 0$ . The map is color-coded according to impact phases resulting from two-surface transits (red) and single-surface transits (blue).

phases resulting from two-surface transits (red) and single-surface transits (blue).

Given an initial emission phase  $\theta_0$ , the RF phase at all subsequent impacts can be tracked by repeatedly iterating Eq. 2.7. Recall that no time-delay between the impact of a primary and the emission of the resulting secondaries is assumed (see Sect. 1.8). After a sufficient number of map iterations, the dynamics cease to change as orbits converge and get trapped in the attractor, which is defined as the set of values that

random orbits converge towards [95]. Unlike conventional theories, no *a priori* assumptions on the form of the attractor are made.

## 2.2.2 Bifurcation Diagrams and Comparison to Resonance Theory

As the map (Eq. 2.7) depends on the parameters  $\bar{E}_0$  and  $\bar{v}_{0x}$ , the attractor changes as these parameters are varied. In nonlinear dynamics, the attractor dependence on a system parameter is represented on a bifurcation diagram [95]. Figure 2.3 shows a bifurcation diagram constructed by scanning  $\bar{E}_0$  in the range 0.10-1.20 for 400 steps with a fixed  $\bar{v}_{0x} = 0.03$ . The vertical axis is the RF attractor phase at impact and is displayed symmetrically in  $[-\pi, \pi]$ . The bifurcation diagram is constructed as follows. For each value of  $\bar{E}_0$  on the diagram, the map is constructed with a resolution of one million RF phases from the procedure described earlier. Sixty-four random emission phases (particles) are selected to advance through the map, a sufficient sample to reach all stable attractors of the system. Each particle is then iterated five thousand times through the map to allow each orbit to converge to its attractor. The first four thousand iterations are discarded because only the attractor is of interest and not the transient dynamics leading to it. Each unique phase in the last thousand iterations constitutes the system attractor.  $\bar{E}_0$  is then incremented and this process is repeated.

Although the attractor can be better approximated with more initial particles and map advances, the chosen numerical parameters give sufficiently accurate results to justify the qualitative conclusions made later in this thesis and are thoroughly tested. Recall that the map (Eq. 2.7) tracks two-surface and single-surface transits on each

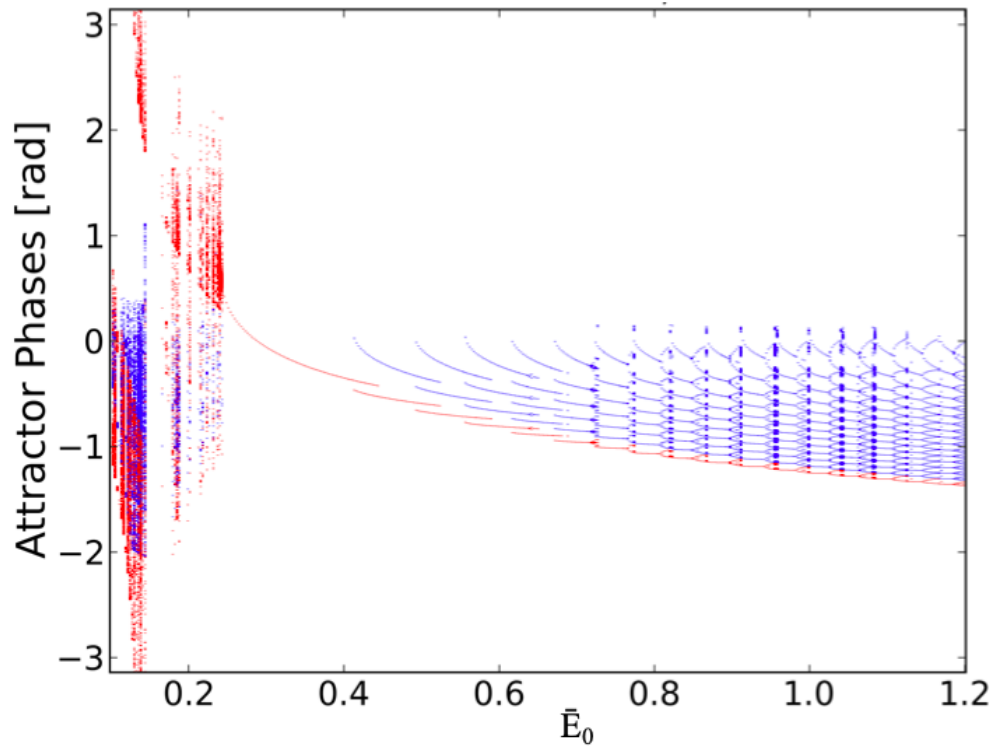


Figure 2.3: Bifurcation diagram constructed by scanning  $\bar{E}_0$  in  $[0.10, 1.20]$  for a fixed  $\bar{v}_{0x} = 0.03$  and  $\eta = 0$ . Attractor phases resulting from two-surface transits and single-surface transits are shown in red and blue, respectively.

iteration by selecting the appropriate (minimum) transit time (Eq. 2.6). For a visual aid on the dynamics, the bifurcation diagram is color coded according to impact phases resulting from two-surface transits (red) and single-surface transits (blue).

Note that the structure of the attractor changes considerably as a function of  $\bar{E}_0$ . For a specified RF field frequency and gap separation, varying  $\bar{E}_0$  is equivalent to varying the RF field amplitude, or vice-versa, varying the gap separation for a fixed RF field amplitude and frequency. For  $\bar{E}_0$  between 0.10-0.24 (see Fig. 2.4 for a zoomed-in view), the attractor is chaotic, as impacts occur over a large RF phase range with no

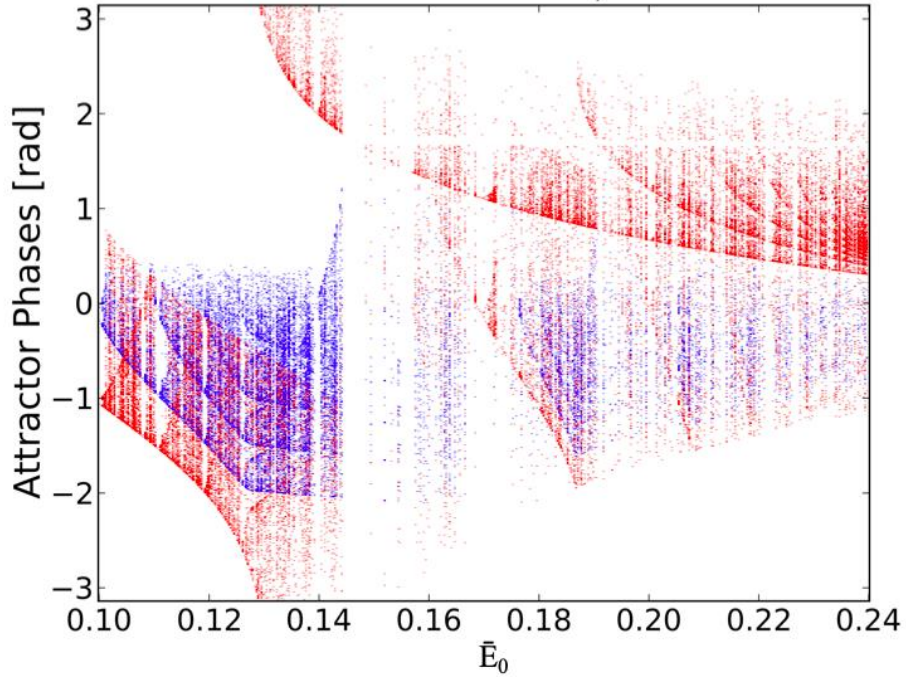


Figure 2.4: Zoomed-in view of Fig. 2.3 for  $\bar{E}_0$  between 0.10-0.24.

periodicity. Despite the low RF field strength and large gap separation in this parameter region (small  $\bar{E}_0$ ), electrons nonetheless traverse the gap for two-surface impacts (indicated by red points).

As  $\bar{E}_0$  further increases, all orbits converge to a single RF impact phase, representing a two-surface fixed-point attractor. As  $\tau_{01} = \pi$  for this fixed-point attractor, the mode is identified as a first-order ( $N = 1$ ) two-surface resonance. From conventional resonance theory [1], the range of RF field amplitudes in a parallel-plate system that give rise to two-surface resonant multipactor is obtained by setting  $\tau_{01} = N\pi$  in Eq. 2.4, resulting in:

$$\bar{E}_0 = \frac{1 - N\pi\bar{v}_{0x}}{2 \sin(\theta_0) + N\pi \cos(\theta_0)}. \quad (2.8)$$

In Eq. 2.8,  $\theta_0$  is a phase from the basin of attractor phases that converges to stable resonant behavior of order  $N$ . For zero emission velocity ( $\bar{v}_{0x} = 0$ ), stability requirements restrict  $\theta_0$  to the range  $[0, \arctan(2/N\pi)]$ . For a first-order resonance ( $N = 1$ ), the upper phase bound is  $\theta_{0u} \approx 0.567$  radians, corresponding to a lower normalized RF electric-field bound of  $\bar{E}_{0l} \approx 0.243$ .

For nonzero emission velocity,  $\theta_{0u}$  and  $\bar{E}_{0l}$  remain a good estimate but the lower phase boundary  $\theta_{0l}$  can become negative [1, 79], as electrons are able to escape an initial retarding field and reach the opposite surface. Specifically,  $\theta_{0l}$  is the maximum negative phase (i.e., cutoff phase) such that the secondary electron initially reverses back to the plate of origin and then, after the RF field switches sign, reverses again just before a single-surface impact. For a given  $\bar{v}_{0x}$  and order  $N$ , this cutoff phase and corresponding upper field boundary can be obtained by implicitly solving Eq. 2.8. For  $\bar{v}_{0x} = 0.03$  and  $N = 1$ , this gives  $\theta_{0l} \approx -0.427$  radians and  $\bar{E}_{0u} \approx 0.446$ . These stability boundaries are in excellent agreement with the bifurcation diagram (see Fig. 2.5), which depicts the two-surface fixed-point resonant attractor well within the calculated basin of attraction for the corresponding parameter region. Thus, this new model recovers the findings from resonance theory for first-order ( $N = 1$ ) multipactor.

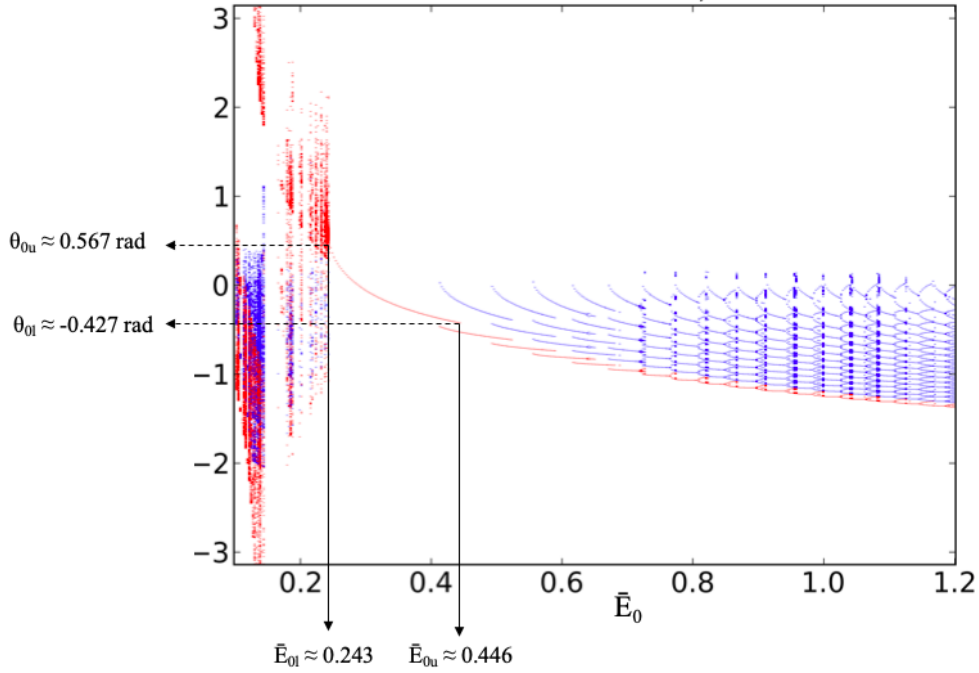


Figure 2.5: First-order ( $N = 1$ ) two-surface resonance stability boundaries recovered by the bifurcation diagram in Fig. 2.3 for  $\bar{v}_{0x} = 0.03$ .

As  $\bar{E}_0$  nears  $\bar{E}_{0u}$ , the fixed-point resonant attractor becomes unstable and new two-surface modes appear that spread even further into the decelerating RF phase regime. As  $\bar{E}_0$  further increases, these attractors undergo period doubling, bifurcating into separate stable attractors. Note that some of the period doublings are not true bifurcations, as the period- $2n$  cycle is disconnected from the preceding period- $n$  attractor. This can be understood by noting that Eq. 2.7 is not a pure map but rather a composition of two separate maps (two-surface and single-surface). Even more, single-surface impacts (blue points) begin to appear together with the two-surface impacts and follow a similar pattern. This combination of single-surface and two-surface impacts is the signature of the ping pong modes [60-63]. Here, these ping-pong multipactor modes

cycle periodically through multiple single-surface and two-surface impacts.

Note that orbits guided by the map converge to stable attractor point(s) and are repelled from unstable points. Thus, with a sufficient sample of emission phases, the bifurcation diagram recovers all stable modes of the discharge over the entire parameter range. This methodology is far more comprehensive than the standard approach of applying stability conditions for different known modes (such as resonance) to establish multipacting boundaries [1, 15-16].

A bifurcation diagram can also be constructed by instead fixing  $\bar{E}_0$  and scanning the other free parameter  $\bar{v}_{0x}$ . This is shown in Fig. 2.6 for a fixed  $\bar{E}_0 = 0.70$  and a  $\bar{v}_{0x}$  scan between 0.020-0.80. For a fixed frequency-gap product, scanning  $\bar{v}_{0x}$  is equivalent to varying the average secondary electron emission energy, a property of the surface material. As in the  $\bar{E}_0$  scan, multipactor takes on different forms. For low emission velocities, the attractor is largely single-surface chaotic as the low energy electrons return to the emission surface. As  $\bar{v}_{0x}$  is increased, periodic ping-pong modes begin to form as electrons now have sufficient energy to engage in two-surface impacts. In particular, a period-2 ping-pong multipactor is observed between 0.18-0.52, where electrons alternate between a single-surface and a two-surface impact. Finally, the period-2 ping-pong attractor transitions to chaos for higher emission velocities, where electrons can now engage in more complex orbits. Note that the chaotic regions contain period windows where the attractor temporarily shifts to a low-periodicity limit cycle [95]. Here, a slight change in parameter space can result in a completely different orbit.

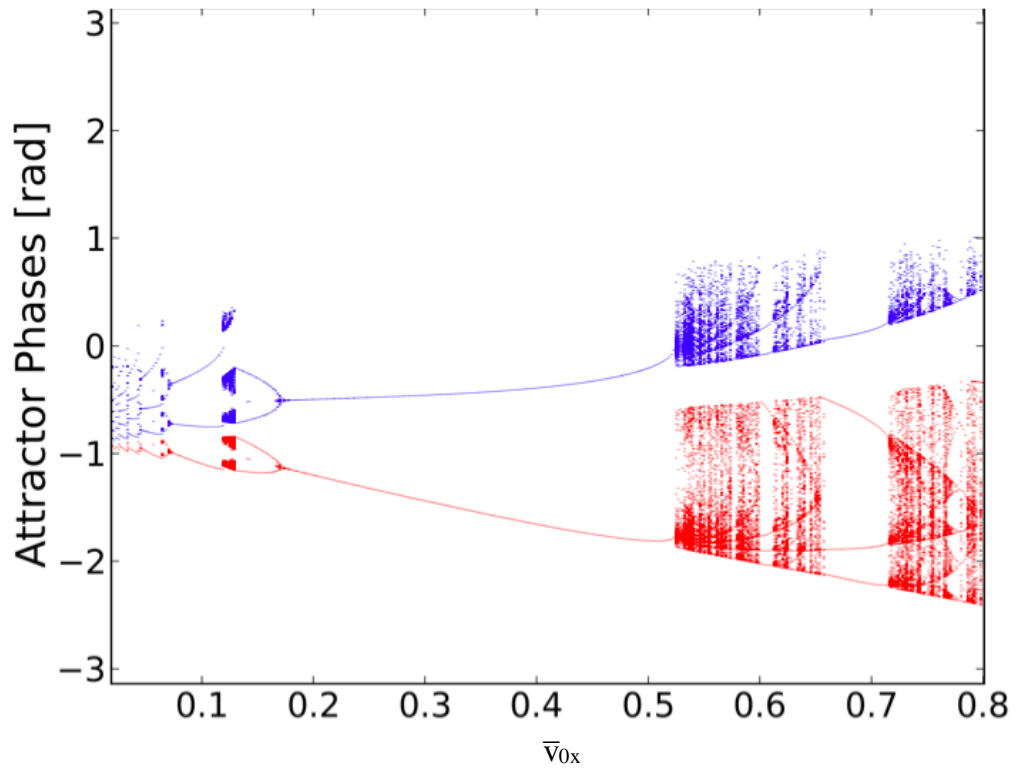


Figure 2.6: Bifurcation diagram constructed by scanning  $\bar{v}_{0x}$  in  $[0.02, 0.80]$  for a fixed  $\bar{E}_0 = 0.70$  and  $\eta = 0$ . Attractor phases resulting from two-surface transits and single-surface transits are shown in red and blue, respectively.

### 2.2.3 Multipactor Exponential Growth Rate and Incorporation of Spreads in Secondary Emission Energies and Angles

The multipactor maps and bifurcation diagrams are a function of the fields and geometry. To obtain a quantitative analysis, the secondary emission properties of the surface material need to also be considered. To calculate the secondary electron emission (SEE) yield, defined as the average number of emitted secondaries per incident primary, Vaughan's formula (Eq. 1.1) is used with a modification accounting for backscattered and reflected primaries, as described in Sect. 1.3.2.

The SEE parameters in Vaughan's formula are material dependent. In this thesis, copper material is chosen. The incident angle for an electron impact at an RF attractor phase  $\theta_a$  is  $\theta_I = \arctan(\bar{v}_y/\bar{v}(\tau_a, \theta_a))$ , where  $\bar{v}(\tau_a, \theta_a)$  is the normal component of the impact velocity (normalized) given by Eq. 2.2 and  $\tau_a$  is the corresponding normalized transit-time. Note that  $\tau_a$  can correspond to a single-surface or two-surface transit-time depending on whether the impact at phase  $\theta_a$  results from a single-surface or two-surface transit.  $\bar{v}_y$  is the normalized transverse component (parallel to the surfaces) of the impact velocity, which remains constant as the electric-fields are normal to the surfaces. For the time-being,  $\bar{v}_y = \bar{v}_{0x}$  so as to assume a fixed emission angle. A random emission energy and angle are incorporated later in this section. The impact energy (expressed in eV) at an attractor phase  $\theta_a$  is given by  $W = \frac{m}{2e} (\bar{v}^2(\tau_a, \theta_a) + \bar{v}_y^2)(\omega D)^2$ .

The exponential growth rate for a bifurcation scan is given by:

$$\lambda(\eta, \bar{E}_0, \bar{v}_{0x}) = \omega \frac{\ln(\prod_i \delta_{\theta_i} \prod_j \delta_{\theta_j})}{\sum_i \tau_{\theta_i} + \sum_j \tau_{\theta_j}}. \quad (2.9)$$

In Eq. 2.9,  $\delta_{\theta_i}$  is the SEE yield (Eq. 1.1a) resulting from an impact at RF attractor phase  $\theta_i$  with corresponding transit-time  $\tau_{\theta_i}$ . The indices  $i$  and  $j$  span over points in the surface-0 and surface-1 system attractor, respectively. Here, the system refers to the specified map parameters  $(\eta, \bar{E}_0, \bar{v}_{0x})$  and the corresponding map(s) given by Eq. 2.7. In the absence of a DC electric-field (i.e.,  $\eta = 0$ ),  $\prod_i \delta_{\theta_i} = \prod_j \delta_{\theta_j}$  and  $\sum_i \tau_{\theta_i} = \sum_j \tau_{\theta_j}$  as the attractor impact phases for each surface are identical. As to be shown in Sect. 2.3, this is generally not true for the case where  $\eta \neq 0$ .

Eq. 2.9 is a general formula that applies to all types of multipactor, including two-surface resonance where  $\sum_i \tau_{\theta_i} + \sum_j \tau_{\theta_j} = 2N\pi$  (the factor of 2 is included because the left-hand side is the two-way transit-time) [96]. It is convenient to express the exponential growth rate in terms of the average SEE yield over an RF period  $T = 2\pi/\omega$ :  $\delta_{\text{avg}} = e^{\lambda T}$ . Using Eq. 2.9,  $\delta_{\text{avg}}$  can be equivalently expressed as:

$$\delta_{\text{avg}}(\eta, \bar{E}_0, \bar{v}_{0x}) = \left( \prod_i \delta_{\theta_i} \prod_j \delta_{\theta_j} \right)^{\frac{1}{\frac{\sum_i \tau_{\theta_i} + \sum_j \tau_{\theta_j}}{2\pi}}}. \quad (2.10)$$

Figure 2.7 shows the average SEE yield (black curve) given by Eq. 2.10 over the bifurcation diagram from Fig. 2.3, assuming an RF frequency of  $f = \omega/2\pi = 500$  MHz and a gap separation of  $D = 7$  mm. Note that the average SEE yield is large in the parameter region that supports the two-surface resonant attractor and small in regions that support chaotic and high-periodicity modes. The fluctuations in the curve arise from the period-windows within the chaotic regions, where the attractor temporarily takes on a low-periodicity form.

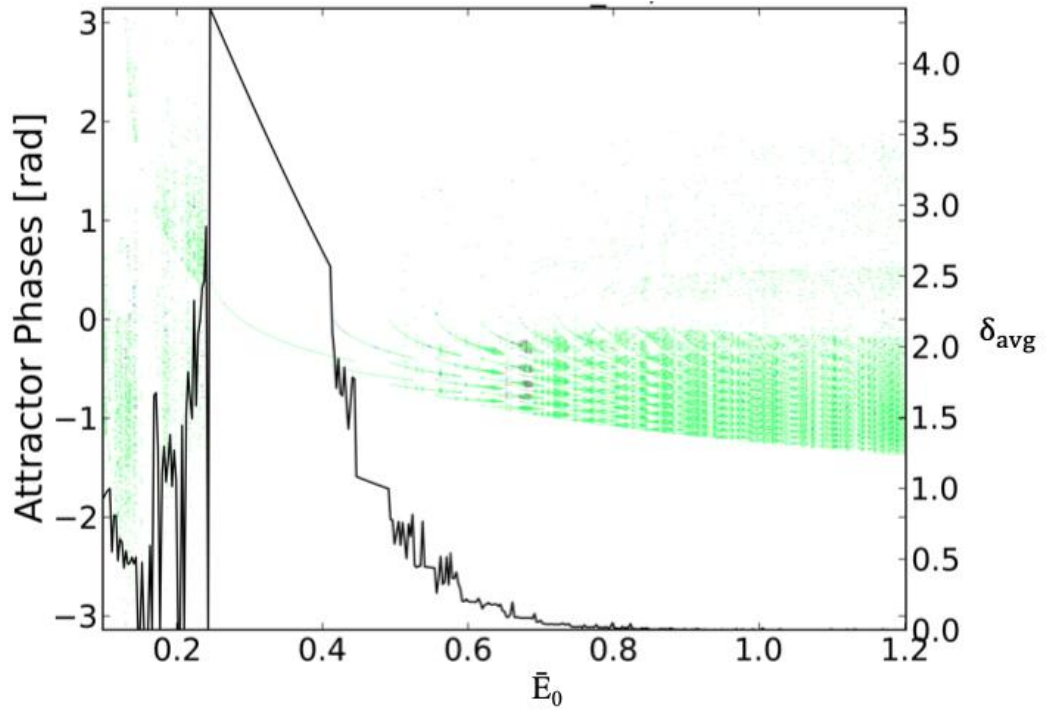


Figure 2.7: Average SEE yield over an RF period (black curve) for the  $\bar{E}_0$  scan in Fig. 2.3 (scale shown on right). The RF frequency and gap separation are  $f = 500$  MHz and  $D = 7$  mm, respectively. For each scan, a monoenergetic emission  $\bar{v}_{0x} = 0.03$  is assumed and the DC electric-field is turned off ( $\eta = 0$ ).

Note that Eq's 2.9 and 2.10 describe the case of monoenergetic secondary emission (i.e., a fixed  $\bar{v}_{0x}$ ). As discussed in Ch. 1, the secondary emission energy (and angle) are actually random variables and therefore described by distributions. To incorporate a spread in secondary emission energies, the parameter  $\bar{v}_{0x}$  is scanned (for given values of  $\bar{E}_0$  and  $\eta$ ). The scan range of  $\bar{v}_{0x}$  is consistently chosen to include emission energies on the order of an eV to a few tens of eVs. For each  $(\bar{E}_0, \eta, \bar{v}_{0x})$  combination, the corresponding map(s) (Eq. 2.7), attractor, and average SEE yield  $\delta_{\text{avg}}(\bar{E}_0, \eta, \bar{v}_{0x})$  (Eq. 2.10) are systematically calculated (it will be shown in Sect. 2.3 that two separate maps are required for the case where  $\eta \neq 0$ ). To obtain the effective SEE yield over an RF period (Eq. 2.12), the average SEE yields obtained from the monoenergetic  $\bar{v}_{0x}$  scans are integrated over an exponential distribution with expected value  $\bar{v}_{0x\text{avg}}$  (Eq. 2.11):

$$f(\bar{v}_{0x}) = \frac{1}{\bar{v}_{0x\text{avg}}} e^{-\bar{v}_{0x}/\bar{v}_{0x\text{avg}}}, \quad (2.11)$$

$$\delta_{\text{eff}}(\bar{E}_0, \eta) = \int \delta_{\text{avg}}(\bar{E}_0, \eta, \bar{v}_{0x}) f(\bar{v}_{0x}) d\bar{v}_{0x}. \quad (2.12)$$

This procedure is similar to the reconstruction of kinetic plasma modes from a monoenergetic fluid model [97]. For systems with transverse fields (see Sect. 2.4 and Ch. 3), the transit-times and SEE yields are also sensitive to the emission angle. Thus, including an emission angle scan is also important for these cases. For these systems, the transverse emission velocity ( $\bar{v}_{0y}$ ) is an additional map parameter. To incorporate an emission energy and angle scan, several maps are constructed, each with a different combination of  $(\bar{v}_{0x}, \bar{v}_{0y})$  corresponding to an emission velocity magnitude of  $\bar{v}_0 = \sqrt{\bar{v}_{0x}^2 + \bar{v}_{0y}^2}$  and an emission angle  $\phi = \arctan(\bar{v}_{0x}/\bar{v}_{0y})$  (defined with respect to the

surface tangential). As before, the scan range of emission energies includes values from an order of an eV to a few tens of eVs. For each value of  $\bar{v}_0$ , the emission angle  $\phi$  is varied between  $[0, \pi]$  radians. For a given combination of  $(\bar{v}_0, \phi)$ , the normalized emission velocities are  $\bar{v}_{0x} = \bar{v}_0 \sin(\phi)$  and  $\bar{v}_{0y} = \bar{v}_0 \cos(\phi)$ . For each map constructed in the emission energy and angle scan, the corresponding map attractor and average SEE yield (Eq. 2.10) are computed. As before, to obtain an effective value, the average SEE yields are integrated over corresponding secondary emission distributions:

$$\delta_{\text{eff}}(\bar{E}_0, \eta) = \iint \delta_{\text{avg}}(\bar{E}_0, \eta, \bar{v}_0, \phi) f_1(\bar{v}_0) f_2(\phi) d\bar{v}_0 d\phi. \quad (2.13)$$

In this chapter, the secondary emission velocity magnitude  $\bar{v}_0$  is taken to follow an exponential distribution (Eq. 2.11) while the secondary emission angle distribution is taken to be  $f_2(\phi) = (1/2)\sin(\phi)$  for  $0 \leq \phi \leq \pi$ , which is also commonly employed in Monte Carlo models [21-26]. Note that these emission distributions correspond to true secondaries. Although backscattered electrons may follow different distributions, this does not affect the multipactor dynamics and the qualitative results from the scans.

## 2.2.4 Comparison to Simulation

To test the predictions from this theory, a 3D simulation model using the Warp particle-in-cell code is setup. Warp is a well-established simulation tool that has demonstrated considerable success in modeling particle-accelerators and electron clouds [7]. The reader is referred to Ref. [50] for a detailed overview of the Warp code. Warp uses the POISNST library to incorporate SEE [51]. This library has an extensive description of relevant parameters for a given surface material, such as dependence of yield on impact energy/angle and a realistic velocity spread based on experimental fits.

Here, a stripline geometry (0.583 mm thick, 46 x 46 mm wide) with copper surfaces is selected. For the first set of Warp simulations, an RF frequency of  $f = 500$  MHz and a gap separation of  $D = 7$  mm are selected (corresponding to an  $fD$  product of 3.5 GHz-mm) in the absence of a DC electric-field (i.e.,  $\eta = 0$ ). For the fixed  $fD$  product, a series of simulations are run, each with a different RF electric-field amplitude  $E_0$ . The range of amplitudes is chosen so that the normalized parameter  $\bar{E}_0$  ranges between 0.10-1.20 for the purpose of comparison to Fig. 2.3. The corresponding RF electric-field amplitude for each simulation is uniquely given by  $E_0 = \bar{E}_0(m/e)D\omega^2$ , resulting in a range from 39.28 kV/m to 471.37 kV/m.

Each simulation is run for 5 RF periods with a resolution of 320 time steps per period. 100 seed electrons are injected over the first RF period on every fourth time step. For simulations with low growth rates, the number of injected seed electrons is increased to 10000 to account for the rapid loss of particles so as to maintain consistent simulation statistics. As the initiation of multipactor is mostly of interest as opposed to saturation, space-charge effects are turned off. On each time step, the electrons are advanced in space according to the influence of the RF electric-field (and any DC fields that may be included). The fields are simulated as electrostatic fields on a 3D grid and are “manually” updated on each time step. Since electron velocities are low ( $v \ll c$ ), the effects of the RF magnetic-field are not included. As electrons impact the surfaces, secondaries are emitted depending on the impact energies and angles. The total number of particles in the system is recorded on each time step and expressed in semi-log form. The slope of a least-squares linear fit gives the exponential growth (or decay) rate, from which the average SEE yield over an RF period is then obtained.

To compare the Warp simulations to the map-based theory, an emission energy scan is conducted and the effective SEE yield over an RF period  $\delta_{\text{eff}}(\bar{E}_0, \eta)$  (Eq. 2.12) is computed over the corresponding range of  $\bar{E}_0$  (with the fixed  $\eta = 0$ ). Recall that this requires constructing several monoenergetic maps (Eq. 2.7), computing the corresponding map attractors and average SEE yields (Eq. 2.10), and then integrating over the specified secondary emission velocity distribution (Eq. 2.11). To match the Warp code parameters for copper, the SEE parameters in the theory are set to  $\delta_{\text{max}0} = 2.1$ ,  $W_{\text{max}0} = 271$  eV, and  $W_c = 6$  eV (Eq. 1.1). Additionally,  $\bar{v}_{0\text{xavg}}$  is chosen to correspond to a normal emission energy of  $W_{0\text{xavg}} = 3$  eV (i.e., a total average emission energy of 6 eV as  $\bar{v}_y = \bar{v}_{0x} \rightarrow W_{0\text{avgtotal}} = 2W_{0\text{xavg}}$ ).

Figure 2.8 plots the effective SEE yield predicted by Warp and the map-based theory with an emission energy scan. Both curves from theory and simulation track closely throughout the scan. The crossover point, i.e., where the effective SEE yield intercepts unity (or equivalently where the exponential growth rate is zero), predicted by Warp and the theory is in excellent agreement. Although the bifurcation diagram in Fig. 2.3 is constructed for a monoenergetic case, it nonetheless provides a qualitative understanding on the structure of the growth rate. Initially, the growth rate steadily increases as multipactor is driven at a strong two-surface resonance. The growth rate is then reduced as the attractor transitions to high-order ping-pong modes, where the spread in impact phases dilutes multipactor growth. The different forms of multipactor recovered by this bifurcation diagram are well reflected in the growth rates predicted by the theory and simulation.

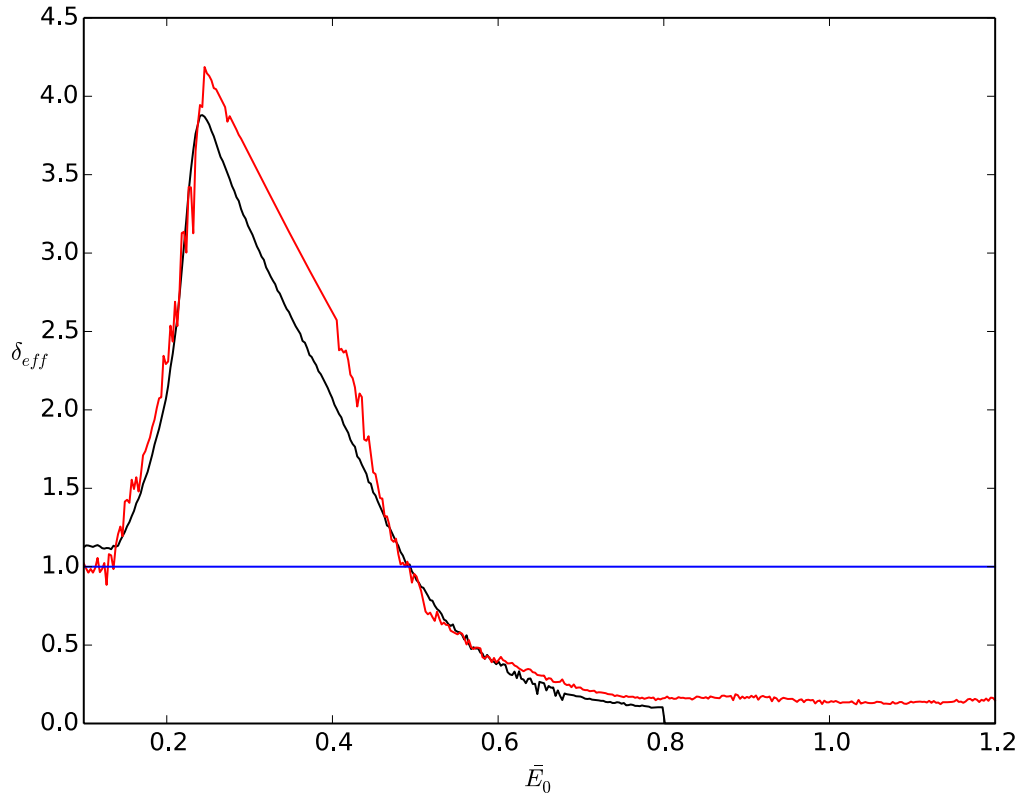


Figure 2.8: Effective SEE yield over an RF period from theory with an emission energy scan (red) and Warp simulations (black) as a function of  $\bar{E}_0$ . The RF frequency and gap separation are  $f = 500$  MHz and  $D = 7$  mm, respectively, and the DC electric-field is turned off ( $\eta = 0$ ). The corresponding RF electric-field amplitude scan range is from 39.28 kV/m to 471.37 kV/m.

## 2.3 Map-Based Theory Under RF and DC Electric-Fields

### 2.3.1 Multipactor Maps and Bifurcation Diagrams

In this section, the multipactor dynamics in the presence of both RF and DC electric-fields are explored (i.e.,  $\eta \neq 0$ ). As before, the two-surface and one-surface map equations for an emission from surface-0 are given by Eq's 2.4 and 2.5, respectively (but now with  $\eta \neq 0$ ). Recall that the direction of the positive surface normal switches on each two-surface impact due to the change in location of the coordinate system origin (see Fig. 2.1b). As a result, the fields change sign on the subsequent iteration. Thus, for each two-surface impact, the sign of the RF field for the subsequent iteration is accounted for by shifting the RF impact phase by  $\pi$  (Eq. 2.7). In addition, the sign of  $\eta$  is reversed to account for the change of sign of the DC electric-field, resulting in a separate pair of map equations:

$$0 = -\sin(\tau_{10} + \theta_0) + \sin(\theta_0) + \tau_{10}(\cos(\theta_0) + \bar{v}_{0x}/\bar{E}_0) + \frac{1}{2}\eta\tau_{10}^2 - 1/\bar{E}_0. \quad (2.14)$$

$$0 = -\sin(\tau_{11} + \theta_0) + \sin(\theta_0) + \tau_{11}(\cos(\theta_0) + \bar{v}_{0x}/\bar{E}_0) + \frac{1}{2}\eta\tau_{11}^2. \quad (2.15)$$

As before, the subscripts of  $\tau$  designate the surface of emission and surface of impact, respectively. Since the underlying equations for an emission from each surface are different, each surface has its own map ( $M_0$  and  $M_1$ ) defined by Eq's 2.6 and 2.7 but with the appropriate pair of transit-times ( $(\tau_{01}, \tau_{00})$  and  $(\tau_{10}, \tau_{11})$ ). Note that in the absence of a DC electric-field (i.e.,  $\eta = 0$ ),  $\tau_{01}(\theta_0|\eta = 0, \bar{E}_0, \bar{v}_{0x}) = \tau_{10}(\theta_0|\eta = 0, \bar{E}_0, \bar{v}_{0x})$  and  $\tau_{00}(\theta_0|\eta = 0, \bar{E}_0, \bar{v}_{0x}) = \tau_{11}(\theta_0|\eta = 0, \bar{E}_0, \bar{v}_{0x})$ . Thus,  $M_0$  and  $M_1$  are equivalent and only one map is needed to describe the system (as seen in Sect. 2.2.1).

The general procedure of advancing an emission phase in this two-map system remains the same as before but with the additional step of tracking the impact surface for each iteration. In particular, for each two-surface transit, the map used to advance the system for the subsequent iteration is switched. To illustrate this, consider electrons emitted from surface-0 at phase  $\theta_0$ . If the transit-time to the same surface is shorter, i.e.,  $\tau_{00}(\theta_0) < \tau_{01}(\theta_0)$ , the same map ( $M_0$ ) is used to further advance the system. However, if the transit-time to the opposite surface is shorter, i.e.,  $\tau_{01}(\theta_0) < \tau_{00}(\theta_0)$ , electrons traverse the gap to impact surface-1 at an RF phase  $\theta_1 = M_0(\theta_0)$ . The system is now guided by the surface-1 map ( $M_1$ ) on the subsequent iteration ( $\theta_2 = M_1(\theta_1)$ ).

Figure 2.9 shows the bifurcation diagrams for each surface resulting from scanning  $\eta$  in the range  $[-1.0, 1.0]$  with fixed system parameters  $\bar{E}_0 = 0.30$  and  $\bar{v}_{0x} = 0.03$ . Here, all electrons are assumed to be initially emitted from surface-0. As before, a random sample of emission phases is selected to repeatedly advance through the maps in order to reach the attractor. For each iteration, the impact surface is recorded to ensure the proper map is used for the subsequent map advance. The attractor phases are then separated according to their corresponding impact surface, resulting in a bifurcation diagram for each surface. This added complexity affects the computational time only minimally, as all operations are vectorized. As before, the bifurcation diagrams are color coded according to impact phases resulting from two-surface transits (red) and single-surface transits (blue).

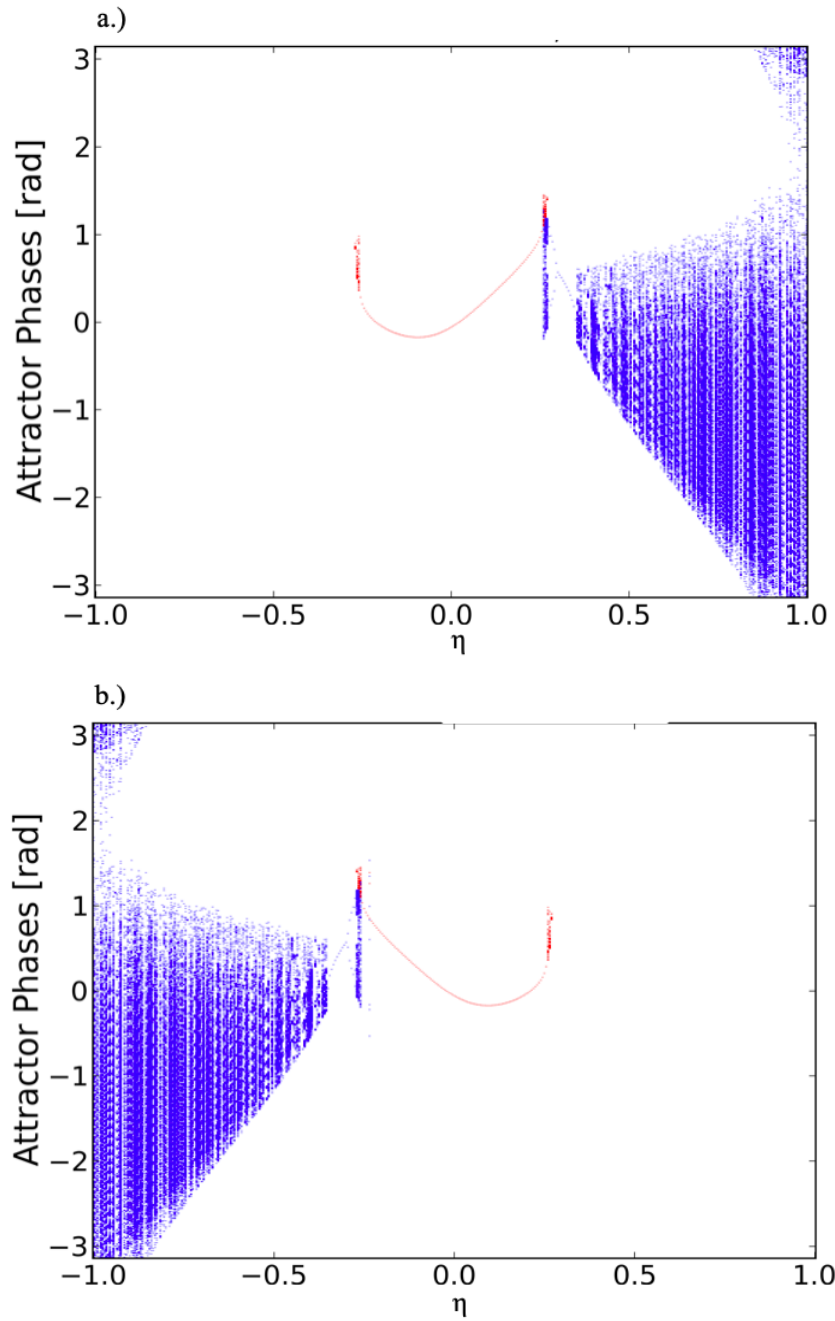


Figure 2.9: Bifurcation diagrams for a.) surface-0 and b.) surface-1 constructed by scanning  $\eta$  in  $[-1.0, 1.0]$  for a fixed  $\bar{v}_{0x} = 0.03$  and  $\bar{E}_0 = 0.30$ . Attractor phases resulting from two-surface transits and single-surface transits are shown in red and blue, respectively.

For a fixed RF electric-field amplitude, varying  $\eta$  corresponds to varying the DC electric-field strength. Note that the plots are mirror images of one another as the dynamics are identical for each surface but occur in reverse directions. This can be understood as follows. For weak DC field strengths ( $-0.30 < \eta < 0.30$ ), a two-surface resonant attractor appears on both diagrams as the RF electric-field dominates and accelerates electrons across the gap. For  $|\eta| > 0.30$ , a two-surface multipactor no longer persists and only single-surface impacts take place, eventually leading to chaos for sufficient DC field strengths. Thus, a strong DC field prevents electrons from reaching the opposite surface (resulting in no attractor for the opposite surface bifurcation diagram) and restores them to the originating surface for repeated single-surface impacts. The orientation of the DC field, or equivalently the sign of  $\eta$ , determines the attracting and repelling surfaces.

### 2.3.2 Comparison to Simulation

To test the map-based theory with a DC electric-field, a Warp simulation scan is conducted. As in Sect. 2.2.4, the RF frequency and gap separation are chosen as  $f = 500$  MHz and  $D = 7$  mm, respectively. In this section, the RF electric-field amplitude is additionally fixed and set to  $E_0 = 91.75$  kV/m (corresponding to  $\bar{E}_0 \approx 0.23358$ ) while the Warp model is expanded to also include a normal DC electric-field  $E_{DC}$ . For the fixed parameters, a series of simulations are run scanning the DC electric-field strength  $E_{DC} = \eta E_0$ , where the parameter  $\eta$  is adjusted between 0.0-1.0. The simulation parameters are identical to those in Sect. 2.2.4 and the multipactor exponential growth rate is computed from the same procedure (assuming copper material).

To compare the simulation results to the theoretical model, a bifurcation scan is constructed for the parameter  $\eta$  (and the fixed  $\bar{E}_0 = 0.23358$ ). As before, a spread in emission energies is incorporated by calculating the average SEE yield (Eq. 2.10) for multiple monoenergetic cases and then integrating over an exponential distribution (Eq. 2.11), giving an effective SEE yield for each value of  $\eta$  (Eq. 2.12). Recall that for a nonzero DC electric-field ( $\eta \neq 0$ ), a map for each surface is needed to fully describe the dynamics, resulting in two distinct sets of attractor phases (see Sect. 2.3.1). Thus, both sets of attractor phases are used to compute the average SEE yield  $\delta_{\text{avg}}(\eta, \bar{E}_0, \bar{v}_{0x})$ , as indicated by Eq. 2.10.

The effective SEE yields from the Warp simulations and the bifurcation scans from theory are shown together in Fig. 2.10 as a function of  $\eta$ . The curves closely track each other and the crossover points are in excellent agreement. As before, a bifurcation diagram constructed for a monoenergetic case (Fig. 2.11) provides an explanation on the structure. For  $\eta \approx 0$ , the growth rate is large as multipactor is driven at a strong two-surface resonance. As  $\eta$  increases, the growth rate decreases as the attractor becomes chaotic and then increases as multipactor again shifts to resonance. Finally, as  $\eta$  approaches unity, the growth rate dilutes as the attractor transitions to chaos, where the repeated low single-surface impact energies reduce the growth rate. As also seen in Sect 2.2.4, the different forms of multipactor recovered in the bifurcation diagram manifest in the growth rates predicted by theory and simulation. This finding raises an interesting research question: can multipactor be suppressed by intelligently introducing chaos?

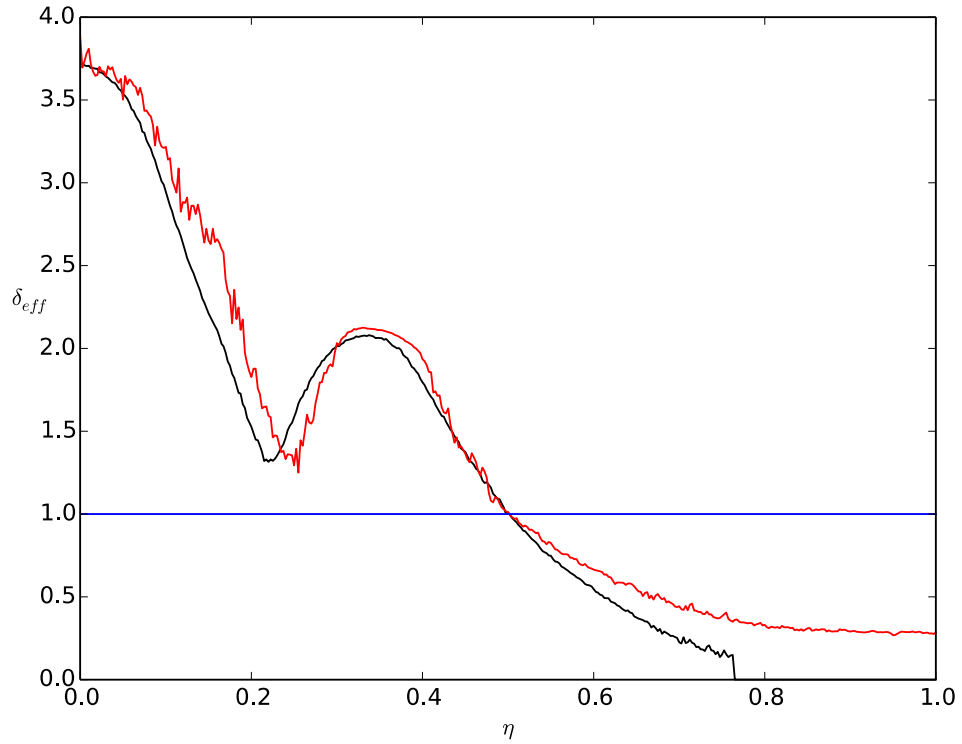


Figure 2.10: Effective SEE yield over an RF period from theory with an emission energy scan (red) and Warp simulation (black) as a function of  $\eta$ . The RF frequency, gap separation, and RF field amplitude are  $f = 500$  MHz,  $D = 7$  mm, and  $E_0 = 91.75$  kV/m, respectively, corresponding to  $\bar{E}_0 \approx 0.23358$ . The corresponding DC electric-field scan range is from 0 kV/m to  $E_0$ .

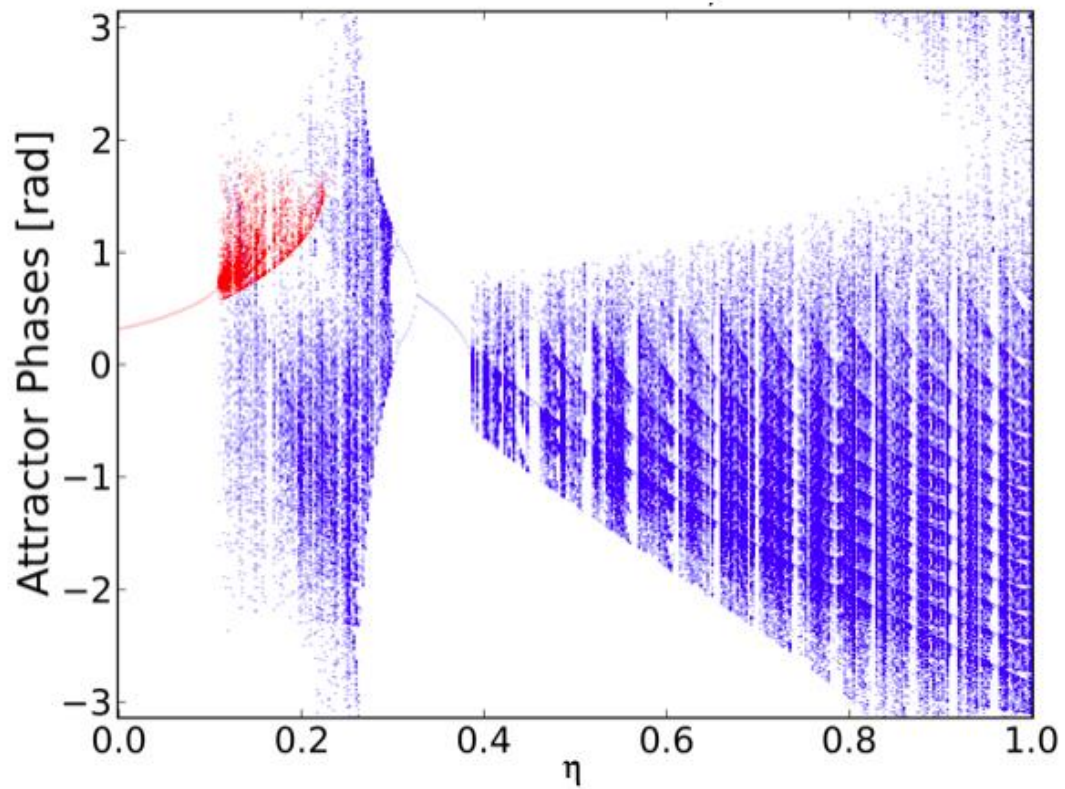


Figure 2.11: Bifurcation diagram for surface-0 constructed by scanning  $\eta$  for a monoenergetic  $\bar{v}_{0x} = 0.05$  and a fixed  $\bar{E}_0 = 0.23358$ . Attractor phases resulting from two-surface transits and single-surface transits are shown in red and blue, respectively.

## 2.4 Map-Based Theory with a Transverse DC Magnetic-Field

### 2.4.1 Basic Equations, Bifurcation Diagrams, and Comparison to Resonance Theory

In this section, the map-based multipactor theory is expanded to include to a transverse DC magnetic-field (Fig. 2.12). This configuration is commonly found in cross-field devices [54-55, 77-79]. Here, the same procedure developed in the previous sections of this chapter is used but with modified equations for the transit-times. The Lorentz force-law for the system is given by:

$$\ddot{x} + \omega_c \dot{y} = \frac{e}{m} E_0 \sin(\omega t + \theta_0), \quad (2.16)$$

$$\ddot{y} - \omega_c \dot{x} = 0. \quad (2.17)$$

In Eq's 2.16 and 2.17,  $\omega_c = eB_{DC}/m$  is the cyclotron frequency. The solutions to these equations (in normalized form) for an electron emitted at  $t = 0$  from surface-0 with normal and transverse emission velocities  $v_{0x}$  and  $v_{0y}$ , respectively, are:

$$\begin{aligned} \bar{x}(\tau, \theta_0) = & \frac{\bar{E}_0}{\Omega^2 - 1} \left( \sin(\tau + \theta_0) - \sin(\theta_0) \cos(\Omega\tau) - \frac{\cos(\theta_0) \sin(\Omega\tau)}{\Omega} \right) + \\ & \frac{\bar{v}_{0x}}{\Omega} \sin(\Omega\tau) - \frac{\bar{v}_{0y}}{\Omega} (1 - \cos(\Omega\tau)), \end{aligned} \quad (2.18)$$

$$\begin{aligned} \bar{y}(\tau, \theta_0) = & \frac{\bar{E}_0}{\Omega^2 - 1} \left( -\Omega \cos(\tau + \theta_0) - \sin(\theta_0) \sin(\Omega\tau) - \frac{\cos(\theta_0)(1 - \Omega^2 - \cos(\Omega\tau))}{\Omega} \right) + \\ & \frac{\bar{v}_{0x}}{\Omega} (1 - \cos(\Omega\tau)) + \frac{\bar{v}_{0y}}{\Omega} \sin(\Omega\tau). \end{aligned} \quad (2.19)$$

In Eq's 2.18 and 2.19,  $\Omega = \omega_c/\omega$  is the ratio of the cyclotron frequency to the RF frequency. Note that these equations are undefined for the magnetic-field free case (i.e.,  $\Omega = 0$ ) and for  $\omega_c = \omega$  (i.e.,  $\Omega = 1$ ). The solution for the former case, where only

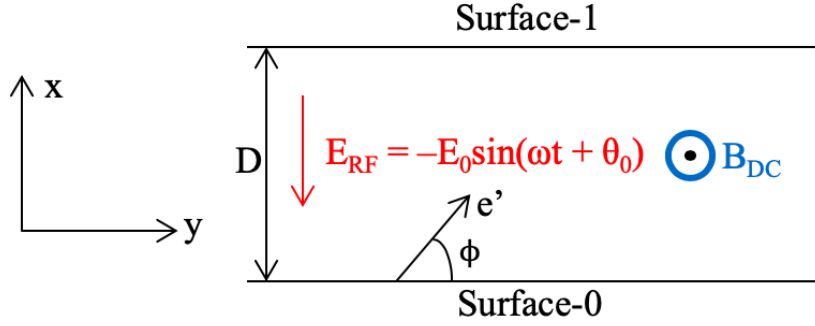


Figure 2.12: Parallel-plate geometry with normal RF electric-field and a transverse DC magnetic-field. Here,  $\phi$  is the emission angle with respect to the surface tangential.

the RF electric-field is present, is given by Eq. 2.3 (with  $\eta = 0$ ). The solution for the latter case can be obtained by taking the limits of Eq's 2.18 and 2.19 as  $\Omega \rightarrow 1$ .

In this study, the transverse geometry dimensions are taken to be much larger than the gap separation  $D$ . Thus, the  $y$ -component of the electron trajectory (Eq. 2.19) is neglected in the calculation of the transit-times. However, the transverse velocity ( $d\bar{y}(\tau, \theta_0)/d\tau$ ) affects the impact energy/angle and hence is relevant for the SEE yield.

The normalized two-surface (single-surface) transit-time  $\tau_{01}$  ( $\tau_{00}$ ) for an electron to impact surface-1 (surface-0) is given by setting  $\bar{x} = 1$  ( $\bar{x} = 0$ ) in Eq. 2.18:

$$\frac{1}{\bar{E}_0} = \frac{1}{\Omega^2 - 1} \left( \sin(\tau_{01} + \theta_0) - \sin(\theta_0) \cos(\Omega\tau_{01}) - \frac{\cos(\theta_0) \sin(\Omega\tau_{01})}{\Omega} \right) + \frac{\bar{v}_{0x}}{\bar{E}_0 \Omega} \sin(\Omega\tau_{01}) - \frac{\bar{v}_{0y}}{\bar{E}_0 \Omega} (1 - \cos(\Omega\tau_{01})). \quad (2.20)$$

$$0 = \frac{1}{\Omega^2 - 1} \left( \sin(\tau_{00} + \theta_0) - \sin(\theta_0) \cos(\Omega\tau_{00}) - \frac{\cos(\theta_0) \sin(\Omega\tau_{00})}{\Omega} \right) + \frac{\bar{v}_{0x}}{\bar{E}_0 \Omega} \sin(\Omega\tau_{00}) - \frac{\bar{v}_{0y}}{\bar{E}_0 \Omega} (1 - \cos(\Omega\tau_{00})). \quad (2.21)$$

As before, the subscripts of  $\tau$  designate the surface of emission and surface of impact, respectively, and no resonance assumptions are made, allowing for the recovery of all possible modes. For given parameters  $\bar{E}_0, \Omega, \bar{v}_{0x}$ , and  $\bar{v}_{0y}$ , the map relating an emission phase  $\theta_0$  to the phase at the next impact is given by Eq's 2.6 and 2.7 but with  $\tau_{01}$  and  $\tau_{00}$  now determined by the earliest (nonnegative and nonzero) roots of Eq's 2.20 and 2.21, respectively. Here, the transit-time dependence on the emission phase and the system parameters is implied. Note that the transit-times are symmetric with respect to the DC magnetic-field, i.e.,  $\tau_{01} = \tau_{10}$  and  $\tau_{00} = \tau_{11}$ . This is in contrast to the case where a normal DC electric-field is present in the gap, where a separate map for each surface is required (see Sect. 2.3.1).

Figure 2.13 shows a bifurcation diagram constructed by scanning  $\bar{E}_0$  in the range 0.10-1.20 with fixed parameters  $\Omega = 0.50$  and  $\bar{v}_{0x} = \bar{v}_{0y} = 0.03$ . The diagram is constructed from the same procedure described in Sect. 2.2.2. For  $\bar{E}_0$  between 0.10-0.37, all orbits converge to a single impact phase, representing a single-surface (indicated by blue) fixed-point attractor. As  $\tau_{00} = 2\pi$  for these phases, this mode is identified as a first-order ( $M = 1$ ) single-surface resonance. Here, the low RF electric-field strength and the large gap separation (small  $\bar{E}_0$ ) combined with the DC magnetic-field prevents two-surface transits across the gap. As  $\bar{E}_0$  further increases, all orbits again converge to a single RF impact phase but now with two-surface impacts (indicated by red). As  $\tau_{01} = \pi$  for these fixed-point attractor phases, this mode is identified as first-order ( $N = 1$ ) two-surface resonance. To compare these findings with resonance theory, the fixed-phase equation is obtained by setting  $\tau_{01} = N\pi$  in Eq. 2.20, resulting in:

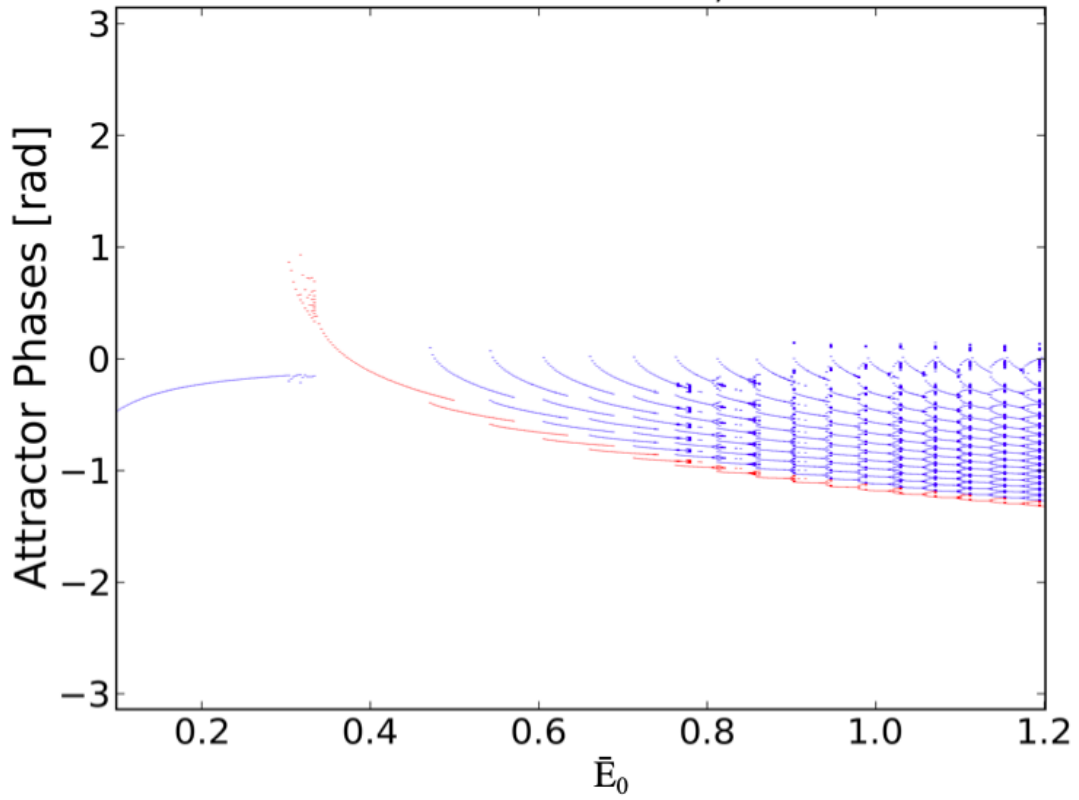


Figure 2.13: Bifurcation diagram constructed by scanning  $\bar{E}_0$  in  $[0.10, 1.20]$  for a fixed  $\bar{v}_{0x} = \bar{v}_{0y} = 0.03$  and  $\Omega = 0.50$ . Attractor phases resulting from two-surface transits and single-surface transits are shown in red and blue, respectively.

$$\bar{E}_0 = \frac{\left(1 - \frac{\bar{v}_{0x}}{\Omega} \sin(\Omega N \pi) + \frac{\bar{v}_{0y}}{\Omega} (1 - \cos(\Omega N \pi))\right) (\Omega^2 - 1)}{-\sin(\theta_0) - \sin(\theta_0) \cos(\Omega N \pi) - \frac{\cos(\theta_0) \sin(\Omega N \pi)}{\Omega}}. \quad (2.22)$$

Note that in the absence of a DC magnetic-field (i.e.,  $\Omega = 0$ ), Eq. 2.22 reduces to Eq. 2.8. The upper phase stability bound is the phase that minimizes Eq. 2.22 (or equivalently maximizes the denominator of Eq. 2.22) for given values of  $\Omega$  and  $N$ , resulting in  $\theta_{0u} = \tan^{-1}(\Omega(1 + \cos(\Omega N \pi))/\sin(\Omega N \pi))$ . In the absence of a DC magnetic-field (i.e.,  $\Omega = 0$ ), this expression reduces to  $\tan^{-1}(2/(N\pi))$ , which is the well-known result derived by Vaughan [1]. For a first-order ( $N = 1$ ) resonance and  $\Omega = 0.50$ ,  $\theta_{0u} \approx 0.464$  radians, corresponding to a lower normalized RF electric-field bound of  $\bar{E}_{0l} \approx 0.335$ .

As explained in Sect. 2.2.2, the lower phase bound  $\theta_{0l}$  boundary is obtained by implicitly solving Eq. 2.22 for the maximum negative emission phase such that the electron escapes a single-surface impact (for a given emission energy) and impacts the opposite surface with a resonance transit-time [1, 79]. For  $\Omega = 0.50$ ,  $\bar{v}_{0x} = \bar{v}_{0y} = 0.03$ , and  $N = 1$ , this gives  $\theta_{0l} \approx -0.371$  radians and  $\bar{E}_{0u} \approx 0.50$ . These stability boundaries are in excellent agreement with the bifurcation diagram (see Fig. 2.14). Thus, as also found in Sect. 2.2.2, the map-based theory recovers first-order ( $N = 1$ ) resonant multipactor. As  $\bar{E}_0$  nears  $\bar{E}_{0u}$ , the two-surface resonant attractor becomes unstable and high-periodicity ping-pong modes begin to appear, where multiple single-surface and two-surface impacts occur periodically.

A bifurcation diagram can also be constructed by instead scanning  $\Omega$  and fixing  $\bar{E}_0$ ,  $\bar{v}_{0x}$ , and  $\bar{v}_{0y}$ . This is shown in Fig. 2.15 for a  $\Omega$  scan between 0.0-1.50 and a fixed  $\bar{E}_0 = 0.23358$  and  $\bar{v}_{0x} = \bar{v}_{0y} = 0.05$ . For a fixed RF frequency, scanning  $\Omega$  is equivalent

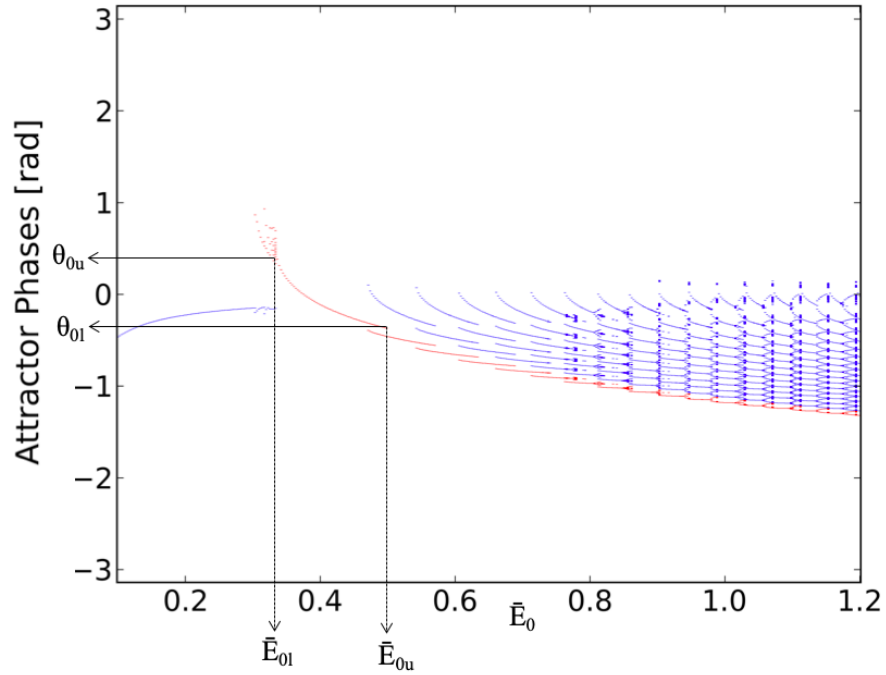


Figure 2.14: First-order ( $N = 1$ ) two-surface resonance stability boundaries recovered by the bifurcation diagram in Fig. 2.13 for  $\Omega = 0.50$  and  $\bar{v}_{0x} = \bar{v}_{0y} = 0.03$ .

to varying the DC magnetic-field strength. For  $\Omega \approx 0$ , two-surface resonance dominates, as the magnetic-field is not strong enough to drive electrons away from resonance. As  $\Omega$  increases, the attractor transitions to chaos, where both two-surface and single-surface impacts occur over a large phase range with no periodicity. For  $\Omega > 0.37$ , the attractor manifests as a single-surface period- $n$  (limit) cycle, where the phase at each single-surface impact alternates between multiple values.

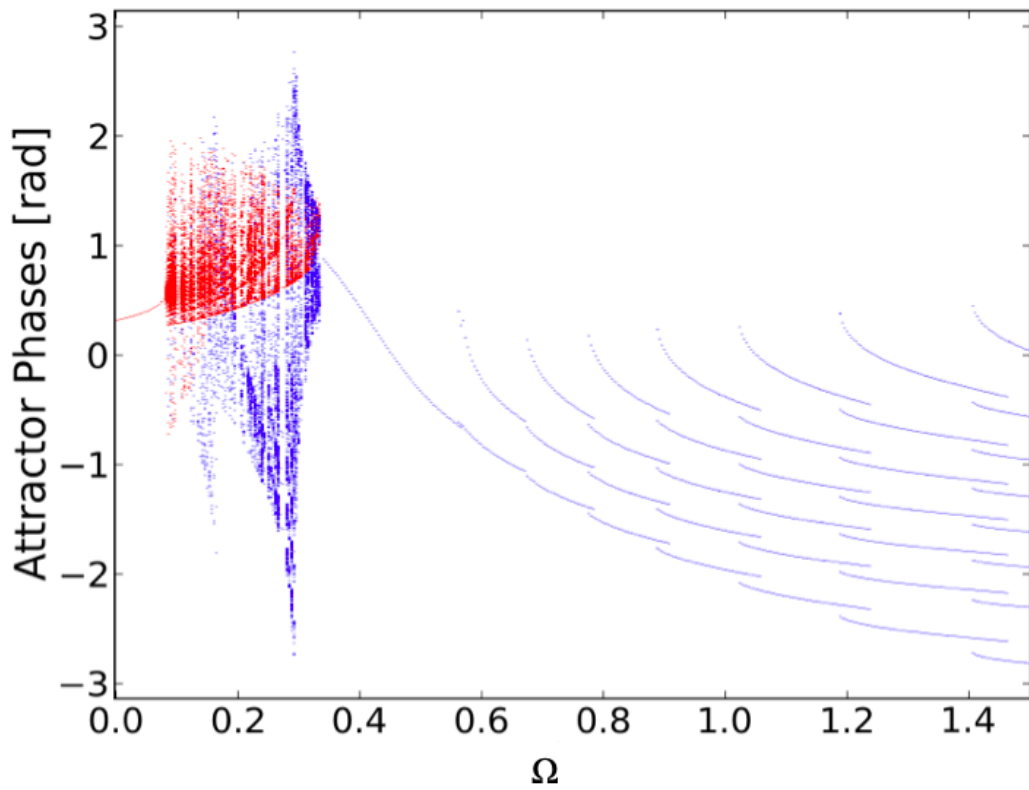


Figure 2.15: Bifurcation diagram constructed by scanning  $\Omega$  in  $[0.0, 1.50]$  for a fixed  $\bar{E}_0 = 0.23358$  and  $\bar{v}_{0x} = \bar{v}_{0y} = 0.05$ . Attractor phases resulting from two-surface transits and single-surface transits are shown in red and blue, respectively.

## 2.4.2 Comparison to Simulation

To test the map-based theory with a transverse DC magnetic-field, a Warp simulation scan is conducted. As previously, the RF frequency, gap separation, and RF amplitude are set to  $f = 500$  MHz,  $D = 7$  mm, and  $E_0 = 91.75$  kV/m (corresponding to  $\bar{E}_0 \approx 0.23358$ ), respectively. Here, a transverse DC magnetic-field  $B_{DC}$  is also included in the Warp model. A series of simulations are run scanning the DC magnetic-field strength  $B_{DC} = (m/e)\omega\Omega$ , where  $\Omega$  is adjusted between 0.0-1.50 (for the purpose of comparison to Fig. 2.15). The corresponding DC magnetic-field scan range is from 0 mT to 27 mT. The simulation parameters are the same as before and the multipactor exponential growth rate is calculated in a similar way (assuming copper material).

To compare the simulation results to the theoretical model, a bifurcation scan is constructed for the parameter  $\Omega$  (with a fixed  $\bar{E}_0 = 0.23358$ ) in the same range. A spread in emission energies and angles is incorporated by calculating the average SEE yield  $\delta_{avg}(\bar{E}_0, \Omega, \bar{v}_{0x}, \bar{v}_{0y})$  (Eq. 2.10) for multiple monoenergetic and fixed emission angle cases and then integrating over the specified secondary emission distributions, resulting in an effective value for each  $\Omega$  (Eq. 2.13 but with  $\eta$  replaced by  $\Omega$ ).

The effective SEE yields from Warp and theory are shown together in Fig. 2.16 as a function of  $\Omega$ . The curves again are in good agreement. As before, a bifurcation diagram constructed for a monoenergetic case with a fixed emission angle (Fig. 2.15) provides a qualitative explanation on the structure. For  $\Omega \approx 0$ , the growth rate is large as multipactor is driven at a strong two-surface resonance. As  $\Omega$  increases, the effective SEE yield decreases as the attractor transitions to chaotic and high-periodicity forms, where the spread in impact phases dilutes multipactor growth.

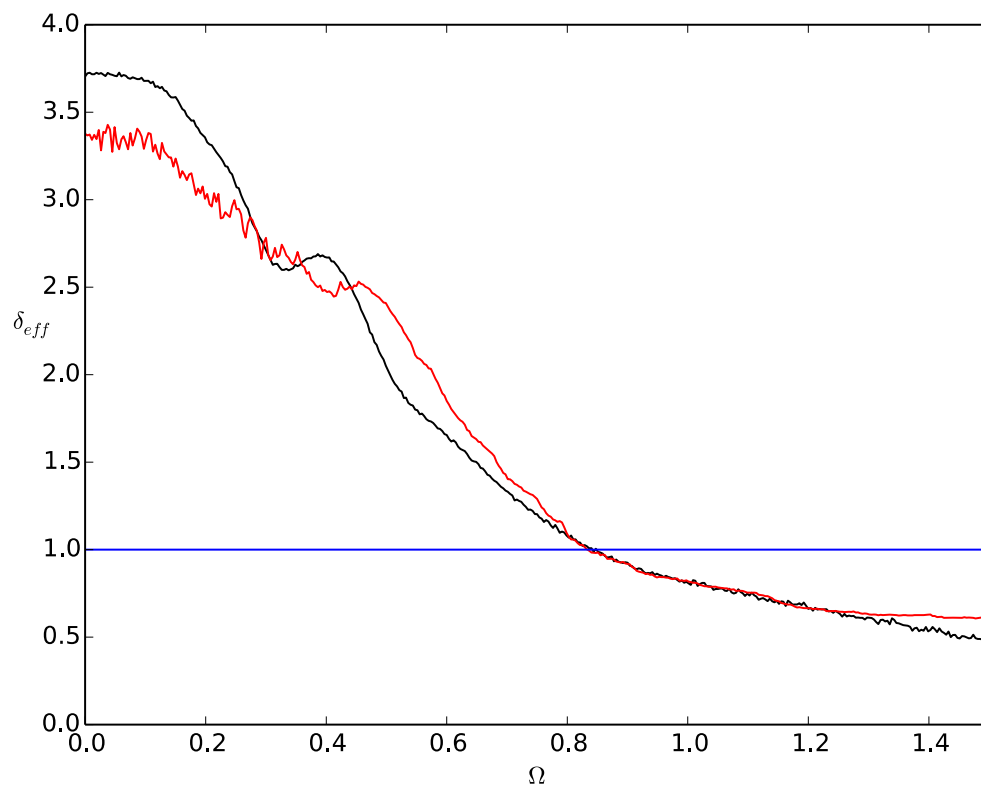


Figure 2.16: Effective SEE yield over an RF period from theory with an emission energy scan (red) and Warp simulation (black) as a function of  $\Omega$ . The RF frequency, gap separation, and RF field amplitude are  $f = 500$  MHz,  $D = 7$  mm, and  $E_0 = 91.75$  kV/m, respectively, corresponding to  $\bar{E}_0 \approx 0.23358$ . The corresponding DC magnetic-field scan range is from 0 mT to 27 mT.

## 2.5. Construction of Universal Multipactor Susceptibility Diagrams from Map-Based Theory and Comparison to Industrial Design Standards

The theoretical predictions so far have been expressed in terms of normalized variables (i.e.,  $\bar{E}_0, \eta, \Omega$ ). Engineers and industry are however interested in multipactor thresholds in terms of physical parameters, such as field amplitudes, frequencies, and geometry dimensions. Section 1.4.1 showed that combining conventional resonance theory with material considerations results in universal susceptibility diagrams that portray multipactor breakdown boundaries in the fD-voltage plane (see Fig. 1.3). In this section, the map-based theory is used to construct similar multipactor susceptibility diagrams for a parallel-plate geometry. These results are then compared to industrial design standards and particle-in-cell simulations.

Figure 2.17 shows a susceptibility diagram constructed from the map-based theory for copper material ( $\delta_{\max 0} = 2.25, W_{\max 0} = 175$  eV). This diagram is constructed as follows. First, all DC fields are turned off (i.e.,  $\eta = \Omega = 0$ ) and only the RF electric-field is considered. Without any loss of generality, the RF frequency is taken to be  $f = \omega/2\pi = 1$  GHz. Additionally,  $V_0 = E_0 D$  is defined as the RF voltage amplitude. For each (fD,  $V_0$ ) coordinate on the diagram,  $\delta_{\text{eff}}(\bar{E}_0)$  (Eq. 2.13) is calculated, where the parameter  $\bar{E}_0 = eV_0/(mD^2\omega^2)$  is completely determined by the fD product and  $V_0$ .

To display the multipactor boundaries, contours corresponding to different values of  $\delta_{\text{eff}}$  are shown (blue for  $\delta_{\text{eff}} = 0.50$ , black for  $\delta_{\text{eff}} = 1.0$ , green for  $\delta_{\text{eff}} = 2.0$ , orange for  $\delta_{\text{eff}} = 3.0$ , and red for  $\delta_{\text{eff}} = 4.0$ ). The black contours corresponding to  $\delta_{\text{eff}} = 1$

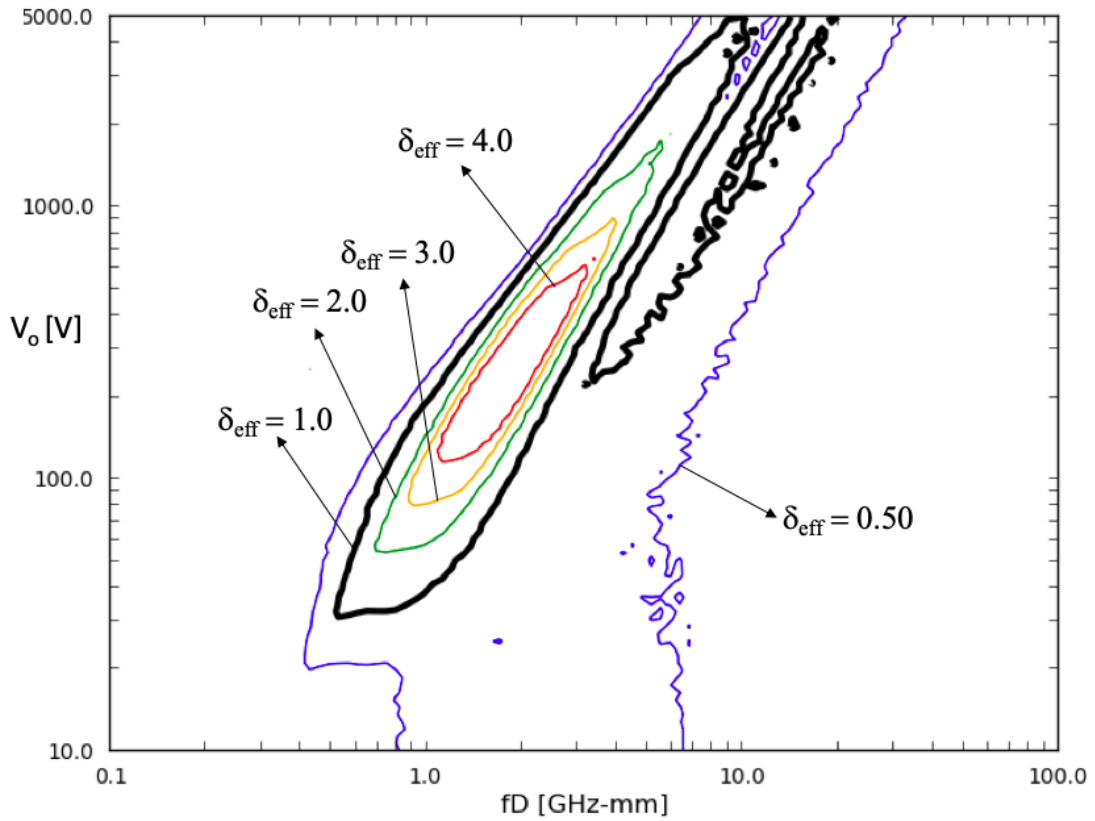


Figure 2.17: Multipactor susceptibility diagram (log-log plot) for copper material in the absence of DC fields (i.e.,  $\eta = \Omega = 0$ ) constructed from the map-based theory. Here, the RF frequency is  $f = 1$  GHz. Contours corresponding to different magnitudes of  $\delta_{\text{eff}}$  are shown. The black contours are the multipacting boundaries.

represent the multipactor boundary (i.e., where the multipactor exponential growth rate is zero). Thus, parameter regions within these black contours support multipactor growth (i.e.,  $\delta_{\text{eff}} > 1.0$ ) while parameter regions outside these contours support multipactor decay (i.e.,  $\delta_{\text{eff}} < 1.0$ ). Note that the diagram is plotted on a log-log scale.

To test these theoretical predictions, consider the European Space Agency (ESA) design standard for copper material [18]. This design standard is shown (dashed lines) on top of the original susceptibility diagram (Fig. 2.17) in Fig. 2.18, where each separate margin is labeled either as ‘1’, ‘2’, or ‘3’. Note that this design standard is first constructed from the susceptibility diagrams derived by Hatch and Williams [15-16] from resonance theory and then adjusted according to experimental tests.

As seen in Fig. 2.18, the susceptibility diagram from theory and the ESA design standard have considerable overlap and predict similar multipacting regimes. However, margins 1 and 3 overestimate the theoretical bounds while margin 2 underestimates. To test the theoretical predictions relative to the design standard, Warp simulations are run at several parameter points on the susceptibility diagram. These results are shown in Fig. 2.19 (indicated by the crosses). Here, red crosses are placed in areas of multipactor growth (i.e.,  $\delta > 1$ ) while black crosses are placed in areas of multipactor decay (i.e.,  $\delta < 1$ ). Note that the simulations predict multipactor decay right inside margins 1 and 3 (indicated by the black crosses close to these margins), which is also supported by the theory as these points are outside the black contours. The simulations also show that multipactor persists beyond margin 2 (indicated by the red crosses below margin 2), which is also supported by the theory, as these points are within the black contours.

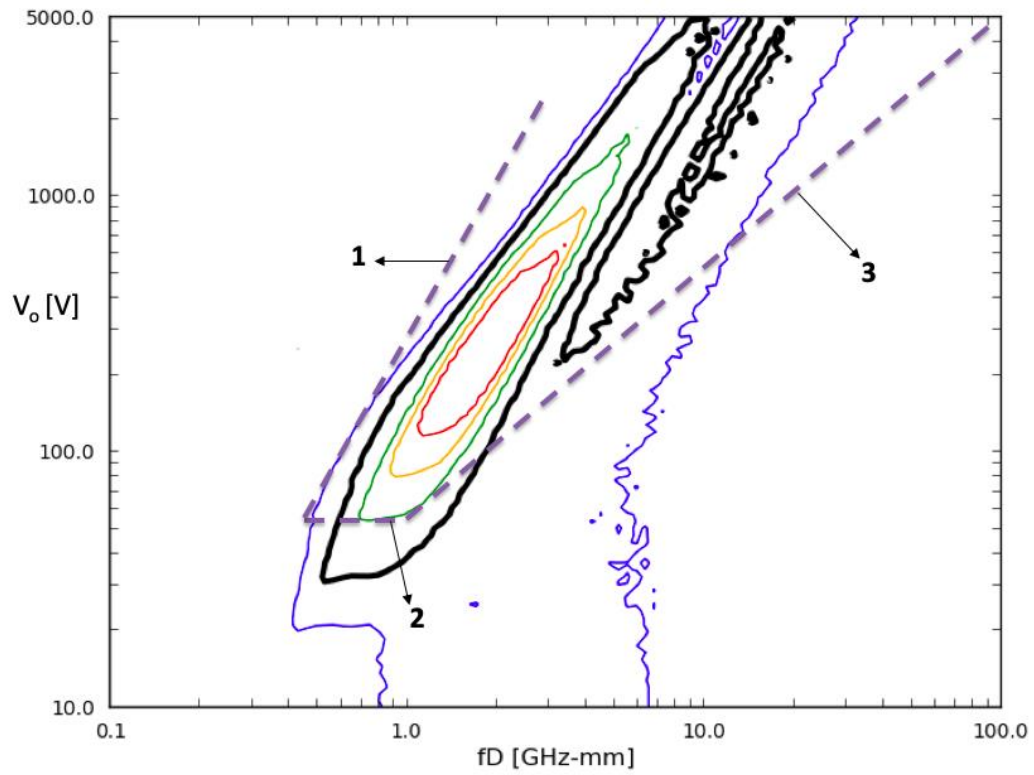


Figure 2.18: European Space Agency (ESA) design standard [18] (dashed lines) for copper material shown on top of the susceptibility diagram from theory (Fig. 2.17). Here, each separate design margin is labeled either as ‘1’, ‘2’, or ‘3’.

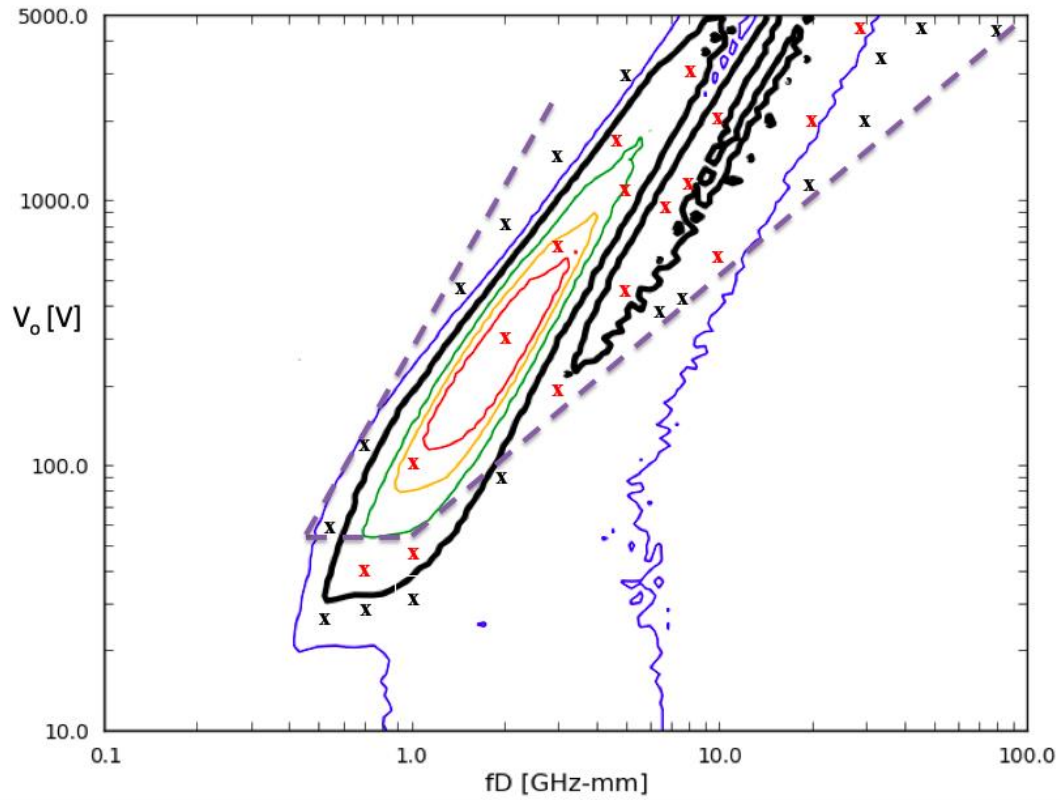


Figure 2.19: Results from particle-in-cell simulations (crosses) at various points on the susceptibility diagram from theory. Here, red crosses are placed on parameter regions that support multipactor growth (i.e.,  $\delta > 1$ ) while black crosses are placed on parameter regions that support multipactor decay (i.e.,  $\delta < 1$ ).

This expanded susceptibility space occurs for low fD products ( $\sim 1$  GHz-mm), which have been previously shown to support ping-pong modes that involve combined single-surface and two-surface impacts [60-63]. In fact, a detailed look at the maps in this parameter space (and the corresponding attractors) reveals that these regions do indeed support ping-pong multipactor. Note that these high-periodicity modes are not recovered by single-resonance theory and thus parameter regions that support such modes (and give an effective SEE yield greater than unity) are likely to go unidentified by conventional susceptibility diagrams. However, the map-based theory scans all of parameter space with no *a priori* assumptions, allowing for the recovery of all multipactor modes.

Note that a few multipactor points predicted by the simulations are not predicted by the theory (i.e., red crosses that lie outside the black contours). This can be attributed to differences in the SEE emission model used by the theory and the simulation code (recall that the theory uses a SEE model based on the modified Vaughan's formula (Eq. 1.1) while the simulation code uses a more complex emission model as specified by the POISNST library). Nonetheless, multipactor parameter regions predicted by simulation do remain within the blue contour from theory, which gives a reliable estimate of the overall susceptibility boundary.

Figure 2.20 shows a susceptibility diagram constructed from the map-based theory using a transverse DC magnetic-field strength of  $B_{DC} = 10$  mT (corresponding to  $\Omega \approx 0.28$ ). The diagram is constructed from the same procedure as before but now with the corresponding nonzero  $\Omega$ . Compared to the zero magnetic-field case (Fig. 2.17), this particular magnetic-field strength broadens the multipactor

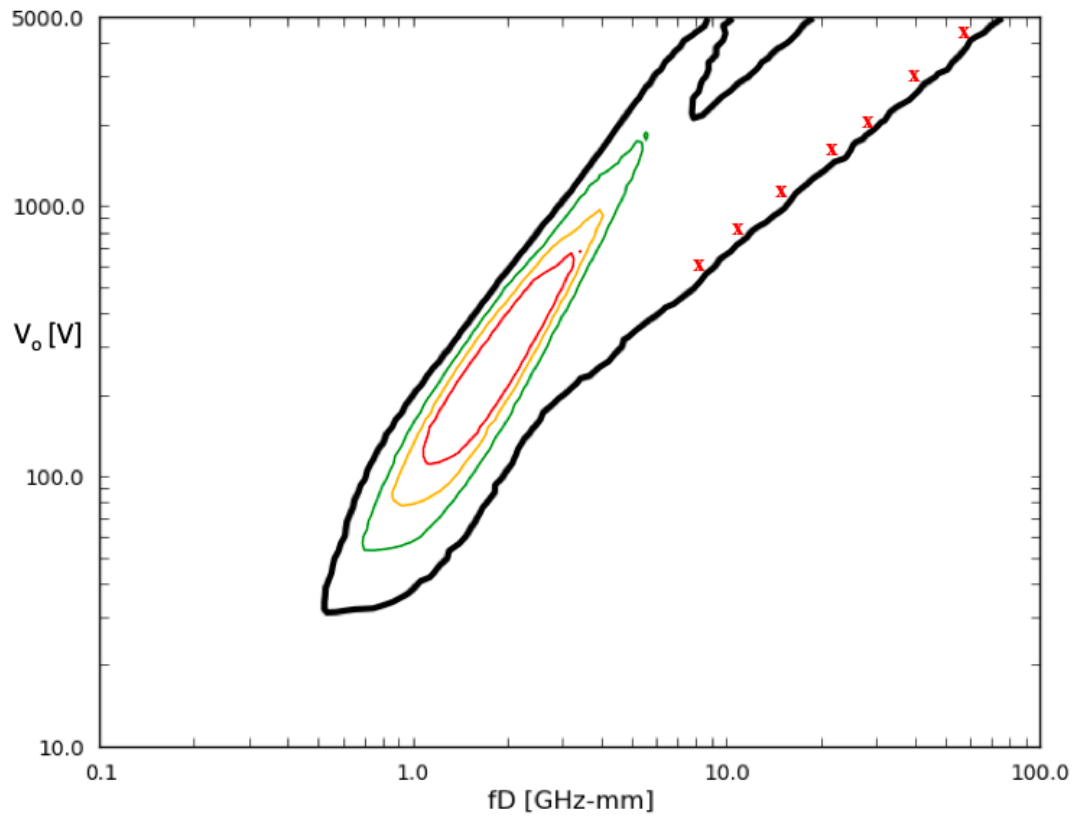


Figure 2.20: Multipactor susceptibility diagram (log-log plot) for copper material with  $B_{DC} = 10$  mT (corresponding to  $\Omega \approx 0.28$ ) constructed from the map-based theory. Here, the RF frequency is taken to be  $f = 1$  GHz. Contours corresponding to different magnitudes of  $\delta_{\text{eff}}$  are shown (according to the same color-code in Fig. 2.17).

susceptibility boundary. Simulations also predict multipactor growth in this expanded parameter space (indicated by the red crosses in Fig. 2.20). Although a DC magnetic-field is often examined for multipactor suppression, it can also result in higher SEE yields as the magnetic-field alters trajectories and causes impacts at oblique angles.

The susceptibility diagrams constructed from the map-based theory have several key advantages compared to current state-of-the-art industrial design standards. First, as the map-based theory makes no *a priori* resonance assumptions, these susceptibility diagrams incorporate the effects of all possible manifestations of multipactor. Second, single-surface impacts, which can play a considerable role in two-surface systems, are consistently included (recall that the map given by Eq. 2.7 selects the minimum of the two transit-times). Third, realistic spreads in secondary emission energies and angles are incorporated (see Eq. 2.13). Lastly, the map-based theory is universal in that the fields (or geometry) can be changed by simply modifying the underlying equations (as demonstrated in Sect's 2.2-2.4). All of these features allow for accurate and reliable multipactor threshold predictions.

## Chapter 3: Map-Based Multipactor Theory for Coaxial Systems

### 3.1 Chapter Overview

This chapter expands the map-based multipactor theory introduced in Ch. 2 to a coaxial geometry driven by the transverse electromagnetic (TEM) mode and an axial DC magnetic-field (Sect. 3.2). Here, the theoretical predictions are tested against published simulation and experimental results. The content from this chapter is published in Ref. [93].

### 3.2 Map-Based Multipactor Theory for a Coaxial System

#### 3.2.1 Basic Equations and Multipactor Maps

In this analysis, a coaxial geometry (inner-radius  $a$ , outer-radius  $b$ ) and a cylindrical coordinate system  $(r, \phi, z)$  are used (Fig. 3.1). Here, the length of the conductors  $L$  is assumed to be much greater than the conductor radii (i.e.,  $L \gg a, b$ ). The fundamental transverse electromagnetic (TEM) mode with an RF voltage amplitude  $V_0$  and an RF frequency  $\omega = 2\pi f$  is assumed, corresponding to a radial radio-frequency (RF) electric-field given by  $E_{RF}(r, t) = \frac{-V_0}{r(t)\ln(b/a)}\sin(\omega t + \theta_0)$ . As in Ch. 2, the sign of the RF electric field is negative in order to have positive acceleration for accelerating phases in  $[0, \pi)$ . Further, an axial DC magnetic-field is applied in the  $z$ -direction. This system is commonly examined for multipactor suppression schemes in

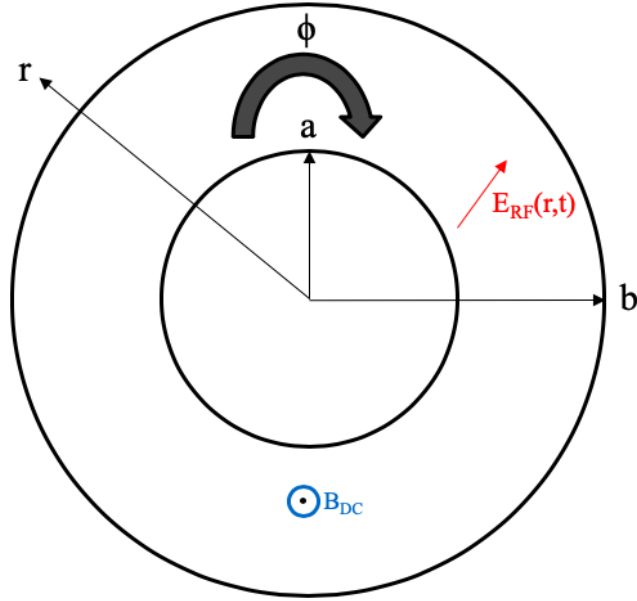


Figure 3.1: Cross-sectional view of a coaxial geometry with inner-radius  $a$  and outer-radius  $b$ . The cylindrical coordinate system  $(r, \phi, z)$  is shown, where the  $z$ -axis extends along the length of the conductors (i.e., into or out of the page). The radial RF electric-field and the axial DC magnetic-field are also shown.

space-borne applications [70-71]. The Lorentz force-law for this system is given by:

$$\ddot{r} - r(\dot{\phi})^2 = \frac{e}{m} \left( \frac{V_0}{r(t) \ln(b/a)} \sin(\omega t + \theta_0) - B_{DC} r \dot{\phi} \right), \quad (3.1)$$

$$r\ddot{\phi} + 2\dot{r}\dot{\phi} = \frac{e}{m} B_{DC} \dot{r}. \quad (3.2)$$

As this system conserves angular momentum,  $\dot{\phi}(t)$  can be eliminated and Eq.'s 3.1 and 3.2 can be reduced to a single second-order differential equation for  $r(t)$ . To demonstrate this, first note that the left-hand side of Eq. 3.2 can be rewritten as  $\frac{1}{r} \frac{d}{dt} (r^2 \dot{\phi})$ . Substituting this expression into the left-hand side of Eq. 3.2, multiplying

both sides by  $r$ , and then integrating (with respect to time) yields the following expression for  $\dot{\phi}$ :

$$\dot{\phi} = \frac{\frac{eB_{DC}}{2m}(r^2 - r_0^2) + \phi_0 r_0^2}{r^2}. \quad (3.3)$$

In Eq. 3.3,  $r_0 = r(t = 0)$  corresponds to an emission either from the inner-conductor (i.e.,  $r_0 = a$ ) or an emission from the outer-conductor (i.e.,  $r_0 = b$ ) while  $\phi_0 = \phi(t = 0)$ . Substituting Eq. 3.3 into Eq. 3.1 yields the following second-order differential equation:

$$\ddot{r} - \frac{\left(\frac{eB_{DC}}{2m}(r^2 - r_0^2) + \phi_0 r_0^2\right)^2}{r^3} = \frac{e}{m} \left( \frac{V_0}{r(t) \ln(b/a)} \sin(\omega t + \theta_0) - \frac{B_{DC} \left(\frac{eB_{DC}}{2m}(r^2 - r_0^2) + \phi_0 r_0^2\right)}{r} \right). \quad (3.4)$$

As shown, the original system of two second-order differential equations (Eq.'s 3.1 and 3.2) is reduced to a single second-order differential equation for  $r(t)$  (Eq. 3.4). In this chapter, the following normalized variables are used:  $\tau = \omega t$  for time,  $\bar{r} = (r-a)/(b-a)$  for the radial position (note that  $r = a \rightarrow \bar{r} = 0$  and  $r = b \rightarrow \bar{r} = 1$ ),  $\bar{v} = v/(\omega b)$  for velocity,  $\bar{E}_0 = eV_0/(mb^2\omega^2)$  for the RF electric-field amplitude,  $\Omega = \omega_c/\omega$  for the DC magnetic-field ( $\omega_c = eB_{DC}/m$  is the cyclotron frequency), and  $R = a/b$  (representing a geometry parameter).

Equation 3.4 can be equivalently expressed with these normalized variables by making the appropriate substitutions and converting the time derivatives to derivatives with respect to  $\tau$ , i.e.,  $\dot{r} = (1 - R)\omega b \bar{r}'$  and  $\dot{\phi} = \omega \phi'$ , where  $' = \frac{d}{d\tau}$ . For simplicity, the normalized form of Eq. 3.4 is not presented here (but can be obtained from the

procedure discussed above). Moreover, the radial and azimuthal velocities are  $v_r = \dot{r}$  and  $v_\phi = r\dot{\phi}$ , respectively (recall  $\dot{\phi}$  is given by Eq. 3.3). In normalized notation, these velocities are expressed as  $\bar{v}_r = (1-R)\bar{r}'$  and  $\bar{v}_\phi = (\bar{r}(1-R) + R)\phi'$ . The initial normalized radial and azimuthal emission velocities are denoted as  $\bar{v}_{r0}$  and  $\bar{v}_{\phi0}$ , respectively.

To construct the multipactor maps for given parameters  $(\bar{E}_0, \Omega, R, \bar{v}_{r0}, \bar{v}_{\phi0})$ , the normalized transit-times over all emissions phases  $\theta_0$  in  $[0, 2\pi)$  are computed:  $\tau_{aa}(\theta_0|\bar{E}_0, \Omega, R, \bar{v}_{r0}, \bar{v}_{\phi0})$ ,  $\tau_{ab}(\theta_0|\bar{E}_0, \Omega, R, \bar{v}_{r0}, \bar{v}_{\phi0})$ ,  $\tau_{bb}(\theta_0|\bar{E}_0, \Omega, R, \bar{v}_{r0}, \bar{v}_{\phi0})$  and  $\tau_{ba}(\theta_0|\bar{E}_0, \Omega, R, \bar{v}_{r0}, \bar{v}_{\phi0})$ . Here, the subscripts of  $\tau$  designate the emission conductor and the impact conductor, respectively, where ‘a’ refers to the inner-conductor and ‘b’ refers to the outer-conductor. As seen in Ch. 2, electrons may impact either conductor and thus all four transit-times are calculated to account for the possibility of both single-surface impacts ( $a \rightarrow a$  or  $b \rightarrow b$ ) and two-surface impacts ( $a \rightarrow b$  or  $b \rightarrow a$ ).

To calculate  $\tau_{aa}(\theta_0)$  and  $\tau_{ab}(\theta_0)$ , Eq. 3.4 (in normalized form) is first numerically solved via an ordinary differential equation (ODE) solver with the initial conditions  $\bar{r}_a(\tau = 0, \theta_0) = 0$  and  $\bar{r}'_a(\tau = 0, \theta_0) = \bar{v}_{r0}/(1-R)$ . Here, the subscript of  $\bar{r}$  indicates the emission conductor (i.e., ‘a’ for inner-conductor and ‘b’ for outer-conductor). An integrator based on linear multistep methods is selected, which gives similar results as a standard Runge-Kutta integrator but is more computationally efficient (for this study) [98]. The single-surface transit-time  $\tau_{aa}(\theta_0)$  and two-surface transit-time  $\tau_{ab}(\theta_0)$  are then obtained by solving  $\bar{r}_a(\tau_{aa}, \theta_0) = 0$  and  $\bar{r}_a(\tau_{ab}, \theta_0) = 1$ , respectively. As the trajectory may intersect zero (or unity) more than once, the earliest such solutions are used.

Similarly, to calculate  $\tau_{bb}(\theta_0)$  and  $\tau_{ba}(\theta_0)$ , Eq. 3.4 (in normalized form) is first numerically solved but now with the initial conditions  $\bar{r}_b(\tau = 0, \theta_0) = 1$  and

$\bar{r}'_b(\tau = 0, \theta_0) = -\bar{v}_{r0}/(1-R)$ . Note that the radial emission velocity is negative for an emission from the outer-conductor because the emission direction is in the negative radial direction (i.e., from the outer-conductor to the inner-conductor). The single-surface transit-time  $\tau_{bb}(\theta_0)$  and two-surface transit time  $\tau_{ba}(\theta_0)$  are then found by solving  $\bar{r}_b(\tau_{bb}, \theta_0) = 1$  and  $\bar{r}_b(\tau_{ba}, \theta_0) = 0$ , respectively. All numerical parameters relating to the integration of Eq. 3.4 are thoroughly tested.

The multipactor maps that relate an emission phase from each conductor to the phase at the next impact are given by:

$$M_a(\theta_0|\bar{E}_0, \Omega, R, \bar{v}_{r0}, \bar{v}_{\phi 0}) = (\theta_0 + \tau_{\min}^a(\theta_0)) \bmod 2\pi, \quad (3.5)$$

$$M_b(\theta_0|\bar{E}_0, \Omega, R, \bar{v}_{r0}, \bar{v}_{\phi 0}) = (\theta_0 + \tau_{\min}^b(\theta_0)) \bmod 2\pi. \quad (3.6)$$

In Eq.'s 3.5 and 3.6,  $\tau_{\min}^a(\theta_0) = \min(\tau_{aa}(\theta_0), \tau_{ab}(\theta_0))$  and  $\tau_{\min}^b(\theta_0) = \min(\tau_{bb}(\theta_0), \tau_{ba}(\theta_0))$  while the subscript of  $M$  (and the superscript of  $\tau_{\min}$ ) corresponds to the emission conductor (i.e.,  $M_a$  is the map for an emission from the inner-conductor and  $M_b$  is the map for an emission from the outer-conductor). Here, the transit-time dependence on the system parameters is implied (i.e.,  $\tau(\theta_0)$  is used rather than  $\tau(\theta_0|\bar{E}_0, \Omega, R, \bar{v}_{r0}, \bar{v}_{\phi 0})$  for convenience). As in Ch. 2, the minimum transit-time is selected to consistently account for both single-surface impacts ( $a \rightarrow a$  or  $b \rightarrow b$ ) and two-surface impacts ( $a \rightarrow b$  or  $b \rightarrow a$ ).

Note that, unlike the maps for a parallel-plate system (Eq. 2.7), impact phases resulting from two-surface transits are not shifted by  $\pi$ . This is because the coordinate system does not reverse direction after each two-surface impact and therefore the sign of the RF field need not be reversed for the subsequent iteration.

Given an emission phase  $\theta_0$  (and the emission conductor), the RF phase at all subsequent impacts can be tracked by repeatedly iterating Eq's 3.5 and 3.6. To illustrate

the procedure of advancing an electron in this system, consider an emission phase  $\theta_0$  from the inner-conductor. If the transit-time to impact the inner-conductor is shorter, i.e.,  $\tau_{aa}(\theta_0) < \tau_{ab}(\theta_0)$ , then the same map ( $M_a$ ) is used to further advance the system. However, if the transit-time to the outer-conductor is shorter, i.e.,  $\tau_{ab}(\theta_0) < \tau_{aa}(\theta_0)$ , then the subsequent emission phase ( $\theta_1 = M_a(\theta_0)$ ) is advanced by  $M_b$  on the next iteration ( $\theta_2 = M_b(\theta_1)$ ). Thus, on each two-surface impact, the map used to advance the system for the following iteration is switched. On each iteration, the impact conductor is recorded to ensure the proper map is used for the subsequent map advance. Recall that this map-advancement procedure is similar to that in a parallel-plate system with a normal DC electric-field, where a separate map for each surface is also required (see Sect. 2.3.1).

After a sufficient number of map iterations, orbits reach the attractor. As demonstrated in Ch. 2, the attractor form varies as a function of the system parameters, which is often displayed on a bifurcation diagram. In this analysis, rather than analyzing individual bifurcation diagrams (as done in Ch. 2), the attractor impact phases are directly used to predict multipactor growth or decay. This is justified as the main interest of this analysis is to compare against published results rather than to analyze specific multipactor dynamics. Bifurcation diagrams for this coaxial system can be constructed from an analogous procedure described in Ch. 2.

## 3.2.2 Comparison to Published Simulation and Experimental Results

In this section, the map-based theory for a coaxial system developed in Sect. 3.2.1 is tested against published simulations and experiments conducted at the European Space Agency Val Space Consortium Laboratory [70]. In this study, multipactor in a coaxial waveguide under TEM mode operation is investigated over a wide range of axial DC magnetic-field strengths. The experimental parameters include:  $a = 1.515$  mm,  $b = 3.490$  mm,  $f = \omega/2\pi = 1.145$  GHz, a DC magnetic-field test-range between 0 mT and 35 mT, and copper conductors ( $\delta_{\max 0} = 2.25$ ,  $W_{\max 0} = 175$  eV). For each DC magnetic-field strength, the multipactor threshold power (i.e., the minimum RF power that initiates multipactor) is determined. For further details on the experimental setup and methodology, the reader is referred to Ref. [70]. In addition to the experimental data, this study also provides simulation predictions from the FEST3D code [48]. This simulation code also uses a SEE model based on the modified Vaughan's formula (see Sect. 1.3.2). The multipactor threshold power as a function of the DC magnetic-field strength obtained from experiment and simulation are shown together in Fig. 2 of Ref. [70], which demonstrates that multipactor behaves nonlinearly with respect to the magnetic-field.

To test the map-based theory against these results, the effective SEE yield  $\delta_{\text{eff}}(\bar{E}_0, \Omega, R)$  (Eq. 2.13) is calculated as a function of  $\bar{E}_0$  for each DC magnetic-field strength. Recall that this requires constructing several maps (Eq's 3.5 and 3.6) for several monoenergetic emissions and fixed emission angles (i.e., different combinations of  $(\bar{v}_{r0}, \bar{v}_{\phi 0})$ ), computing the corresponding attractors and average SEE

yields (Eq. 2.10), and then integrating over specified secondary emission distributions. On each scan, the normalized variables in the theory ( $\Omega = \omega_c/\omega$  and  $R = a/b$ ) are set according to the experimental parameters. While  $\Omega$  changes with the DC magnetic-field strength,  $R \approx 0.434$  remains constant as the conductor radii are fixed. Further, the material parameters of the SEE model in the theory are set to correspond to copper (as in the experiment and simulation) while  $f_1(\bar{v}_0)$  and  $f_2(\phi)$  in Eq. 2.13 are set to a Maxwellian distribution (with an average value corresponding to an emission energy of 4 eV) and a cosine-law, respectively, to match the FEST3D simulation code.

Varying  $\bar{E}_0$  is equivalent to varying the RF power. The normalized threshold point  $\bar{E}_{0TH}$  is defined as the value where the effective SEE yield first intercepts unity (or equivalently where the exponential growth is zero), i.e.,  $\delta_{\text{eff}}(\bar{E}_0, \Omega, R) \approx 1.0$  (see Fig. 3.2 for an example). The threshold power is defined as  $P_{TH} = \frac{V_{0TH}^2}{2Z_0}$ , where the threshold RF voltage amplitude  $V_{0TH}$  is recovered from the normalization (i.e.,  $V_{0TH} = (m/e)(b\omega)^2\bar{E}_{0TH}$ ) and  $Z_0 = 50 \Omega$  is the characteristic impedance of the transmission line used in the experiments. Note that the factor of (1/2) is present in the expression for  $P_{TH}$  because the peak voltage is used as opposed to the RMS voltage. Finally, expressing  $V_{0TH}$  in terms of  $\bar{E}_{0TH}$  results in the following expression for the RF threshold power:

$$P_{TH} = \frac{\left(\frac{m}{e}\right)^2 (b\omega)^4 \bar{E}_{0TH}^2}{2Z_0}. \quad (3.7)$$

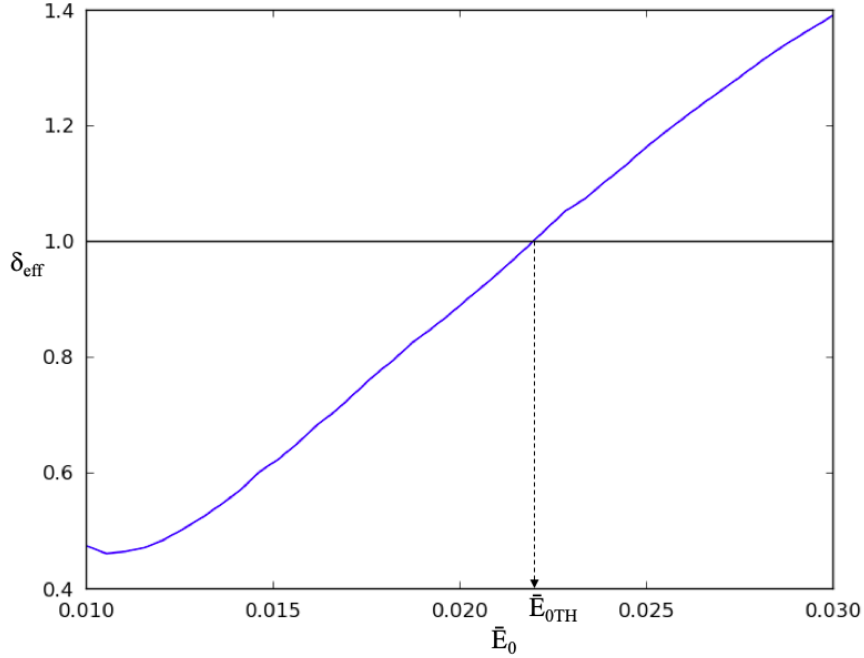


Figure 3.2: Effective SEE yield as a function of  $\bar{E}_0$  for fixed parameters  $\Omega = 0.856$  (corresponding to  $B_{\text{DC}} = 35$  mT and  $f = 1.145$  GHz) and  $R = 0.434$  (corresponding to  $a = 1.515$  mm and  $b = 3.490$  mm). The normalized threshold point  $\bar{E}_{0\text{TH}}$  is defined as the value where  $\delta_{\text{eff}} \approx 1.0$  (indicating the onset of multipactor).

Figure 3.3 plots the threshold power predicted by the map-based theory against the simulation and experimental results provided in Ref. [70]. The theoretical predictions are in excellent agreement with the simulations over the entire magnetic-field range and depict a similar nonlinear multipactor behavior. Note that the simulation code, which numerically tracks electron trajectories, is fundamentally different from the theory, which instead tracks phase advancement via the maps (Eq.'s 3.5 and 3.6). Discrepancies between theory with experiment (and simulation with experiment) are attributed to the assumed secondary emission energy and angle distributions, possible

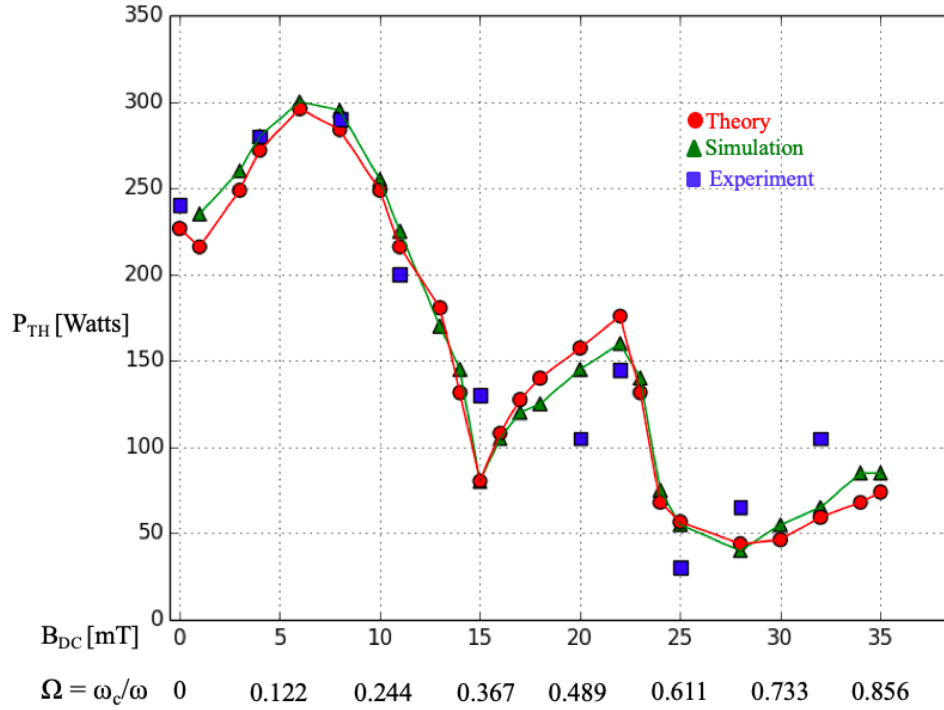


Figure 3.3: Multipactor threshold power predicted by the map-based theory (red circles) against simulation (green triangles) and experimental (blue squares) results from Ref. [70]. The value of the normalized parameter  $\Omega$  is shown for different DC magnetic-field strengths.

experimental errors, and inaccuracies in the SEE model.

Chapter 2 showed that the multipactor form changes throughout parameter space between single-resonance, period- $n$ , ping-pong, and chaos. Even more, it was found that these forms manifest in the exponential growth rate, where low-periodicity forms result in large growth rates compared to high-periodicity and chaotic modes. Although specific multipactor dynamics (i.e., bifurcation diagrams) are not presented in this analysis (for reasons discussed earlier), a similar explanation is expected to hold for the nonlinear structure of the threshold power in this coaxial system.

In fact, Fig. 3 of Ref. [70] shows representative electron trajectories for different DC magnetic-field strengths in this coaxial system. For weak DC magnetic-fields ( $B_{DC} \approx 0$  mT), electrons participate in two-surface resonance modes that involve transits from  $a \rightarrow b$  and  $b \rightarrow a$ . As the DC field becomes intermediate ( $B_{DC} \approx 10$  mT), ping-pong multipactor takes place, where combined single-surface and two-surface impacts occur. For even larger DC magnetic-fields, multipactor manifests as a single-surface resonance on the inner-conductor. This change in the multipactor mode throughout parameter space is well-in-line with the central message of the map-based theory and is further reflected in the threshold powers seen in theory, simulation, and experiment.

# Chapter 4: Map-Based Multipactor Theory for Multicarrier Operation

## 4.1 Chapter Overview

In this chapter, the map-based multipactor theory is generalized to multicarrier operation, where several RF carriers (each with a separate amplitude and frequency) are present. Here, the lowest-order multicarrier system in a parallel-plate geometry is considered, namely two-carrier operation (Sect 4.2). The theoretical predictions are verified against particle-in-cell simulations and an example of a two-carrier susceptibility diagram that summarizes the influence of the second-carrier on multipactor is presented. The content from this chapter is published in Ref. [94].

## 4.2 Map-Based Multipactor Theory for Two-Carrier Operation in a Parallel-Plate Geometry

### 4.2.1 Basic Equations and Multipactor Maps

To illustrate the map-based theory for a two-carrier system, consider parallel-plate geometry of gap separation  $D$  with RF electric-fields  $-E_{01}\sin(\omega_1 t + \theta_{01})$  and  $-E_{02}\sin(\omega_2 t + \theta_{02})$  (Fig. 4.1a). Here,  $E_{01}(E_{02})$ ,  $\omega_1 = 2\pi f_1(\omega_2 = 2\pi f_2)$ , and  $\theta_{01}(\theta_{02})$  are the amplitude, frequency, and initial phase, respectively, of the fundamental (second) RF carrier. The same normalized variables from Ch. 2 are also used in this chapter:  $\tau = \omega_1 t$

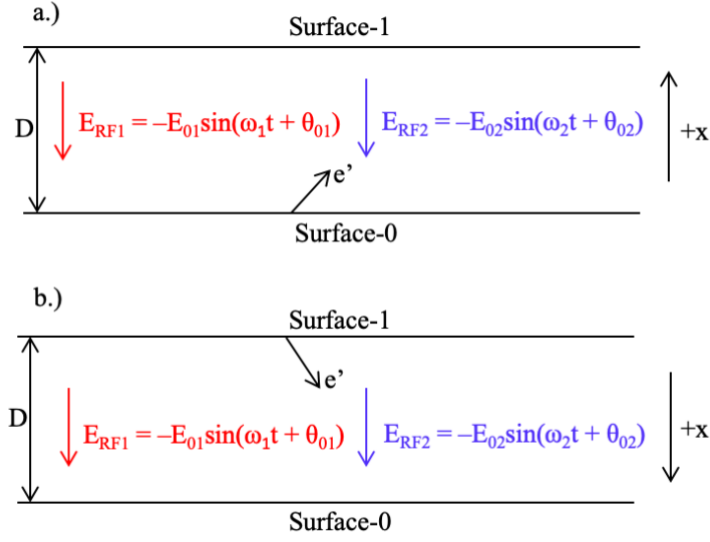


Figure 4.1: Parallel-plate geometry with gap separation  $D$  and fundamental-carrier ( $E_{RF1}$ ) and second-carrier ( $E_{RF2}$ ) RF electric-fields. Direction of coordinate system for an electron emitted from a.) surface-0 and b.) surface-1.

for time,  $\bar{x} = x/D$  for position,  $\bar{v} = v/(\omega_1 D)$  for velocity, and  $\bar{E}_{01} = eE_{01}/(mD\omega_1^2)$  for the fundamental carrier amplitude. Here, the parameters  $\beta = E_{02}/E_{01}$  (representing the ratio of the field amplitudes) and  $n = \omega_2/\omega_1$  (representing the ratio of the field frequencies) are also defined.

As in Ch. 2, the Lorentz force-law (Eq. 4.1) is integrated to obtain the velocity (Eq. 4.2) and position (Eq. 4.3) at a time  $\tau = \omega_1 t$  for an electron emitted at  $t = 0$  from surface-0 with a normal emission velocity  $v_{0x}$ :

$$\ddot{x} = (e/m)(E_{01}\sin(\omega_1 t + \theta_{01}) + E_{02}\sin(\omega_2 t + \theta_{02})), \quad (4.1)$$

$$\bar{v}(\tau, \theta_{01}, \theta_{02}) = -\bar{E}_{01}(\cos(\tau + \theta_{01}) - \cos(\theta_{01})) + (\beta/n)\cos(n\tau + \theta_{02}) - (\beta/n)\cos(\theta_{02}) + \bar{v}_{0x}, \quad (4.2)$$

$$\begin{aligned} \bar{x}(\tau, \theta_{01}, \theta_{02}) = & -\bar{E}_{01}(\sin(\tau + \theta_{01}) - \sin(\theta_{01}) - \tau \cos(\theta_{01}) + (\beta/n^2)\sin(n\tau + \theta_{02}) - \\ & (\beta/n^2)\sin(\theta_{02}) - \tau(\beta/n)\cos(\theta_{02})) + \tau \bar{v}_{0x}. \end{aligned} \quad (4.3)$$

Note that in the absence of the second-carrier (i.e.,  $\beta = 0$ ), Eq's 4.1-4.3 simplify to standard single-carrier operation, as given by Eq's 2.1-2.3. The normalized two-surface transit-time  $\tau_{01}$  and single-surface transit-time  $\tau_{00}$  for an emission from surface-0 are found by setting  $\bar{x}(\tau_{01}, \theta_{01}, \theta_{02}) = 1$  and  $\bar{x}(\tau_{00}, \theta_{01}, \theta_{02}) = 0$ , respectively:

$$\begin{aligned} 0 = & -\sin(\tau_{01} + \theta_{01}) + \sin(\theta_{01}) + \tau_{01}(\cos(\theta_{01}) + \bar{v}_{0x}/\bar{E}_{01}) - (\beta/n^2)\sin(n\tau_{01} + \theta_{02}) + \\ & (\beta/n^2)\sin(\theta_{02}) + (\beta/n)\tau_{01}\cos(\theta_{02}) - 1/\bar{E}_{01}, \end{aligned} \quad (4.4)$$

$$\begin{aligned} 0 = & -\sin(\tau_{00} + \theta_{01}) + \sin(\theta_{01}) + \tau_{00}(\cos(\theta_{01}) + \bar{v}_{0x}/\bar{E}_{01}) - (\beta/n^2)\sin(n\tau_{00} + \theta_{02}) + \\ & (\beta/n^2)\sin(\theta_{02}) + (\beta/n)\tau_{00}\cos(\theta_{02}). \end{aligned} \quad (4.5)$$

Recall that the subscripts of  $\tau$  designate the surface of emission and surface of impact, respectively. As before, both transit-times are calculated to account for impacts on either surface. As indicated by the normalization of time (i.e.,  $\tau = \omega_1 t$ ),  $\tau_{01}$  and  $\tau_{00}$  are defined with respect to the fundamental-carrier field. These quantities with respect to the second-carrier field are  $n\tau_{01}$  and  $n\tau_{00}$ . As before, no resonance assumptions on the transit-times are made to allow for the recovery of all possible modes.

For given system parameters ( $\bar{E}_{01}, \beta, n, \bar{v}_{0x}$ ), the maps relating an emission at  $\{\theta_{01}, \theta_{02}\}$  to the phases at the next impact are given by:

$$\begin{aligned} M_1(\theta_{01}, \theta_{02} | \bar{E}_{01}, \beta, n, \bar{v}_{0x}) = \\ \left\{ \begin{array}{l} \text{mod}(\theta_{01} + \tau_{00}(\theta_{01}, \theta_{02} | \bar{E}_{01}, \beta, n, \bar{v}_{0x}), 2\pi), \quad \tau_{\min} = \tau_{00}(\theta_{01}, \theta_{02} | \bar{E}_{01}, \beta, n, \bar{v}_{0x}) \\ \text{mod}(\theta_{01} + \tau_{01}(\theta_{01}, \theta_{02} | \bar{E}_{01}, \beta, n, \bar{v}_{0x}) + \pi, 2\pi), \quad \tau_{\min} = \tau_{01}(\theta_{01}, \theta_{02} | \bar{E}_{01}, \beta, n, \bar{v}_{0x}) \end{array} \right\}, \end{aligned} \quad (4.6)$$

$M_2(\theta_{01}, \theta_{02} | \bar{E}_{01}, \beta, n, \bar{v}_{0x}) =$

$$\begin{cases} \text{mod}(\theta_{02} + n\tau_{00}(\theta_{01}, \theta_{02} | \bar{E}_{01}, \beta, n, \bar{v}_{0x}), 2\pi), & \tau_{\min} = \tau_{00}(\theta_{01}, \theta_{02} | \bar{E}_{01}, \beta, n, \bar{v}_{0x}) \\ \text{mod}(\theta_{02} + n\tau_{01}(\theta_{01}, \theta_{02} | \bar{E}_{01}, \beta, n, \bar{v}_{0x}) + \pi, 2\pi), & \tau_{\min} = \tau_{01}(\theta_{01}, \theta_{02} | \bar{E}_{01}, \beta, n, \bar{v}_{0x}) \end{cases} \quad (4.7)$$

In Eq's 4.6 and 4.7,  $\tau_{01}(\theta_{01}, \theta_{02} | \bar{E}_{01}, \beta, n, \bar{v}_{0x})$  and  $\tau_{00}(\theta_{01}, \theta_{02} | \bar{E}_{01}, \beta, n, \bar{v}_{0x})$  are the normalized two-surface and single-surface transit-times for an emission at  $\{\theta_{01}, \theta_{02}\}$  as determined by the earliest nonnegative roots of Eq's 4.4 and 4.5, respectively, while  $\tau_{\min}$  is the minimum of the two transit-times (Eq. 2.6). Each RF carrier has a separate map, where  $M_1$  (Eq. 4.6) corresponds to the map for the fundamental-carrier and  $M_2$  (Eq. 4.7) corresponds to the map for the second-carrier. As two RF phases are tracked, the maps are two-dimensional. In general, a  $k$ -carrier system is described by  $k$  separate maps that are each  $k$ -dimensional.

As in maps for single-carrier operation (Eq. 2.7), impact phases resulting from two-surface transits are shifted by  $\pi$  to account for the change in sign of the RF fields under the flipped coordinate system for the subsequent iteration (see Fig. 4.1b). As the transit-times are symmetric, i.e.,  $\tau_{01} = \tau_{10}$  and  $\tau_{00} = \tau_{11}$ , Eq.'s 4.6 and 4.7 can guide emissions from either surface. This symmetry is broken if a normal DC electric-field is present in the gap or if the geometry is coaxial, as shown in Sect. 2.3 and Ch. 3, respectively.

The RF phases at the next impact for an emission at  $\{\theta_{01}^0, \theta_{02}^0\}$  can be determined by iterating Eq's 4.6 and 4.7, i.e.,  $\theta_{01}^1 = M_1(\theta_{01}^0, \theta_{02}^0)$  and  $\theta_{02}^1 = M_2(\theta_{01}^0, \theta_{02}^0)$ . In this notation, the superscript of  $\theta$  refers to the iteration number while, as before, the subscript refers to the RF carrier. A second iteration results again

in the next pair of impact phases, i.e.,  $\theta_{01}^2 = M_1(\theta_{01}^1, \theta_{02}^1)$  and  $\theta_{02}^2 = M_2(\theta_{01}^1, \theta_{02}^1)$ . As described in Ch. 2, the attractor is reached by systematically repeating this process for a random sample of emissions. Note that, as two RF phases are tracked, the attractor is two-dimensional.

As demonstrated in Ch. 2, the attractor varies as a function of the system parameters ( $\bar{E}_{01}$ ,  $\beta$ ,  $n$ ,  $\bar{v}_{0x}$ ) and is often displayed on a bifurcation diagram. As the attractor is two-dimensional for two-carrier systems, the corresponding bifurcation diagrams are 3D (i.e., each RF carrier phase and the varying system parameter). As 3D plots are difficult to visualize, bifurcation diagrams are not as conceptually useful for two-carrier systems (or multicarrier systems) as for single-carrier systems. Thus, the attractor impact phases are not presented on bifurcation diagrams in this study but are rather directly used to compute multipactor growth (or decay). This is further justified as the primary interest of this analysis is to test the predictivity of the map-based theory rather than to analyze specific multipactor dynamics. The procedure of calculating the attractor for a two-carrier system is analogous to that in a single-carrier system.

## 4.2.2 Comparison to Simulation and Two-Carrier Susceptibility Diagrams

To test the map-based theory for two-carrier operation, a simulation scan is conducted using the Warp code. As in Ch. 2, a fundamental-carrier amplitude  $E_{01} = 91.75$  kV/m and frequency  $f_1 = \omega_1/2\pi = 500$  MHz along with a gap separation of  $D = 7$  mm are selected (assuming copper material). Here, a second-carrier RF electric-field is also included in the Warp model. The second-carrier frequency is set to a fixed

value of  $f_2 = \omega_2/2\pi = 250$  MHz (corresponding to  $n = 0.50$ ). For these fixed values, a series of simulations are run, each with a different second-carrier RF amplitude  $E_{02}$ . The second-carrier amplitudes are chosen so that the parameter  $\beta = E_{02}/E_{01}$  ranges from 0.0-2.0, resulting in a range between 0 kV/m and 183.5 kV/m. The simulation procedure is identical to that in Ch. 2 and the multipactor exponential growth rate (over a fundamental RF period) is computed in a similar way.

To compare the Warp simulations to the theoretical model, the effective SEE yield  $\delta_{\text{eff}}(\bar{E}_{01}, \beta, n)$  (Eq. 2.12) is calculated as a function of  $\beta$ . Recall that this requires constructing several maps (each with a different monoenergetic  $\bar{v}_{0x}$ ), computing the corresponding attractors, average SEE yields (Eq. 2.10), and then integrating over an emission velocity distribution (Eq. 2.11). For each scan, the other system parameters are set to correspond to the simulation parameters, resulting in a constant  $\bar{E}_{01} \approx 0.23358$  and  $n = 0.50$ . The maps (Eq's 4.6 and 4.7) on each emission energy scan are constructed from the Newton-Raphson root-finding algorithm described in Sect. 2.2.1.

Figure 4.2 plots the effective SEE yield predicted by Warp and the map-based theory with an emission energy scan using a  $\bar{v}_{0x\text{avg}}$  corresponding to a normal emission energy of  $W_{0x\text{avg}} = 3$  eV (i.e., a total average emission energy of 6 eV as  $\bar{v}_y = \bar{v}_{0x} \rightarrow W_{0\text{avgtotal}} = 2W_{0x\text{avg}}$ ). Both curves from theory and simulation track closely throughout the entire scan. The crossover point, i.e., where the effective SEE yield intercepts unity (or equivalently where the exponential growth rate is zero), predicted by Warp and the theory is in close agreement. As seen from the scans, the effective SEE yield decreases as the strength of the second-carrier field increases. Chapter 2 demonstrated that the system attractor form manifests in the exponential growth rate, where low-periodicity

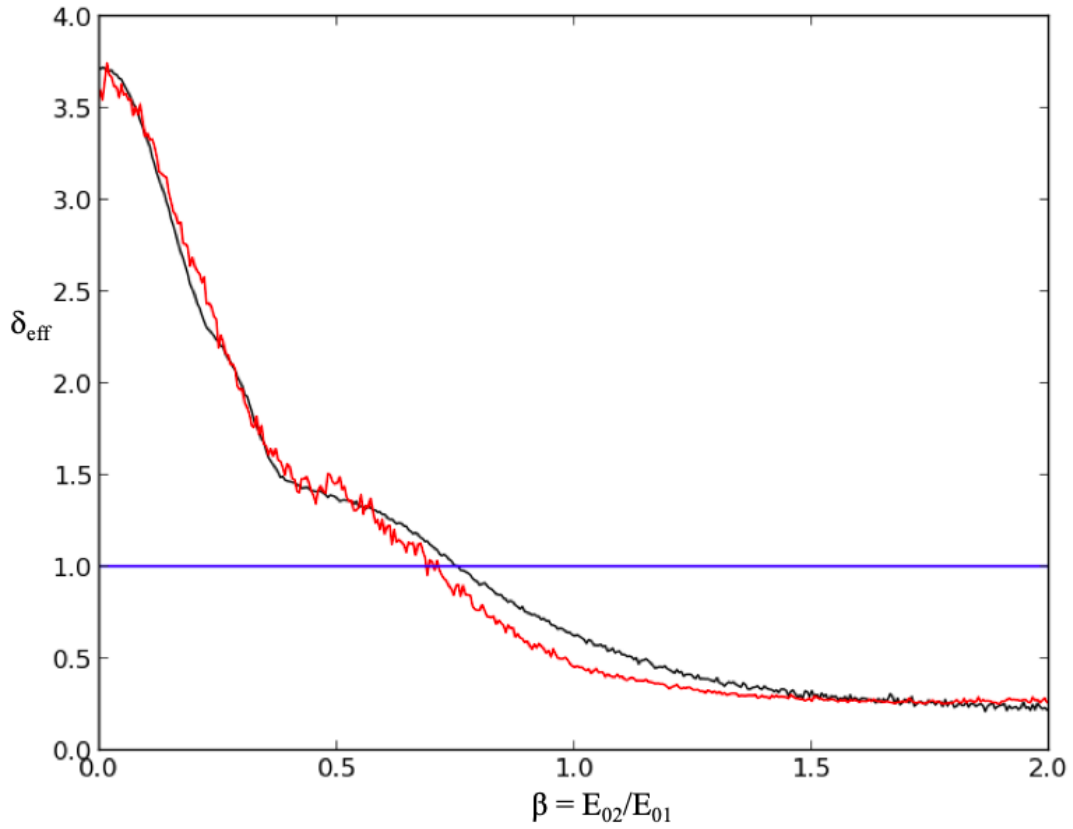


Figure 4.2: Effective SEE yield over a fundamental RF period from theory with an emission energy scan (red) and Warp simulations (black) as a function of  $\beta$ . The fundamental RF field amplitude and frequency are  $E_{01} = 91.75$  kV/m and  $f_1 = 500$  MHz, respectively, while the gap separation is  $D = 7$  mm (corresponding to  $\bar{E}_{01} \approx 0.23358$ ). The RF frequency of the second-carrier is  $f_2 = 250$  MHz (corresponding to  $n = 0.50$ ). The corresponding second-carrier field amplitude scan range is from 0 kV/m to 183.5 kV/m.

forms result in large growth rates compared to high-periodicity and chaotic modes. Although bifurcation diagrams are not presented in this analysis (for reasons discussed earlier), a similar explanation is expected to also apply for two-carrier systems.

The scan in Fig. 4.2 is done for a fixed second-carrier frequency (i.e., a fixed  $n$ ). Figure 4.3 shows a two-carrier susceptibility diagram, where  $\beta$  and  $n$  are both simultaneously varied for the same fixed values of  $E_{01}$ ,  $\omega_1$ , and  $D$  selected before (corresponding to  $\bar{E}_{01} \approx 0.23358$ ). This diagram is constructed as follows. For each  $(\beta, n)$  coordinate on the diagram (and the fixed  $\bar{E}_{01}$ ), the effective SEE yield (Eq. 2.12) is computed. The diagram is then color-coded according to the magnitude of the effective SEE yield (color-code shown on right of Fig. 4.3).

Figure 4.3 can be understood as follows. For  $\beta \approx 0$ , the second-carrier strength is too weak to significantly affect the large multipactor growth rate. As  $\beta$  increases, the growth rate begins to change as the second-carrier field becomes sufficiently strong to influence the multipactor electrons. Additionally, for a sufficiently large  $\beta$ , the growth rate also varies as a function of the second-carrier frequency (i.e.,  $n$ ). From the diagram, it is clear (for this particular choice of  $E_{01}$ ,  $\omega_1$ , and  $D$ ) that multipactor growth is minimum in the presence of a large second-carrier amplitude ( $\beta$ ) and a low second-carrier frequency ( $n$ ). Overall, the second-carrier field alters the electron trajectories, transit-times, impact energies, and angles (and hence the multipactor modes and SEE yields), in return modifying the growth rate. Such a diagram is a useful tool for device design as it identifies second-carrier parameters that mitigate multipactor growth or even result in multipactor-free operation. Note that a two-carrier susceptibility diagram can be constructed for any combination of  $E_{01}$ ,  $\omega_1$ , and  $D$ .

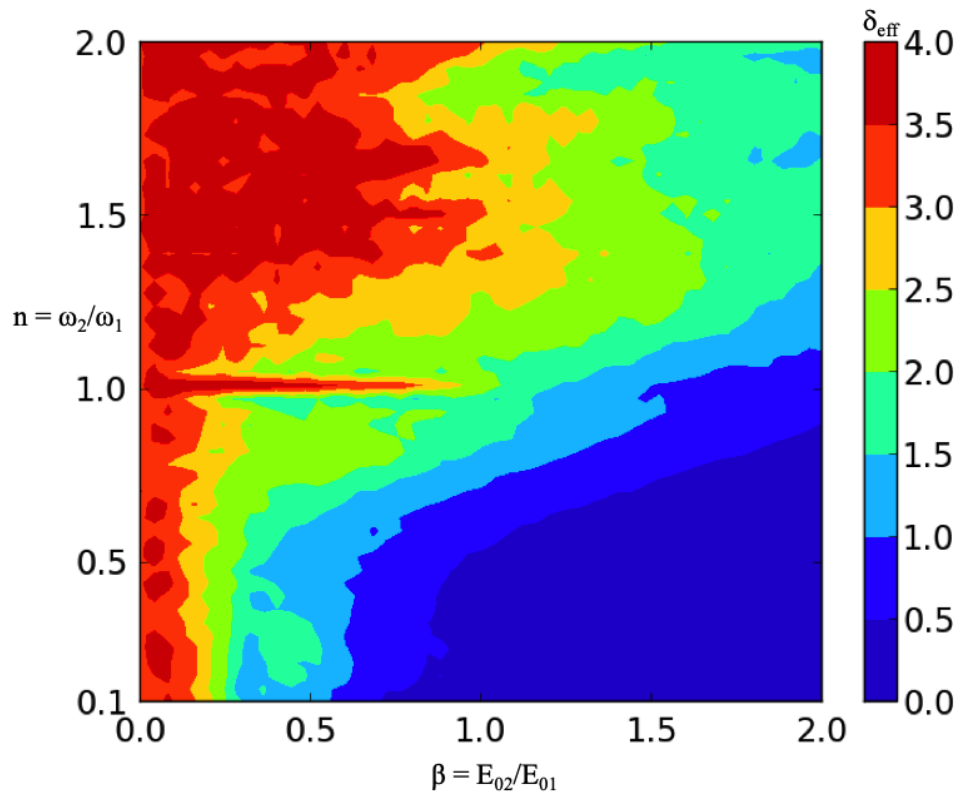


Figure 4.3: Two-carrier susceptibility diagram for  $E_{01} = 91.75$  kV/m,  $f_1 = 500$  MHz, and  $D = 7$  mm (corresponding to  $\bar{E}_{01} \approx 0.23358$ ). The diagram is color-coded according to the magnitude of the effective SEE yield (color-code shown on right).

# Chapter 5: Summary and Future Research Directions

## 5.1 Chapter Overview

This chapter summarizes the major conclusions drawn from this dissertation research and the major features (and advantages) of the new theoretical approach (Sect. 5.2). Future research directions are then discussed (Sect. 5.3).

## 5.2 Summary

This dissertation presented a new theoretical approach based on nonlinear dynamics and chaos theory for the understanding, prediction, and assessment of multipactor discharge. The major findings from this research are as follows:

1. Multipactor is pervasive: it exists throughout dynamical space but changes form between single-resonance, period- $n$ , ping-pong, and chaos (see Fig. 2.3 for example). Even more, the multipactor form manifests in the exponential growth rate, where low-periodicity forms result in larger growth rates compared to high-periodicity and chaotic modes (see Fig. 2.10 for example). The transition to different forms of multipactor is immaterial.
2. The map-based theory recovers multipactor resonance under appropriate limits but also provides information on alternate parameter regions, where multipactor manifests in more complex forms (see Fig. 2.5 for example).

3. This new theory demonstrates that multipactor persists outside conventional resonance boundaries. In Sect. 2.5, the normalized theory was expressed in terms of susceptibility diagrams that portray multipactor breakdown boundaries as a function of device parameters. Compared to industrial design standards, these diagrams identify new parameter spaces susceptible to the discharge (see Fig. 2.18). These findings are supported by particle-in-cell simulations (see Fig. 2.19). In these new regions, multipactor manifests in more complex forms, such as ping-pong multipactor. The plethora of possible manifestations of multipactor, along with realistic spreads in secondary emission energies and angles, may shed light on experimental discrepancies with modern-day design standards.
4. The map-based scans suggest that the multipactor growth rate can be reduced by appropriately adjusting the device operation point to a region that supports chaos. This is a practical result and can be potentially used to design multipactor suppression schemes.
5. The map-based theory has been illustrated and verified for systems far more complex than standard single-carrier operation in a parallel-plate geometry (such as coaxial (Ch. 3) and multicarrier (Ch. 4)), demonstrating the accuracy of the theoretical model and its versatility as a predictive tool. This approach is well-suited to analyze these complex systems as it makes no *a priori* assumptions on the multipactor mode and rapidly scans vast regions of parameter space (along with a realistic spread in secondary emission energies and angles). This model serves as the first comprehensive theory

for multipactor discharge in coaxial and multicarrier systems.

6. Overall, the map-based theory revolutionizes the universal understanding of multipactor dynamics. It identifies stability boundaries and parameter regions susceptible to multipactor breakdown more reliably and comprehensively than existing models. This model serves as the first comprehensive theoretical solution for multipactor discharge.

Furthermore, the main features and advantages of the map-based multipactor theory are summarized as follows:

1. The theory is general in that it makes no *a priori* resonance assumptions on the multipactor mode. Instead, it models multipactor as a complex dynamical system, where iterative maps recover global multipactor behavior.
2. The theory is comprehensive as it rapidly scans vast regions of parameter space to recover a plethora of multipactor modes. This methodology readily incorporates a spread in secondary emission energies and angles, resulting in high-accuracy predictions.
3. The theory is predictive as the findings are in excellent agreement with resonance theory, particle-in-cell simulations, industrial design standards, and experimental data for a wide range of systems, including parallel-plate, coaxial, and multicarrier.

4. Compared to particle-tracking codes, this theoretical approach is far more computationally efficient, as it does not numerically track individual electron trajectories.
5. The theory is universal in that the same core procedure can be used to study different systems by simply changing the underlying equations (as demonstrated in Ch.'s [2-4](#)).

### 5.3 Future Research Directions

As with any mathematical model, there is always room for improvement. In this work, the theoretical predictions are only as accurate as the SEE emission model. Thus, future work includes incorporating more accurate SEE models and secondary emission distributions into the theory (as they are uncovered). Additionally, as Ch. [4](#) expanded the theoretical model to a two-carrier system, future work may also include incorporating multiple RF carriers into the theory. However, the main challenge in doing so is the computational cost required to construct the high-dimensional maps.

Moreover, the computer programming for the theoretical approach is implemented in Python. To enhance the computational efficiency, future work may also include implementing the programming in a lower level language, such as C. Finally, the ultimate test of this theory is experiment. Thus, future work includes designing and conducting experiments to further test the theoretical predictions. In particular, the major finding of multipactor suppression with chaos along with the susceptibility diagrams constructed in Sect. [2.5](#) provide a strong theoretical baseline for designing future experiments.

## Appendix A: Brief Review of Chaos Theory

As the theoretical approach presented in this dissertation is based upon chaos theory, this appendix provides a brief overview of this subject. This discussion is not intended to be an exhaustive overview but rather a brief discussion of the relevant concepts and terminology that pertain to this thesis. The reader is referred to Ref. [95] for a thorough introduction to chaos theory.

Chaos was perhaps first observed in the year 1880 by Henri Poincaré during his study of the three-body problem. In a general sense, chaos can be understood as unpredictable behavior. Chaos in dynamical systems is often associated with a sensitivity to initial conditions, where a small perturbation to an initial state results in an orbit that diverges exponentially from the initial orbit. Here, a dynamical system is defined as a system which evolves with respect to one or several variables (often time). A plethora of dynamical systems from a wide range of fields, such as physics, engineering, biology, economics, and meteorology, exhibit chaotic behavior. Today, chaos theory continues to be an active area of research.

A dynamical system is often characterized by a map  $M(x)$ , which is a mathematical function that describes the evolution of all possible states of the system (denoted by the variable  $x$ ). As this thesis deals mostly with one-dimensional discrete-time maps, this discussion is restricted to this particular type of system. Given an initial state  $x_0$ , the states at all subsequent times can be obtained by repeatedly iterating the

map, i.e.,  $x_1 = M(x_0)$ ,  $x_2 = M(x_1) \dots x_N = M(x_{N-1})$ . Here, each map application is called an iteration while the sequence of iterates  $\{x_0, x_1, x_2 \dots x_N\}$  is called the orbit.

After a sufficient number of map iterations, the dynamics cease to change and orbits converge to the attractor, which is defined as the set states that random orbits converge towards. Each attractor has an associated basin of attraction, which is defined as the set of states that converge to that attractor. Generally, there are three types of attractors for one-dimensional systems: fixed-point, limit cycle, and chaos.

A fixed-point of a map  $M$  is defined as a state that iterates back to itself, i.e., if  $x_0 = M(x_0)$ , then  $x_0$  is a fixed-point. Graphically, fixed-points are identified by intersections of the map with the  $45^\circ$  line of unity slope. A fixed-point is stable if random orbits converge towards it and unstable if random orbits diverge from it. Mathematically, a stable fixed-point  $x_s$  satisfies  $|dM(x_s)/dx| < 1$  while an unstable fixed-point  $x_{us}$  satisfies  $|dM(x_{us})/dx| > 1$ .

A limit-cycle (period- $n$ ) attractor contains  $n$  distinct states with the property that each state repeats periodically after  $n$  map iterations. Note that the special case of  $n = 1$  corresponds to a fixed-point attractor. The notion of stability for a limit-cycle attractor is similar to that of a fixed-point attractor in that the orbit is stable if random states are attracted towards it.

A chaotic attractor features no observable periodicity or pattern but rather consists of a random collection of states. Here, orbits do not get entrapped by a limit-cycle but instead visit random states on each map iteration, resulting in an attractor that spans a large number of states with no periodicity. This aperiodic behavior is typically referred to as chaos.

It is often the case that the map of a dynamical system is not only a function of the state space but also of system parameters. Thus, as a system parameter changes, so does the attractor. In chaos theory, the attractor dynamics as a function of a system parameter is often displayed on a bifurcation diagram. A bifurcation diagram is constructed by first fixing the parameter of interest to a particular value, then repeatedly advancing a random sample of states through the corresponding map, discarding the early iterations so as to eliminate the transient dynamics, and then selecting each unique remaining state, which constitutes the system attractor. The parameter is then incremented and this process is repeated. Thus, a bifurcation diagram is a visual representation of the system dynamics as a function of a system parameter. On a typical bifurcation diagram, the attractor changes form between fixed-point, limit-cycles, and chaos. The transition from a period- $n$  attractor to a period- $2n$  attractor is referred to as a period doubling bifurcation. At the transition points between different attractor forms, the preceding attractor form becomes unstable while the new attractor form gains stability.

Finally, as this thesis deals with multipactor dynamics, it is useful to discuss these concepts in the context of the multipactor phase maps (Eq. 2.7). A (stable) two-surface fixed-point attractor with a two-surface transit-time  $\tau_{01} = N\pi$  implies an order  $N$  resonance, as each impact occurs at half-integer multiples of the RF cycle (recall  $N$  is an odd integer representing the number of RF half-periods between impacts). Similarly, a (stable) single-surface fixed-point attractor with a single-surface transit-time  $\tau_{00} = M\pi$  implies an order  $M$  resonance, as each impact occurs at full-integer multiples of the RF cycle (recall  $M$  is an even integer representing the number of full RF periods between impacts). A period- $n$  attractor corresponds to a period- $n$  mode, as

the impact phase changes periodically between several values. A period- $n$  cycle can be either a resonant or non-resonant mode, where the general condition for two-surface resonance is given by  $\sum_{i=1}^n \tau_i = N\pi$  (or  $M\pi$  for single-surface resonance) [59]. In particular, a period- $n$  attractor that contains impact phases resulting from both two-surface and single-surface transits is a ping-pong mode (which can also be resonant according to a modified condition stated in Ref.'s [60-61]). Finally, a chaotic attractor corresponds to nonresonant multipactor, as impacts occur over a large spread of RF phases with no periodicity.

As shown in this thesis, the bifurcation diagrams depict the many possible manifestations of multipactor throughout parameter space. Recall that orbits guided by the phase map converge to stable attractor point(s) and are repelled from unstable points. Thus, with a sufficient sample of emission phases, the bifurcation diagrams recover all stable modes of the multipactor discharge over the entire parameter range. This methodology is far more comprehensive than the standard approach of applying stability conditions and deriving multipactor boundaries for different known modes (such as resonance) [1, 15-16].

## Bibliography

- [1] J.R.M. Vaughan. Multipactor. *IEEE Transactions on Electron Devices*, 35(7): 1172-1180, 1988.
- [2] D.H. Preist and R.C. Talcott. On the Heating of Output Windows of Microwave Tubes by Electron Bombardment. *IRE Transactions on Electron Devices*, 8:243-251, 1961.
- [3] J.R.M. Vaughan. Some High-Power Window Failures. *IRE Transactions on Electron Devices*, 8:302-308, 1961.
- [4] J.R.M. Vaughan. Observation of Multipactor in Magnetrons. *IEEE Transactions on Electron Devices*, 15(11):883-889, 1968.
- [5] G. Rumolo and F. Zimmermann. Electron cloud simulations: beam instabilities and wakefields. *Physical Review Special Topics – Accelerators and Beams*, 5(12):121002, 2002.
- [6] J.G. Power, W. Gai, S.H. Gold, A.K. Kinkead, R. Konecny, C. Jing, W. Liu, and Z. Yusof. Observation of Multipactor in an Alumina-Based Dielectric-Loaded Accelerating Structure. *Physical Review Letters*, 92(16):164801, 2004.
- [7] R. H. Cohen, A. Friedman, M. Kireeff Covo, S.M. Lund, A.W. Molvik, F.M. Bieniosek, P.A. Seidl, J.L. Vay, P. Stoltz, and S. Veitzer. Simulating electron clouds in heavy-ion accelerators. *Physics of Plasmas*, 12(056708), 2005.
- [8] L.Wu and L.K. Ang. Multipactor discharge in a dielectric-loaded accelerating structure. *Physics of Plasmas*, 14(013105), 2007.
- [9] O.V. Sinitsyn, G.S. Nusinovich, and T. M. Antonsen. Self-consistent nonstationary two-dimensional model of multipactor in dielectric-loaded accelerator structures. *Physics of Plasmas*, 16(073102), 2009.
- [10] A.D. Woode and J. Petit. Design data for the control of multipactor discharge in spacecraft microwave and RF systems. *Microwave Journal*, 35(142), 1992.
- [11] N. Rozario, H.F. Lenzing, K.F. Reardon, M.S. Zarro, and C.G. Baran. Investigation of Telstar 4 Spacecraft Ku-Band and C-Band Antenna Components for Multipactor Breakdown. *IEEE Transactions on Microwave Theory and Techniques*, 42(4):558-564, 1994.

- [12] A. Hubble, V. Chaplin, K. Clements, R. Spektor, P. Patridge, and T.P. Graves. Multipactor Breakdown Threshold Reduction Due to Magnetic Confinement in Parallel Fields. *IEEE Transactions on Plasma Science*, 45(7):1726-1730, 2017.
- [13] W.J. Gallagher. The multipactor electron gun. In *Proceedings of the IEEE*, 57(1): 94-95, 1969.
- [14] K. Mishra, D. Rathi, S. George, A. Varia, M. Parihar, H.M. Jada, Y.S.S. Srinivas, R. Singh, S. Kumar and S.V. Kulkarni. Conditioning technique for high power RF vacuum transmission line components using multipactor plasma. *Journal of Physics: Conference Series*, 208 (012017), 2010.
- [15] A.J. Hatch and H.B. Williams. The Secondary Electron Resonance Mechanism of Low-Pressure High-Frequency Gas Breakdown. *Journal of Applied Physics*, 25(4):417-423, 1954.
- [16] A.J. Hatch and H.B. Williams. Multipacting Modes of High-Frequency Gaseous Breakdown. *The Physical Review*, 112(3):681-685, 1958.
- [17] Hughes Aircraft Company. The Study of Multipactor Breakdown in Space Electronic Systems. *NASA Contractor Report*, 1966.
- [18] European Space Agency. Space Engineering, Multipaction Design, and Test. *ECSS-E-20-01A*, 2003; Revised 2013.
- [19] T.P. Graves. Standard/Handbook for Multipactor Breakdown Prevention in Spacecraft Components. *Aerospace Report No. TOR-2014-02198*, 2014.
- [20] American Institute of Aeronautics and Astronautics. Standard/Handbook for Radio-Frequency (RF) Breakdown Prevention in Spacecraft Components. *BSR/ANSI/AIAA S-142-201X*, 2016.
- [21] R.A. Kishek and Y.Y. Lau. Multipactor Discharge on a Dielectric. *Physical Review Letters*, 80(1):193-196, 1998.
- [22] L.K. Ang, Y.Y. Lau, R.A. Kishek, and R.M. Gilgenbach. Power Deposited on a Dielectric by Multipactor. *IEEE Transactions on Plasma Science*, 26(3):290-295, 1998.
- [23] A. Valfells, L.K. Ang, Y.Y. Lau, and R.M. Gilgenbach. Effects of external magnetic field and of oblique radio-frequency electric fields on multipactor discharge on a dielectric. *Physics of Plasmas*, 7(2): 750-757, 2000.
- [24] H.C. Kim and J.P. Verboncoeur. Time-dependent physics of a single-surface multipactor discharge. *Physics of Plasmas*, 12(123504), 2005.

- [25] P. Zhang, Y.Y. Lau, M. Franzi, and R.M. Gilgenbach. Multipactor susceptibility on a dielectric with a bias dc electric field and a background gas. *Physics of Plasmas*, 18(053508), 2011.
- [26] A. Iqbal, J. Verboncoeur, and P. Zhang. Multipactor susceptibility on a dielectric with two carrier frequencies. *Physics of Plasmas*, 25(043501), 2018.
- [27] N.K. Vdovicheva, A.G. Sazontov, and V.E. Semenov. Statistical Theory of Two-Sided Multipactor. *Radiophysics and Quantum Electronics*, 47(8):580-596, 2004.
- [28] A. Sazontov, V. Semenov, M. Buyanova, N. Vdovicheva, D. Anderson, M. Lisak, J. Puech, and L. Lapierre. Multipactor discharge on a dielectric surface: Statistical theory and simulation results. *Physics of Plasmas*, 12(093501), 2005.
- [29] A. Sazontov, M. Buyanova, V. Semenov, E. Rakova, N. Vdovicheva, D. Anderson, M. Lisak, J. Puech, and L. Lapierre. Effect of emission velocity spread of secondary electrons in two-sided multipactor. *Physics of Plasmas*, 12(053102), 2005.
- [30] S. Anza, C. Vicente, J. Gil, V.E. Boria, B. Gimeno, and D. Raboso. Nonstationary statistical theory for multipactor. *Physics of Plasmas*, 17(062110), 2010.
- [31] J. Rasch and J.F. Johansson. Non-resonant multipactor – A statistical model. *Physics of Plasmas*, 19(123505), 2012.
- [32] S. Lin, H. Wang, Y.Li, C. Liu, N. Zhang, W. Cui, and A. Neuber. Multipactor threshold calculation of coaxial transmission lines in microwave applications with nonstationary statistical theory. *Physics of Plasmas*, 22(082114), 2015.
- [33] S. Lin, R. Wang, N. Xia, Y. Li, and C. Liu. Stationary statistical theory of two-surface multipactor regarding all impacts for efficient threshold analysis. *Physics of Plasmas*, 25(013536), 2018.
- [34] V. Shemelin. Existence zones for multipactor discharges. *Soviet Physics Technical Physics*, 31(1029), 1986.
- [35] S. Riyopoulos. Multipactor saturation due to space-charge-induced debunching. *Physics of Plasmas*, 4(1448), 1997.
- [36] A. Valfells, J.P. Verboncoeur, and Y.Y. Lau. Space-Charge Effects on Multipactor on a Dielectric. *IEEE Transactions on Plasma Science*, 28(3):529-536, 2000.

- [37] R. Kishek and Y.Y. Lau. Interaction of Multipactor Discharge and rf Circuit. *Physical Review Letters*, 75(6):1218-1221, 1995.
- [38] R.A. Kishek and Y.Y. Lau. A novel phase focusing mechanism in multipactor discharge. *Physics of Plasmas*, 3(5):1481-1483, 1996.
- [39] R. A. Kishek, Y. Y. Lau, and D. Chernin. Steady state multipactor and dependence on material properties. *Physics of Plasmas*, 4(3):863-872, 1997.
- [40] R.A. Kishek. Interaction of Multipactor Discharge and RF structures. *PhD dissertation, University of Michigan*, 1997.
- [41] J.R.M. Vaughan. A New Formula for Secondary Emission Yield. *IEEE Transactions on Electron Devices*, 36(9):1963-1967, 1989.
- [42] A. Shih and C. Hor. Secondary Emission Properties as a Function of the Electron Incidence Angle. *IEEE Transactions on Electron Devices*, 40(4):824-829, 1993.
- [43] R. Seviour. The Role of Elastic and Inelastic Electron Reflection in Multipactor Discharges. *IEEE Transactions on Electron Devices*, 52(8):1927-1930, 2005.
- [44] V.E. Semenov, E.I. Rakova, D. Anderson, M. Lisak, and J. Puech. Importance of Reflection of Low-Energy Electrons on Multipactor Susceptibility Diagrams for Narrow Gaps. *IEEE Transactions on Plasma Science*, 37(9):1774-1781, 2009.
- [45] M. S. Feldman, A. A. Hubble, R. Spektor and P. T. Partridge. Effects of Backscattered Electrons on Multipactor Simulations with Parallel Magnetic Fields. In *Proceedings 2018 IEEE MTT-S International Conference on Numerical Electromagnetic and Multiphysics Modeling and Optimization (NEMO)*.
- [46] C. Vicente, M. Mattes, D. Wolk, H.L. Hartnagel, J.R. Mosig, and D. Raboso. Contribution to the RF Breakdown in Microwave Devices and its Prediction. In *Proceedings of the 2006 Power Modulator Symposium (IEEE, New York, 2006)*, ISSN 1930-885X, pp. 22–27.
- [47] Computer Simulation Technology (CST). URL: <https://www.cst.com>
- [48] C. Vicente. FEST3D-A simulation tool for multipactor prediction. In *Proceedings 5th Int. Multipactor Corona Passive Intermodulation in Space RF Hardware Workshop*, pp. 11-17, 2005.
- [49] C. Vicente. Multipactor and corona discharge: Theoretical fundamentals and analysis with CST and SPARK3D software tools. In *Proceedings 2017 IEEE International Symposium on Electromagnetic Compatibility & Signal/Power Integrity (EMCSI)*, pp. 1-48, 2017.

- [50] A. Friedman, R.H. Cohen, D.P. Grote, S.M. Lund, W.M. Sharp, J.L. Vay, I. Haber, and R.A. Kishek. Computational Methods in the Warp Code Framework for Kinetic Simulations of Particle Beams and Plasmas. *IEEE Transactions on Plasma Science*, 42(5):1321-1334, 2014.
- [51] M.A. Furman and M.T.F. Pivi. Probabilistic model for the simulation of secondary electron emission. *Physical Review Special Topics – Accelerators and Beams*, 5(12):124404, 2002.
- [52] V. Nistor, L.A. Gonzalez, L. Aguilera, I. Montero, L. Galdo, U. Wochner, and D. Raboso. Multipactor Suppression by Micro-structured Gold/Silver Coatings for Space Applications. *Applied Surface Science*, 315:445-453, 2014.
- [53] J. Vague, J.C. Melgarejo, M. Guglielmi, V.E. Boria, S. Anza, C. Vicente, M.R. Moreno, M. Taroncher, B. Martinez, and D. Raboso. Multipactor Effect Characterization of Dielectric Materials for Space Applications. *IEEE Transactions on Microwave Theory and Techniques*, 66(8):3644-3655, 2018.
- [54] V. E. Semenov, N.A. Zharova, N.I. Zaitsev, A.K. Gvozdev, A.A. Sorokin, M. Lisak, J. Rasch, and J. Puech. Reduction of the Multipactor Threshold Due to Electron Cyclotron Resonance. *IEEE Transactions on Plasma Science*, 40(11):3062-3069, 2012.
- [55] M. Mostajeran. Cross fields and two-sided multipactor. *Physics of Plasmas*, 25(103115), 2018.
- [56] S.G. Jeon, J. Kim, S.T. Han, S.S. Jung, and J.U. Kim. Theoretical study of dc-biased single-surface multipactors. *Physics of Plasmas*, 16(073101), 2009.
- [57] A. Kryazhev, M. Buyanova, V. Semenov, D. Anderson, M. Lisak, J. Puech, L. Lapiere, and J. Sombrin. Hybrid resonant modes of two-sided multipactor and transition to the polyphase regime. *Physics of Plasmas*, 9(11):4736-4743, 2002.
- [58] A.L. Gilardini. New breakdown modes of the multipacting discharge. *Journal of Applied Physics*, 71(9):4629-4631, 1992.
- [59] S. Riyopoulos. Higher-order, asymmetric order multipactors. *Physics of Plasmas*, 14(112101), 2007.
- [60] R.A. Kishek. Ping-pong modes and higher-periodicity multipactor. *Physics of Plasmas*, 20(056702), 2013.
- [61] R.A. Kishek. Ping-Pong Modes: A New Form of Multipactor. *Physical Review Letters*, 108(035003), 2012.

- [62] M. Siddiqi and R.A. Kishek. Simulation of Ping-pong Multipactor with Continuous Electron Seeding. In *Proceedings of the 2016 North American Particle Accelerator Conference*, 181, 2016.
- [63] V. Shemelin. On boundaries of ping-pong modes in multipacting. *Physics of Plasmas*, 25(053105), 2018.
- [64] I.A. Kossyi, G.S. Lukyanchikov, V.E. Semenov, E.I. Rakova, D. Anderson, M. Lisak, and J. Puech. Polyphase (non-resonant) multipactor in rectangular waveguides. *Journal of Physics D: Applied Physics*, 41(065203), 2008.
- [65] R. Udiljak, D. Anderson, M. Lisak, V.E. Semenov, and J. Puech. Multipactor in a coaxial transmission line. I. Analytical Study. *Physics of Plasmas*, 14(033508), 2007.
- [66] A.M. Perez, C. Tienda, C. Vicente, S. Anza, J. Gil, B. Gimeno, V.E. Boria, and D. Raboso. Prediction of Multipactor Breakdown Thresholds in Coaxial Transmission Lines for Travelling, Standing, and Mixed Waves. *IEEE Transactions on Plasma Science*, 37(10):2031-2040, 2009.
- [67] E. Sorolla, A. Sounas, and M. Mattes. Space charge effects for multipactor in coaxial lines. *Physics of Plasmas*, 22(033502), 2015.
- [68] V.E. Semenov, N. Zharova, R. Udiljak, D. Anderson, M. Lisak, and J. Puech. Multipactor in a coaxial transmission line. II. Particle-in-cell simulations. *Physics of Plasmas*, 14(033509), 2007.
- [69] D. Gonzalez-Iglesias, M. Rodriguez, O.M. Belda, B. Gimeno, V.E. Boria, D. Raboso, and V.E. Semenov. Analysis of Multipactor Effect Using a Phase-Shift Keying Single-Carrier Digital Modulated Signal. *IEEE Transactions on Electron Devices*, 60(8):2664-2670, 2013.
- [70] D. Gonzalez-Iglesias, A.M. Perez, S. Anza, J. Vague, B. Gimeno, V.E. Boria, D. Raboso, C. Vicente, J. Gil, F. Caspers, and L. Conde. Multipactor in a Coaxial Line Under the Presence of an Axial DC Magnetic Field. *IEEE Electron Device Letters*, 33(5):727-729, 2012.
- [71] D. Gonzalez-Iglesias, A.M. Perez, S. Anza, J. Vague, B. Gimeno, V.E. Boria, D. Raboso, C. Vicente, J. Gil, F. Caspers, and L. Conde. Multipactor Mitigation in Coaxial Lines by Means of Permanent Magnets. *IEEE Transactions on Electron Devices*, 61(12):4224-4231, 2014.
- [72] D. Gonzalez-Iglesias, O. Monerris, B. Gimeno, M.E. Diaz, V.E. Boria, and P.M. Iglesias. Multipactor RF Breakdown in Coaxial Transmission Lines With Digitally Modulated Signals. *IEEE Transactions on Electron Devices*, 63(10):4096-4103, 2016.

- [73] R.A. Kishek, Y.Y. Lau, L.K. Ang, A. Valfells, and R. M. Gilgenbach. Multipactor discharge on metals and dielectrics: Historical review and recent theories. *Physics of Plasmas*, 5(5):2120-2126, 1998.
- [74] P.T. Farnsworth. Television by electron image scanning. *Journal of the Franklin Institute*, 218(4):411-444, 1934.
- [75] E. W. B. Gill and A.V. Engel. *Proc. R. Soc. London, Ser. A* 192, 446 1948.
- [76] A.L. Gilardini. Multipacting discharges: Constant-k theory and simulation results. *Journal of Applied Physics*, 78(2):783-795, 1995.
- [77] S. Riyopoulos, D. Chernin, and D. Dialetis. Theory of electron multipactor in crossed fields. *Physics of Plasmas*, 2(8):3194-3213, 1995.
- [78] S. Riyopoulos, D. Chernin, and D. Dialetis. Effect of Random Secondary Delay Times and Emission Velocities in Electron Multipactors. *IEEE Transactions on Electron Devices*, 44(3):489-497, 1997.
- [79] S. Riyopoulos. Multipactor with electric field retarding secondary emission. *Physics of Plasmas*, 5(1):305-311, 1998.
- [80] V. Shemelin. Generalized phase stability in multipacting. *Physical Review Special Topics – Accelerators and Beams*, 14(9):092002, 2011.
- [81] A. Dexter and R. Seviour. Rapid generation of multipactor charts by numerical solution of the phase equation. *Journal of Physics D: Applied Physics*, 38:1383-1389, 2005.
- [82] A. Valfells, R.A. Kishek, and Y.Y. Lau. Frequency response of multipactor discharge. *Physics of Plasmas*, 5(300), 1998.
- [83] V. Semenov, A. Kryazhev, D. Anderson, and M. Lisak. Multipactor suppression in amplitude modulated radio frequency fields. *Physics of Plasmas*, 8(11):5034-5039, 2001.
- [84] S. Anza, C. Vicente, B. Gimeno, V.E. Boria, and J. Armendariz. Long-term multipactor discharge in multicarrier systems. *Physics of Plasmas*, 14(082112), 2007.
- [85] S. Anza, M. Mattes, C. Vicente, J. Gil, D. Raboso, V. E. Boria, and B. Gimeno. Multipactor theory for multicarrier signals. *Physics of Plasmas*, 18(032105), 2011.

- [86] S.A. Rice and J.P. Verboncoeur. Migration of Multipactor Trajectories via Higher-Order Mode Perturbation. *IEEE Transactions on Plasma Science*, 45(7):1739-1745, 2017.
- [87] A. Iqbal, J. Verboncoeur, and P. Zhang. Temporal multiparticle Monte Carlo simulation of dual frequency single surface multipactor. *Physics of Plasmas*, 26(024503), 2019.
- [88] A.A. Hubble, M.S. Feldman, P.T. Partridge, and R. Spektor. Evolution of multipactor breakdown in multicarrier systems. *Physics of Plasmas*, 26(053502), 2019.
- [89] J.S. Chang, P.A. Lawless, and T. Yamamoto. Corona Discharge Processes. *IEEE Transactions on Plasma Science*, 19(6):1152-1166, 1991.
- [90] M. Siddiqi and R.A. Kishek. A predictive model for two-surface multipactor stability and growth based on chaos theory. *Physics of Plasmas*, 26(043104), 2019.
- [91] M. Siddiqi and R.A. Kishek. Map-Based Multipactor Theory for Cross-Field Devices. *IEEE Transactions on Electron Devices*, 66(7):3162-3167, 2019.
- [92] M. Siddiqi and R.A. Kishek. Construction of Multipactor Susceptibility Diagrams from Map-Based Theory. *IEEE Transactions on Electron Devices*, 66(8):3587-3591, 2019.
- [93] M. Siddiqi and R.A. Kishek. A Predictive Model for Multipactor Discharge in Coaxial Systems Based on Chaos Theory. *IEEE Transactions on Electron Devices*, to be published.
- [94] M. Siddiqi and R.A. Kishek. A Predictive Model for Multipactor Discharge in Multicarrier Systems Based on Chaos Theory. *IEEE Transactions on Microwave Theory and Techniques*, to be published.
- [95] Edward Ott. Chaos in dynamical systems. Cambridge university press, 2002.
- [96] R.A. Kishek. Coexistence of mixed mode multipactor. *Physics of Plasmas*, 19(124501), 2012.
- [97] Y.Y. Lau. Fluid description of kinetic modes. *Physics of Plasmas*, 1(2816), 1994.
- [98] L. Petzold. Automatic selection of methods for solving stiff and nonstiff systems of ordinary differential equations. *SIAM Journal on Scientific and Statistical Computing*, 4(1):136-148, 1983.